# Radial Mass Transfer Enhancement in Bubble-Train Flow

Von der Fakultät für Maschinenwesen der
Rheinisch-Westfälischen Technischen Hochschule Aachen
zur Erlangung des akademischen Grades eines
Doktors der Ingenieurwissenschaften
genehmigte Dissertation

vorgelegt von

Dipl.-Ing. Rainer Gruber

aus London, Großbritannien

Berichter: Universitätsprofessor Dr.-Ing. Thomas Melin
Universitätsprofessor Dr.-Ing. Wolfgang Marquardt

Tag der mündlichen Prüfung: 13. 12. 2001

Die vorliegende Arbeit entstand während meiner Tätigkeit am Institut für Verfahrenstechnik der Rheinisch-Westfälischen Technischen Hochschule Aachen.

Allen, die zum Gelingen dieser Arbeit beigetragen haben, danke ich recht herzlich. Mein besonderer Dank gilt dabei:

Herrn Prof. Dr.-Ing. T. Melin für seine fachliche Betreuung, die gewährte Freiheit bei der Bearbeitung des Projektes sowie für seine ansteckende Begeisterung für die Verfahrenstechnik,

Herrn Prof. Dr.-Ing. W. Marquardt für die Übernahme des Koreferates,

meinen studentischen Mitarbeitern Julia Beyer, Carsten Stevering, Jens Hoppe, Jörn Buhn, Johannes Meier, Oliver Willmann, Christine Feldmann, Daniel Medart, Jan Baumert und Felix Hühnerschulte für ihre wissenschaftliche Neugierde und ihren unermüdlichen Einsatz,

den Mitarbeitern des Instituts aus Labor, Werkstatt und Sekretariat, die durch ihr Engagement stets eine große Hilfe waren,

und meiner Frau Kathrin für ihre unentbehrliche Unterstützung und Geduld.

Für Kathrin.

# Contents

# List of Figures

# Symbols

## Roman

| | | |
|---|---|---|
| $A_w$ | $m^2$ | surface area of the inner wall of the capillary |
| Bo | $-$ | Bond-number, Bo $= \Delta\rho g d_i^2/\sigma$ |
| $C$ | $kmol\ m^{-3}$ | molar concentration |
| Ca | $-$ | capillary-number, Ca $= \eta u_B \sigma^{-1}$ |
| $D$ | $m^2 s^{-1}$ | Fickian diffusion coefficient |
| $d_i$ | $m$ | tube diameter |
| E | $-$ | enhancement factor, $\mathrm{Sh}_{bubble-train}\mathrm{Sh}^{-1}_{singlephase}$ |
| $E_{(\beta)}$ | $-$ | distribution density function of bubble lengths |
| $dL$ | $m$ | characteristic length of a cell on the numeric grid |
| g | $ms^{-2}$ | gravitational acceleration, $g = 9.81 ms^{-2}$ |
| Gz | $-$ | Graetz-number, $d_i^2 \overline{u} D^{-1} l^{-1}$ |
| $h$ | $m$ | thickness of liquid film between bubble and wall |
| $k_L$ | $ms^{-1}$ | mass transfer coefficient between liquid and wall |
| $l$ | $m$ | tube length |
| $\dot{n}''$ | $kmol\ m^{-2} s^{-1}$ | molar flux |
| Pe | $-$ | Peclet-number, Pe $= u d_i D^{-1}$ |
| $r$ | $m$ | radial coordinate, $0 \leq r \leq R$ |
| $R$ | $m$ | tube radius |
| $r_0$ | $m$ | radial position of zero relative axial velocity |
| $r_1$ | $m$ | radial position of stagnation streamline |
| Re | $-$ | Reynolds-number, Re $= d_i u \nu^{-1}$ |
| Sc | $-$ | Schmidt-number, Sc $= \nu D^{-1}$ |
| Sh | $-$ | Sherwood-number, Sh $= k_L d_i D^{-1}$ |
| $u$ | $ms^{-1}$ | axial liquid velocity |
| $\overline{u}$ | $ms^{-1}$ | volume-average liquid velocity |
| $u_B$ | $m/s$ | axial bubble velocity |

| | | |
|---|---|---|
| $\dot{V}$ | $m^3 s^{-1}$ | volume flow rate |
| $v$ | $ms^{-1}$ | characteristic fluid velocity in a numerical cell |
| $z$ | $m$ | axial coordinate |

## Greek

| | | |
|---|---|---|
| $\beta$ | $-$ | dimensionless distance between bubbles, $\beta = l_{plug} d_i^{-1}$ |
| $\gamma$ | $-$ | dimensionless axial coordinate, $\gamma = z/d_i$ |
| $\gamma_{ce}$ | $-$ | dimensionless concentration entry length |
| $\gamma_{he}$ | $-$ | dimensionless hydrodynamic entry length |
| $\delta$ | $-$ | dimensionless thickness of film between bubble and wall, $h d_i^{-1}$ |
| $\epsilon$ | $-$ | void fraction, $\epsilon = \dot{V}_{gas}/\dot{V}_{tot}$ |
| $\zeta$ | $-$ | dimensionless bubble length, $\zeta = l_{bubble} di^{-1}$ |
| $\eta$ | $Pa\,s$ | dynamic viscosity |
| $\nu$ | $m^2 s^{-1}$ | kinematic viscosity |
| $\rho$ | $kgm^{-3}$ | density |
| $\sigma$ | $Nm^{-1}$ | surface tension |
| $\psi$ | $-$ | ratio of bubble and liquid velocities, $\psi = u_B \overline{u}^{-1}$ |

## General subscripts

| | |
|---|---|
| *am* | arithmetic mean value |
| *bubble* | in/of a gas bubble |
| *gas* | in/of the gas phase |
| *liq* | in/of the liquid phase |
| *lm* | logarithmic mean value |
| *plug* | in/of a liquid plug |
| *tot* | value for the overall (total) flow, i. e. for both gas and liquid |
| *w* | wall |
| *z* | local value at axial position |
| $\alpha$ | value at entrance to the capillary |
| $\omega$ | value at exit from capillary |

# Introduction

This work is a study of mass transfer in a two-phase flow regime, known as bubble-train flow. This regime occurs when large gas bubbles are introduced into a liquid flowing laminarly through a duct with a small cross section. Under these circumstances, the bubbles or droplets adopt a characteristic capsular shape. They almost completely fill the cross section of the duct, remaining separated from the wall by a thin film of liquid.

Compared with single-phase laminar flow, bubble-train flow has two characteristics that are potentially useful: the axial segregation of the bulk liquid significantly reduces axial dispersion, while at the same time inducing a circulating flow pattern in the liquid, which enhances radial transport.

In the past, these effects have rarely been exploited. The primary technical application has been in automated continuous-flow analysers, where bubble-train flow is used to separate samples from each other [1]. The effect of radial transport enhancement is a common observation in capillary blood vessels [2], but has not yet found its way into technical application beyond laboratory experiments. Given the recent interest in micro-process technology, this may change fundamentally in the near future: laminar liquid flow through micro-channels is characteristic of micro-processes and many micro-unit operations may profit from bubble-train flow.

The systematic exploitation of radial transport enhancement by bubble-train flow requires a reliable correlation of the parameters involved to quantify its effect. Despite the considerable attention given to two-phase pipe flows, the available literature does not satisfy this demand. There are several reasons for this shortcoming. First of all, many authors studied two-phase flow in pipes with a diameter larger than the capillary limit [3, 4, 5, 6]. It has only recently been established that the bubble-flow regimes observed at such diameters differ from bubble-train flow [7], and thus the results from these studies are not readily applicable to the latter case.

Secondly, the majority of available studies are devoted to heat transfer, which differs in two respects from mass transfer: heat conductance in liquids is far faster than solute

diffusion and thus heat transfer studies work in a range of Prandtl-numbers smaller by several orders of magnitude than the corresponding Schmidt-numbers in mass transfer. The results from heat transfer studies can thus only be applied to mass transfer by a speculative extrapolation. Furthermore, heat can be transported between wall and liquid via the gas bubbles, while a solute generally cannot, resulting in an over-prediction of mass transfer by heat transfer correlations [8].

Thirdly, even allowing for the shortcomings discussed above, none of the previous studies have been broad enough to form the basis for a generalised correlation. This is hardly surprising, given the large number of free parameters involved, which results in an insurmountable task if the necessary data are to be collected by experiment.

It is therefore no coincidence that the only attempt at devising a general model took a purely theoretical approach: Duda and Vrentas [9, 10] studied the flow pattern and heat transfer in bubble-train flow by solving the boundary value problem analytically. In spite of their formidable mathematical endeavour, the results are unsatisfactory in two respects: in order to render the problem solvable, they had to simplify the geometry by assuming cylindrical rather than capsular bubbles and omitting the liquid film between bubble and wall. Furthermore, their results are presented as a system of implicit infinite series, requiring extensive numerical effort in their evaluation.

Besides the theoretical work of Duda and Vrentas, there is, to my knowledge, only a single experimental study to date that directly addresses radial mass transfer in bubble-train flow. It was conducted by Horvath et al. [8], who used a tubular reactor to measure mass transfer. Although limited in scope, the study supplies some valuable reference data and allows the general conclusion that the rate of radial mass transfer in bubble-train flow lies between the values for single-phase laminar and turbulent flow.

In summary, only very little data and no general correlation of radial mass transfer in bubble-train flow are available. The objective of the present work is to fill this gap with a comprehensive study of the problem and to develop a corresponding correlation. The constraints placed by limited experimental resources on the scope of previous studies will be overcome by making extensive use of a numerical simulation of the problem. Nevertheless, the study will be restricted to capillaries with a circular cross section, to Newtonian liquids and to a dilute solute, since a departure from these three constraints would require a fundamentally different approach. And finally, a constant concentration boundary condition alone will be considered, since the constant flux condition common in heat transfer problems is very rarely encountered in mass transfer.

# 1

# Theoretical considerations

## 1.1 Single-phase pipe flow

Before turning our attention to bubble-train flow, it is useful to recall some of the features of single-phase pipe flow, since many of the features of bubble-train flow can be appreciated more readily by comparison with their single-phase counterparts. As in the subsequent study of bubble-train flow, we will limit the discussion to pipes with a circular cross section.

A fluid with constant properties flowing through a smooth pipe can adopt one of two different flow patterns: laminar flow, which is observed at low to intermediate flow rates, is characterised by the absence of radial velocity components and by Poiseuille's parabolic axial velocity profile which is independent of all fluid properties:

$$\frac{u(r)}{\overline{u}} = \frac{1}{2}\left(1 - \left(\frac{r}{R}\right)^2\right) \tag{1.1}$$

At higher flow rates, the centre core of the laminar flow brakes down into turbulent flow, which is characterised by the formation of eddies. As the flow rate is further increased, the eddy size decreases until at the limit of fully established turbulence the flow becomes isotropic. Owing to the sheer stress exerted by the wall on the flowing liquid, turbulence ceases near the wall, resulting in a laminar boundary layer.

The pattern of pipe flow is governed by the following quantities:

| Quantity | Dimension | Description |
|---|---|---|
| $d_i$ | [l] | inner tube diameter |
| $l$ | [l] | length of the tube |
| $\overline{u}$ | $[l \cdot t^{-1}]$ | volume-average liquid velocity |
| $\nu$ | $[m^2 \cdot t^{-1}]$ | kinematic viscosity of the liquid |

Following Buckingham's $\pi$-theorem, these four quantities based on two dimensions can be reduced to $4 - 2 = 2$ dimensionless groups. The customary choice are the Reynolds-number

$$\mathrm{Re} = \frac{\overline{u} d_i}{\nu} \tag{1.2}$$

and a dimensionless length

$$\gamma = \frac{l}{d_i} \tag{1.3}$$

Re governs both the transition between laminar and turbulent flow, which occurs at approximately Re=2300, and the entry length of the laminar flow. After entering the tube, the final flow pattern is gradually established over a length of tube called the hydrodynamic entry length[1]. In laminar flow, the entry length is [11, p. 351]

$$\gamma_{he} \approx 0.056 \cdot \mathrm{Re} \tag{1.4}$$

while the estimate for turbulent flow is

$$\gamma_{he} \approx 10 \tag{1.5}$$

Mass transfer between the liquid and the wall introduces two further quantities to the problem: a measure for the concentration of solute and a measure for its diffusivity. The latter can be expressed, for example, by the Fickian diffusion coefficient, while it is customary to cast the former into a mass transfer coefficient:

[1]The hydrodynamic entry length is generally understood to be the length of tube at which the velocity at the centre of the tube has approached its final value to within 1%.

| Quantity | Dimension | Description |
|---|---|---|
| $D$ | $[m^2 \cdot s^{-1}]$ | diffusion coefficient |
| $k_L$ | $[m \cdot s^{-1}]$ | mass transfer coefficient |

$k_L$ is defined as the ratio of the resulting flux density to the gradient causing the flux. For single phase flow, there are three definitions of $k_L$ in use, which differ in their formulation of the driving concentration gradient [12, p. 391]. A local mass transfer coefficient can be defined in terms of the local concentration gradient between bulk and wall:

$$k_{L,z} = \frac{\dot{n}''}{C_w - C|_z} \tag{1.6}$$

Typically, mass transfer coefficients are used to describe a separation process as a whole. It is therefore more usual to formulate $k_L$ in terms of an input and output concentration and a mean driving force. Using the arithmetic mean of the driving forces at the entry and at the exit of the process leads to the following arithmetically averaged mass transfer coefficient:

$$k_{L,am} = \frac{\dot{n}''}{\frac{(C_{w,\alpha}-C_\alpha)+(C_{w,\omega}-C_\omega)}{2}} \tag{1.7}$$

where $\dot{n}'' = \frac{\dot{V}(C_\alpha - C_\omega)}{A_w}$ is the density of the overall flux to or from the wall.

Alternately, one can use the logarithmic average of the driving force:

$$k_{L,lm} = \frac{\dot{n}''}{\frac{(C_{w,\alpha}-C_\alpha)-(C_{w,\omega}-C_\omega)}{\ln\left(\frac{C_{w,\alpha}-C_\alpha}{C_{w,\omega}-C_\omega}\right)}} \tag{1.8}$$

This formulation follows naturally from the integration of the local mass balance along the length of the apparatus and I shall use it in the present study.

The two additional quantities introduce no additional dimension to the problem and thus they give rise to two further dimensionless groups. The Schmidt-number is defined by

$$\mathrm{Sc} = \frac{\nu}{D} \tag{1.9}$$

and is analogous to the Prandtl-number in heat transfer, while the Sherwood-number is defined by

$$\mathrm{Sh} = \frac{k_L d_i}{D} \tag{1.10}$$

and corresponds to the Nußelt-number in heat transfer. Depending on the underlying definition of $k_L$, Sh can be either a local, an arithmetic mean or a log-average number.

Mass transfer between the fluid and the wall results in a characteristic concentration profile over the tube diameter which is similar in shape to the velocity profile. After the flow enters the tube, the concentration profile is gradually established over a length of tube known as the concentration entry length[2]. For laminar flow, it can be approximated as [13, p. 165]

$$\gamma_{ce} = 0.05 \cdot \mathrm{Re} \cdot \mathrm{Sc} \tag{1.11}$$

while the estimate for turbulent flow is identical to equ. 1.5. Comparing equ. 1.4 and 1.11 while bearing in mind that Sc is in the order of $10^3$, shows that in laminar flow, the concentration entry length is very much longer than the hydrodynamic entry length. In fact, in most cases the concentration profile does not fully develop before the flow exits the tube.

Much attention has been devoted to correlating the rate of heat or mass transfer in pipe flow (for detailed reviews, see [11, 12, 13]). For laminar flow, the problem is comparatively well accessible to analytical solution if constant boundary conditions and fluid properties and a hydrodynamically fully developed flow are assumed and axial diffusion is neglected. Under these restrictions, the problem was first solved independently by Graetz [14] and Nußelt [15] and is known as the Graetz-Nußelt problem[3]. A significant finding of their studies is that the solution can be expressed in terms of a single dimensionless group, which results from combining the three independent groups. This new dimensionless group is known as the Graetz-number:

$$\mathrm{Gz} = \mathrm{Re} \cdot \mathrm{Sc} \cdot \gamma^{-1} = \frac{d_i^2 \overline{u}}{Dl} \tag{1.12}$$

Thus the solution to the Graetz-Nußelt problem can be expressed as

$$Sh = f(Gz) \tag{1.13}$$

[2]In analogy to the hydrodynamic entry length, the concentration entry length is defined as the length after which Sh is within 1% of its final value.

[3]Graetz and Nußelt actually studied the heat transfer problem. Under the assumption of sufficient dilution to neglect diffusion-induced convection, their results can be applied to mass transfer as well.

As is typical for the analytical solution of problems involving diffusion in cylindrical coordinates, however, the original solution is expressed as a set of infinite series. Several authors have undertaken to develop more facile mathematical expressions. The best known of these is Lévêque's solution [16], which is limited to rapid flow through short tubes and thus to high Graetz-numbers. Under these circumstances, the concentration profile is in the early stage of its development, the concentration boundary layer is limited to a thin film at the wall and the concentration profile in this film can be linearised. In terms of an arithmetically averaged Sherwood-number, Lévêque's solution is:

$$Sh_{am} = 1.615 \cdot \mathrm{Gz}^{1/3} \tag{1.14}$$

Several authors have taken a different approach to developing a more facile solution without reducing the range of validity by fitting empirical expressions to the infinite series solution. To my knowledge the most precise of these correlations was developed by Stephan [11, p. 363] and expresses the log-mean Sherwood-number as:

$$\mathrm{Sh}_{lm} = \frac{3.657}{\tanh\left(2.264\ \mathrm{Gz}^{-1/3} + 1.7\ \mathrm{Gz}^{-2/3}\right)} + 0.0499\ \mathrm{Gz}\ \tanh\left(\mathrm{Gz}^{-1}\right) \tag{1.15}$$

This solution is valid for the entire range of Gz and deviates from the series solution by no more than 1%.

The problem of mass transfer in turbulent pipe flow has not been solved analytically. Empirical solutions have been reviewed, for example, by Baehr and Stephan [11, p. 366], who propose the following correlation developed by Gnielinski [17]:

$$\mathrm{Sh}_{lm} = \frac{\zeta/8(\mathrm{Re} - 1000)Pr}{1 + 12.7\sqrt{\zeta/8}\,(Pr^{2/3} - 1)} \left(1 + \left(\frac{d}{L}\right)^{2/3}\right) \tag{1.16}$$

with

$$\zeta = \frac{1}{\left(0.79 \ln(\mathrm{Re}) - 1.64\right)^2} \tag{1.17}$$

valid in the range of $2300 \leq \mathrm{Re} \leq 5 \cdot 10^6$, $0.5 \leq \mathrm{Pr} \leq 2000$ and $L/d > 1$.

Figure 1.1: Bubble-train flow consisting of air bubbles in water flowing through a 1.2 mm glas capillary. The capillary is submersed in water to reduce refraction.

## 1.2 Distinguishing bubble-train flow from other two-phase flow regimes

There is some confusion concerning the nomenclature for gas-liquid flow patterns in general and bubble-train flow in particular. The term "bubble-train flow" is used by Thulasidas et al. [18, 19], while other authors refer to the same pattern as "slug-flow" [8, 20], "plug-flow" [21] or simply as intermittent flow [22]. All terms imply a flow pattern characterised by a sequence of capsule-shaped bubbles which almost completely fill the cross section of the duct and are separated from the wall by a thin liquid film (Fig. 1.1). I shall use the term bubble-train flow throughout this study, since it is the most descriptive and has not yet been used for other flow patterns.

Recently, Triplett et al. [7] drew attention to the ambiguity of the above-mentioned nomenclatures, which lies in lumping two distinctly different flow patterns into one. In small tubes, the flow pattern is axially symmetrical and thus independent of the direction of gravity, whereas in larger tubes, buoyancy effects influence the pattern. In horizontal tubes, this leads to stratification while in vertical tubes, the bubbles rise through the liquid, resulting in increased slip streams.

But what is a small tube in the sense used above? First of all, as a means of distinction, these small ducts will be referred to as capillaries and flow through them as capillary flow. A capillary is characterised by a predominance of surface tension over buoyancy forces. The ratio of these forces, known as the Bond-number $\mathrm{Bo} = \Delta\rho g d_i^2/\sigma$, has been used by several authors to define the upper diameter limit of capillarity. From a theoretical stability analysis, Brauner and Maron [23] derived $\mathrm{Bo} < 4\pi^2$, while Suo and Griffith experimentally determined the more restrictive limit of $\mathrm{Bo} < 0.22$. Evaluating these limits for a typical range of surface tension values, we find the following limiting diameters for capillarity:

| Surface tension $\sigma$: | 10 mN/m (light hydrocarbons) | 75 mN/m (pure water) |
|---|---|---|
| Brauner & Maron | $d < 20mm$ | $d < 55mm$ |
| Suo & Griffith | $d < 1.5mm$ | $d < 4mm$ |

Suo's and Griffith's limit appears to be more reliable, since it agrees well with experimental observations [22, 7], while the prediction of Brauner and Maron does not. Bearing in mind that ubiquitous surfactants reduce the surface tension in most real feeds in comparison with pure media, capillary flows can be expected in tubes with a typical inner diameter below $1.5 \ldots 3\,\mathrm{mm}$. The scope of this study will be limited exclusively to the examination of bubble-train flow in capillaries. This limitation is justifiable, since the majority of potential applications - including micro-reactors and hollow-fibre membrane contactors - typically lie within the capillary limit. Besides, the extension to larger tubes would involve the study of far more diverse flow phenomena and thus make the scope of this work unmanageable. As a consequence, the term bubble-train flow as used in this work will imply the capillary flow pattern.

Bubble-train flow is one of several flow patterns that two-phase flow in capillaries can display. Several authors have studied these flow regimes and their transitions and have reported their results in terms of flow maps, with the superficial gas and liquid velocities as coordinates [20, 21, 22, 24]. Their results were recently reviewed by Triplett et al. [7], who presented a unified flow map for air-in-water capillary flows supported by the data of several investigations (Fig. 1.2). The map shows that bubble-train flow occurs at the lower end of the gas and liquid velocity scales. Increasing the liquid flow rate eventually leads to disruption of the bubbles so that bubble-train flow breaks down into a flow of more finely dispersed, smaller bubbles (Fig. 1.3 A). On the other hand, an increase in gas velocity eventually leads to a random joining of bubbles and a transition to annular flow (Fig. 1.3 C-D). Both transitions occur at superficial velocities of approximately $1 m/s$.

Of these two, the upper liquid velocity limit is more essential to our purpose of enhancing liquid radial mass transfer. In the air-in-water flow, the limiting liquid velocity translates to $\mathrm{Re} = 1000$ as the upper limit of bubble-train flow. This estimate must, however, be viewed with caution, since it is based solely on experimental evidence for aqueous systems and thus does not model the dependence of pattern transition on viscosity and interfacial tension. Despite the considerable attention devoted to this question in recent studies, the understanding of flow regime transitions is at present still incomplete. Thus we cannot define the limits of bubble-train flow more precisely at this stage. This is not a severe shortcoming, though, since the technical application of bubble-train flow will typically occur at low void fractions and $\mathrm{Re} < 100$ and thus well within the stability limits.

Finally, it should not be overlooked that the flow regime also depends on the method of bubble formation. It stands to reason that bubble-train flow will only be formed if the bubbles have an initial diameter at least equal to that of the duct. Smaller bubbles would

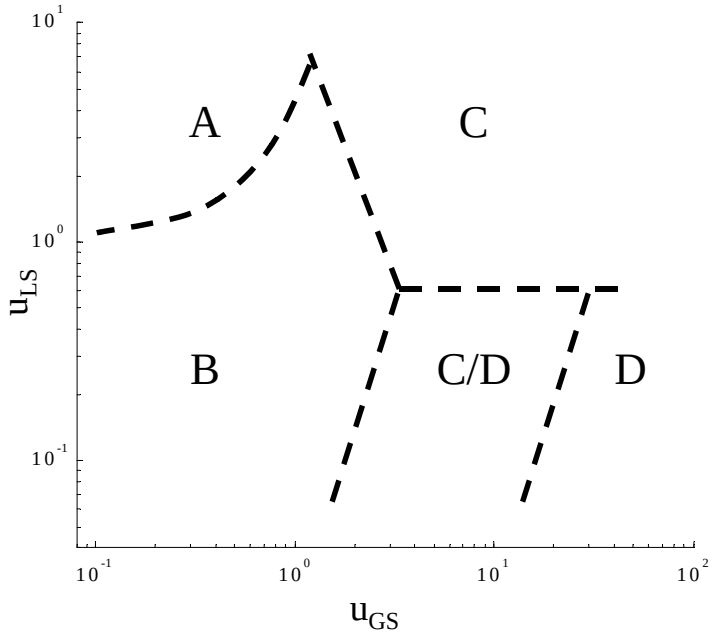


Figure 1.2: Flow map with transition lines between two-phase flow patterns, based on experiments with air-in-water flow through a 1.1 mm capillary [7]. $U_{GS}$ and $U_{LS}$ are the superficial gas and liquid velocities, respectively. Letters in the map refer to flow patterns illustrated in Fig. 1.3.

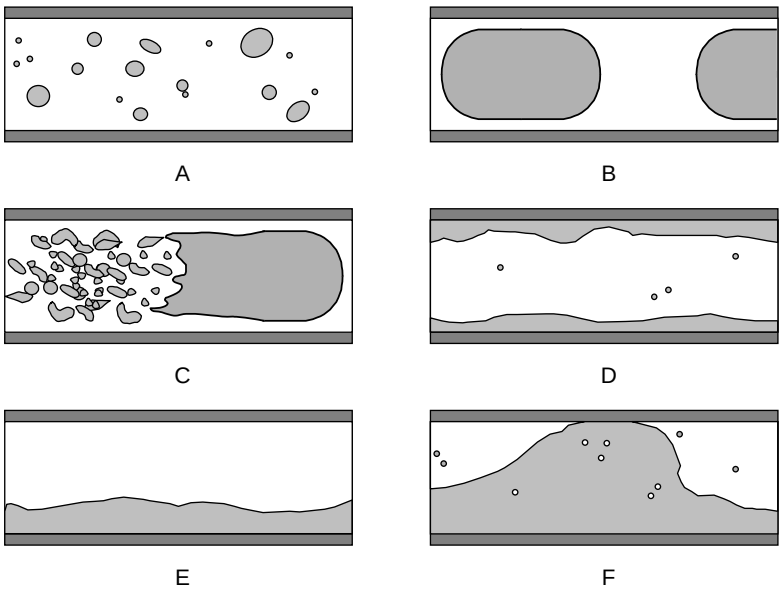


Figure 1.3: Schematic representation of flow patterns in capillary two-phase flow. A - Bubbly flow, B - Bubble-train flow , C - Churn flow, D - Annular Flow. Stratified flow patterns such as E and F are not observed in capillary flow.

have to coalesce first to form a bubble-train, so that at least over a partial length of the duct an intermediate flow pattern would arise.

## 1.3 The anatomy of bubble-train flow

After drawing the distinction between bubble-train flow and other two-phase flow regimes, we will now turn to studying the characteristics of bubble-train flow in more detail, beginning with a qualitative analysis and thereafter quantifying some of the findings.

The geometry of the bubbles in bubble-train flow result from a balance of viscosity, surface tension and pressure forces. Bretherton [25] studied the shape of the forward meniscus theoretically and concluded that for small to intermediate capillary-numbers, it can be approximated as a hemisphere. The same was confirmed by Giavedoni and Saita [26] for the trailing meniscus and thus, in summary, the shape of the bubbles appears to depart only slightly from that of a capsule with hemispherical caps and a cylindrical body. This approximation will be used throughout the study.

The bubbles remain separated from the wall of the capillary by a thin liquid film, which is essentially stagnant since the bubble exerts a very much smaller shear stress on the film than the wall does. As a consequence, the bubbles travel with a velocity $u_B$ slightly greater than the volume-average liquid velocity $\overline{u}$.

The bubbles act as plugs disrupting the parabolic laminar velocity profile of the bulk liquid (Fig. 1.4). Close to the tips of the bubbles, the axial bulk velocity has a plug-shape, whereas at a sufficient distance from the bubbles the parabolic laminar profile is assumed again[4]. The transition from parabolic to plug profile induces radial velocity components in the bulk liquid, which are the principle cause for the enhanced radial transport.

For a more detailed picture, we express the flow pattern in terms of a coordinate system moving with the velocity of the bubble or droplet (Fig. 1.5). In this frame of reference, we can identify two distinctive flow regions: a film-like region close to the wall of the duct which encloses an inner bulk region. The two regions are separated by the streamline connecting the stagnation points on the bubble surfaces which implies that there is no convective exchange of fluid between the two regions. Liquid in the outer film-region flows past the bubbles and is thus fed from the downstream plug while leaking into the upstream plug. By contrast, liquid in the inner bulk region adopts a recirculating flow pattern. Liquid from its outer rim is deflected by the upstream bubble and flows down the

[4]This assumes a sufficient length of the liquid plug.

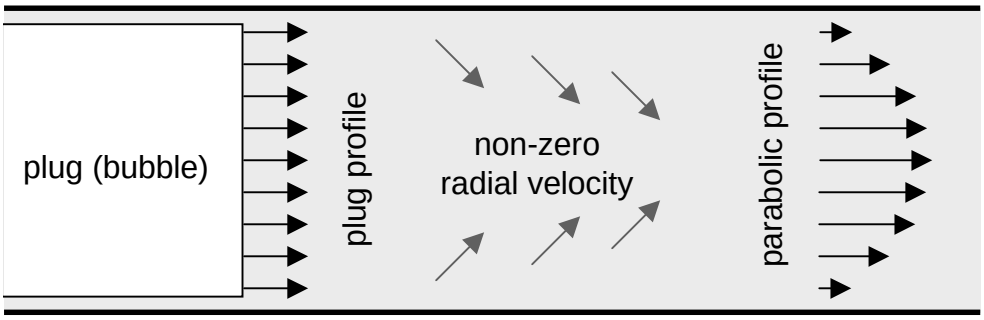


Figure 1.4: The bubble acts as a plug or piston, resulting in an approximately plug-shaped axial velocity profile in the liquid close to it. At an increasing distance from the bubble, the liquid gradually adopts the characteristic parabolic profile of laminar flow. The transition from plug to parabolic profile induces radial flow (gray arrows).

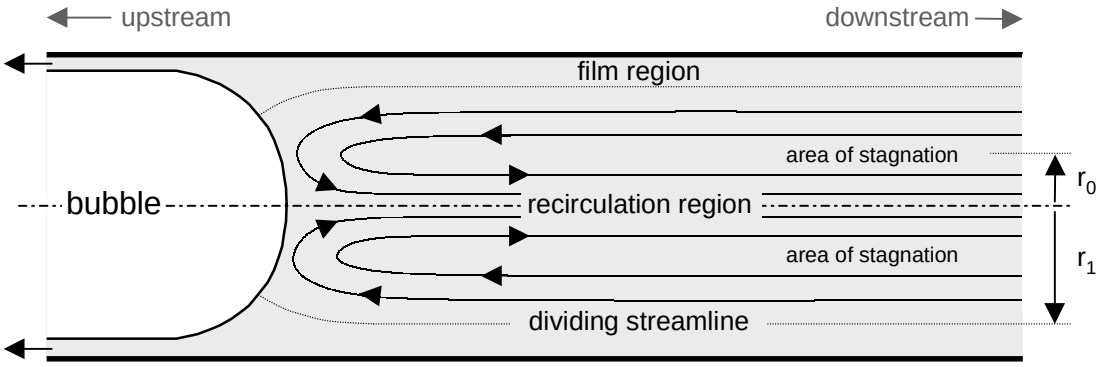


Figure 1.5: Bulk liquid flow occurs in two distinctive regions separated by the streamline linking the stagnation points on the bubbles (dotted line). In this figure, the coordinate system is fixed to the bubble.

centre of the duct, back towards the upstream bubble. Contained within this circulating flow is a torus-shaped area of stagnation.

Radial transport thus involves an essentially diffusive step across the film region and an essentially convective step in the recirculation region, characterised by a loop-shaped motion.

We now turn to describing bubble-flow geometry in quantitative terms. I shall first show that there is only one degree of freedom for the essential geometric measurements and they can thus be expressed in terms of a single parameter. Then I shall discuss the correlation of this parameter with the physical and hydrodynamic properties of the flow.

As already indicated, the liquid film separating the bubble from the wall leads to a velocity difference between bubble and bulk liquid. Assuming incompressibility of both

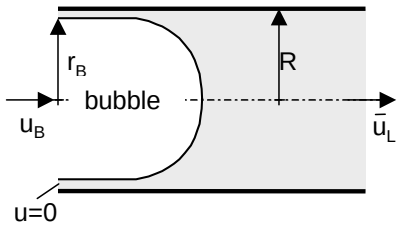


Figure 1.6: Balance volume for equ. 1.19.

gas and liquid and assuming also a stagnating film, the relationship of bubble velocity to film thickness can be established by studying a simple mass balance over the control volume shown in Fig. 1.6:

$$\pi R^2 \overline{u}_L = \pi r_B^2 u_B \tag{1.18}$$

$$\Leftrightarrow \frac{R^2}{r_B^2} = \frac{u_B}{\overline{u}_L} \equiv \psi \tag{1.19}$$

where the dimensionless bubble velocity $\psi$ will be used as the parameter to express the geometric measurements[5].

Solving equ. 1.19 for the film thickness $h = R - r_B$ we find

$$h = R\left(1 - \frac{1}{\sqrt{\psi}}\right) \tag{1.20}$$

or in approximation for thin films as suggested by Fairbrother and Stubbs [27]

$$h = \frac{R}{2}\left(1 - \frac{1}{\psi}\right) \tag{1.21}$$

In the coordinate system moving with the bubble, the fully established velocity profile of the bulk liquid can also be expressed in terms of $\psi$ as

$$u(r) = \frac{2u_B}{\psi}\left(1 - \frac{r^2}{R^2}\right) - u_B \tag{1.22}$$

The circulation of liquid in the plug is reflected by the relative velocity profile (equ. 1.22). The profile has a positive region corresponding to the forward flow close to the centre of the tube and a negative region of backward flow closer to the wall. In between lies a streamline with a zero relative velocity. Its position can be determined by setting equ. 1.22 to zero:

$$r_0 = \frac{R}{\sqrt{2}}\sqrt{2 - \psi} \tag{1.23}$$

[5]The nomenclature $\psi$ follows the suggestion of Thulasidas et al. [19]

Similarly, the position $r_1$ of the dividing streamline that connects the stagnation points and separates the film region from the recirculating region can be determined from equ. 1.22 as well. The rationale is that the forward and backward streams in the recirculating region must carry the same volumetric flow. Integrating flow over radius between the centre line and $r_1$ must therefore come to zero:

$$\int_0^{r_1} u(r) 2\pi r dr = 0 \tag{1.24}$$

$$\Leftrightarrow r_1 = R\sqrt{2-\psi} \tag{1.25}$$

Equ. 1.25 shows a limit of bubble-train flow at $\psi = 2$, which is equivalent to the bubbles travelling with twice the average bulk liquid velocity, $r_1$ becomes zero and the dividing streamline coincides with the centre of the capillary. In this case, the entire flow bypasses the bubble and there is no longer any recirculation between bubbles. While this limit, which was first predicted by Taylor [28], has been observed by Thulasidas et al. [19], it only occurs in tubes above the critical capillary diameter and is thus not considered in the present work.

We have now expressed the key geometric measurements of bubble-train flow in terms of a single dimensionless parameter $\psi$. It remains to be considered how $\psi$ is correlated to the fluid properties and hydrodynamic conditions.

Several authors have studied bubble velocities or film thicknesses in bubble-train flow. Fairbrother and Stubbs [27] studied the velocity ratio of bubbles and liquid and formulated the simple empirical correlation

$$\psi = \frac{1}{1-\sqrt{\mathrm{Ca}}} \tag{1.26}$$

for the range $7.5 \cdot 10^{-5} < \mathrm{Ca} < 0.014$, where Ca is the capillary-number defined as

$$\mathrm{Ca} = \frac{\eta u_B}{\sigma} \tag{1.27}$$

Marchessault and Mason [29] measured the film thickness by means of a travelling camera and proposed the correlation

$$\psi = \left( \frac{1}{1 - 0.05\,(\eta/\sigma)^{1/2} + 0.89\sqrt{\mathrm{Ca}}} \right) \tag{1.28}$$

where $\eta/\sigma$ are in $s/cm$ and the confidence range is $7 \cdot 10^{-6} < \mathrm{Ca} < 2 \cdot 10^{-4}$.

Bretherton [25] applied lubrication theory to the problem and theoretically derived

$$\psi = \frac{1}{1 - 1.29\,(3\mathrm{Ca})^{2/3}} \tag{1.29}$$

He estimated the validity to be within 10% up to Ca $< 0.005$. Bretherton's own attempt at experimental verification, however, showed a systematic deviation between theory and experiment.

The three correlations are in reasonable agreement with each other within their common regions of definition. They can thus be used to estimate the range of film thickness to be expected in bubble-train flow. Examining both typical (Re=100) and limiting operating conditions (Re=1000), we find the following film thicknesses based on equ. 1.26 for some typical fluids:

| | $\sigma$ $[N/m]$ | $\eta$ $[kg/m/s]$ | $\rho$ $[kg/m^3]$ | Re [–] | Ca | $\psi$ [–] | **h/d** [–] |
|---|---|---|---|---|---|---|---|
| water | $7.3 \cdot 10^{-2}$ | $1.0 \cdot 10^{-3}$ | $1.0 \cdot 10^{3}$ | 100 | $1.37 \cdot 10^{-3}$ | 1.038 | **0.9 %** |
| | | | | 1000 | $1.37 \cdot 10^{-2}$ | 1.133 | **3.0 %** |
| light hydrocarbon | $3.0 \cdot 10^{-2}$ | $4.0 \cdot 10^{-3}$ | $0.6 \cdot 10^{3}$ | 100 | $1.13 \cdot 10^{-3}$ | 1.035 | **0.8 %** |
| | | | | 1000 | $1.13 \cdot 10^{-2}$ | 1.118 | **2.7 %** |

The results show that under typical conditions the film thickness stays within 1% of the capillary diameter. Furthermore, it appears that the validity limit of equ. 1.26 coincides with the practical limit of Ca in bubble-train flow. At this limit, a typical film thickness of approximately 3% is predicted. For the present study, I shall assume this to be the maximum occurring film thickness.

In modelling radial transport in bubble-train flow, the question arises of how to represent the film thickness. The options are either to use Ca as an indirect expression of the film thickness or to use the dimensionless film thickness itself as the parameter. In a purely experimental study, the first option would make better sense, since it avoids the necessity of measuring the film thicknesses. In the present study, however, I shall use a numerical analysis as the principle source of data (see Section 2). Since the numerical simulation requires an explicit choice of film thickness, the second option will be used for this investigation. As a consequence, the results will be reported in terms of - among other parameters - the dimensionless film thickness instead of Ca.

This has the further advantage of not basing the results of this investigation on a possibly flawed or limited correlation for the film thickness. As was noted before, Bretherton's own attempt at experimental verification showed systematic deviation between theory and experiment, which he was not able to explain [25]. In view of the reasonable agreement

between the three correlations, one must conclude that they do not take account of all physical effects that can influence the geometry of the flow pattern. Furthermore, all three correlations are limited to a train of gas bubbles as opposed to a train of immiscible liquid drops. Although the latter case is not at the main focus of the present study, it does not seem wise to limit its scope without need.

As a final remark, the hydrodynamic entry length of bubble-train flow[6] can be estimated as roughly equal to that of single phase pipe flow (equ. 1.4), since the entry process involves exactly the same transition from plug to parabolic velocity profile - albeit that the transition is limited to the laminar region between the bubbles. Typical entry lengths are thus in the order of several capillary diameters and thus short enough to be neglected. I shall therefore treat bubble-train flow as hydrodynamically fully developed.

## 1.4 Dimensional analysis

It is useful and indeed customary to express the quantitative analysis of a problem in terms of dimensionless groups which reduces the number of independent variables and enhances the generality of the findings. Single-phase flow and mass transfer problems have already been dimensionally analysed in Section 1.1. To extend the set of dimensionless groups from single-phase to bubble-train flow, I shall introduce three new geometric parameters: the bubble length, the thickness of the liquid film between bubble and wall and the length of the liquid plug. The complete list of independent variables is thus summarised in Table 1.1.

The additional dimensionless groups required to describe bubble-train flow are dimensionless lengths and are therefore straightforward. Using the nomenclature suggested by Horvath et al. [8] as far as applicable, the complete set of dimensionless groups describing radial transport in bubble-train flow is as follows:

$$\mathrm{Re} = \frac{d_i \overline{u}}{\nu} \tag{1.30}$$

$$\mathrm{Sc} = \frac{\nu}{D} \tag{1.31}$$

$$\gamma = \frac{l_{tube}}{d_i} \tag{1.32}$$

$$\mathrm{Sh} = \frac{k_L d_i}{D} \tag{1.33}$$

[6]It is important to stress that hydrodynamic development merely implies reaching a steady velocity distribution throughout the liquid plug. It does not necessarily imply the full development of a parabolic velocity profile between the bubbles, since this will not occur in short liquid plugs.

| | Single Phase | Bubble-train flow |
|---|---|---|
| materials | $\rho\ [ml^{-3}]$ | |
| | $\nu\ [l^2t^{-1}]$ | |
| | $D\ [l^2t^{-1}]$ | |
| geometry | $d_i\ [l]$ | $l_{plug}\ [l]$ |
| | $l_{tube}\ [l]$ | $l_{bubble}\ [l]$ |
| | | $d_{film}\ [l]$ |
| kinetics | $\overline{u}\ [lt^{-1}]$ | |
| | $k_L\ [lt^{-1}]$ | |

Table 1.1: The parameters governing mass transfer in bubble-train flow.

$$\beta = \frac{l_{plug}}{d_i} \tag{1.34}$$

$$\zeta = \frac{l_{bubble}}{d_i} \tag{1.35}$$

$$\delta = \frac{d_{film}}{d_i} \tag{1.36}$$

The choice of variables deserves comment in several respects. The exclusion of surface tension and liquid density follows the arguments presented in the previous section and implies that the thickness of the film between bubble and wall will be used as an explicit parameter rather than correlating it via the surface tension. Additionally, this exclusion implies a rigid bubble geometry independent of surface tension and flow conditions.

Similarly, the exclusion of gravity as an independent variable implies the limitation of the present study to capillary flow.

The literature on two-phase pipe flow often uses the void fraction $\epsilon = \dot{V}_{gas}/\dot{V}_{tot}$ to describe flow patterns. This is not an additional parameter but rather a grouping of three of the parameters enumerated above as can be shown by elementary geometry:

$$\epsilon = \frac{7}{24}\frac{1-2\delta}{\beta+\zeta} \tag{1.37}$$

Furthermore, the definition of $k_L$ discussed in Section 1.1 requires amendment for two-phase flow, because the introduction of a second phase which is opaque to mass transfer[7] introduces an ambiguity into the definition of $\dot{n}''$. It can either be defined as before as the flux per overall wall area

$$\dot{n}'' = \frac{\dot{V}_{liq}\,(C_\alpha - C_\omega)}{A_w} \tag{1.38}$$

or as the flux per surface area contacted by the plugs[8]

$$\dot{n}'' = \frac{\dot{V}_{liq}\,(C_\alpha - C_\omega)}{(1-\epsilon)A_w} = \frac{\dot{V}_{tot}\,(C_\alpha - C_\omega)}{A_w} \tag{1.39}$$

where $\epsilon = \dot{V}_{gas}/\dot{V}_{tot}$ is the void fraction of the flow.

Both definitions have their merit. By using equ. 1.39, we obtain a Sherwood-number $\mathrm{Sh}_{plug}$ that describes the rate of mass transfer from an individual plug. As Horvath et al. [8] point out, $\mathrm{Sh}_{plug}$ thus conveys information about the relative magnitude of convective and diffusive transport in the liquid. On the other hand, using equ. 1.38 results in a Sherwood-number $\mathrm{Sh}_{process}$ that represents the average flux from the whole capillary wall. $\mathrm{Sh}_{process}$ is a measure for the enhancement[9] of the mass transfer process by using bubble-train flow.

The significant difference between both definitions can be illustrated by considering mass transfer from bubble-train flow with a constant flow rate and bubble length but gradually reduced plug lengths. Mixing in the liquid phase increases continuously as the plug length is reduced, resulting in an equally continuous rise of $\mathrm{Sh}_{plug}$. By contrast, we may expect $\mathrm{Sh}_{process}$ to reach a maximum at a certain plug length and then drop again as the plugs are further shortened. This decrease is caused by the trade-off between intensified mixing in the plug on the one hand and the reduction of wall area actually involved in mass transfer on the other. In conclusion, $\mathrm{Sh}_{plug}$ will offer more insight into the transport mechanism inside the plug whereas $\mathrm{Sh}_{process}$ is more relevant to the engineering objective of process enhancement.

Since in this study bubble-train flow is viewed as a means to enhance a mass transfer process, it would seem obvious to study the results in terms of $\mathrm{Sh}_{process}$. I shall not do so, however, for the following reason: It will be shown that the bubble length does not affect

[7] Opacity implies that the bubbles neither absorb nor transmit the solute and will be assumed throughout this study.

[8] The rationale being that mass transfer from the film is negligible and thus only the surface between the liquid plugs and the wall actively participates in mass transfer.

[9] Enhancement implies either treating more liquid to the same specification or treating the same flow to a higher specification.

the intensity of mass transfer from an individual plug. By analysing the results in terms of $\mathrm{Sh}_{plug}$ we can therefore neglect $\zeta$ which reduces the parameter domain by one dimension. The analysis can later be extended to $\mathrm{Sh}_{process}$ by simple multiplication:

$$\mathrm{Sh}_{process} = \mathrm{Sh}_{plug} \cdot (1 - \epsilon) \tag{1.40}$$

To summarise, I shall analyse the results of this study in terms of $\mathrm{Sh}_{plug}$ using the following definition:

$$\begin{aligned} \mathrm{Sh}_{plug} &= \frac{k_{L,lm} d_i}{D} \\ &= \frac{\frac{\dot{V}_{tot} d_i (C_\alpha - C_\omega)}{A_w D}}{\frac{(C_{w,\alpha} - C_\alpha) - (C_{w,\omega} - C_\omega)}{\ln\left(\frac{C_{w,\alpha} - C_\alpha}{C_{w,\omega} - C_\omega}\right)}} \end{aligned} \tag{1.41}$$

By introducing $C_{w,\alpha} = C_{w,\omega} = 0$ and

$$\frac{\mathrm{Gz}_{tot}}{4} = \frac{\dot{V}_{tot} d_i}{A_w D} \tag{1.42}$$

where $\mathrm{Gz}_{tot}$ is the Graetz-number of the two-phase flow, we obtain:

$$\mathrm{Sh}_{plug} = \frac{\mathrm{Gz}_{tot}}{4} \ln\left(\frac{C_\alpha}{C_\omega}\right) \tag{1.43}$$

It is also useful to express the enhancement of mass transfer in bubble-train flow in relation to single-phase mass transfer in terms of an enhancement factor E:

$$\mathrm{E}_{process} = \frac{\mathrm{Sh}_{process}}{\mathrm{Sh}_{singlephase}} \tag{1.44}$$

where both Sherwood-numbers refer to the same liquid flow rates. E is useful, since $\mathrm{E}_{process} > 1$ is a straightforward criterion for process enhancement by bubble-train flow.

An enhancement factor $\mathrm{E}_{plug}$ for mass transfer from an individual plug may be defined analogously:

$$\mathrm{E}_{plug} = \frac{\mathrm{Sh}_{plug}}{\mathrm{Sh}_{singlephase}} \tag{1.45}$$

In this case, however, $\mathrm{Sh}_{singlephase}$ should be determined using the same velocity as the plugs rather than the superficial liquid velocity as in equ. 1.44. This avoids a dependence of $\mathrm{E}_{plug}$ on the void fraction $\epsilon$.

Finally, it must be conceded that the above analysis assumes a flow pattern with a single plug and bubble size. In reality, a spread of sizes is far more likely. However, the necessary extension of $\mathrm{Sh}_{plug}$ to take account of this fact will be deferred to Section 3, because it requires knowledge of the sensitivity of mass transfer to bubble and plug lengths.

## 1.5 Summary

The conclusions drawn from the theoretical considerations can be summarised as follows:

The results of this study will be applicable to capillary flows with $\mathrm{Bo} < 0.22$, which, for typical fluids, translates into an upper limit for the tube diameter of approximately 3 mm. It will further be limited to the region of stable bubble-train flow, which implies a superficial Reynolds-number within approximately $\mathrm{Re} < 1000$ and a flow ratio $\dot{V}_{gas}/\dot{V}_{liquid} < 1$. Under these circumstances, the thickness of the liquid film between bubble and wall will not exceed approximately 3% of the tube diameter.

The geometry of the bubbles can be approximated as a capsular shape with a cylindrical body and hemispherical caps.

The pattern of flow is characterised by a division into two distinctive regions: a film region at the wall that completely flows past the bubble and an inner region that recirculates between two bubbles. There is no convective exchange between these two regions. The position of the streamline separating the two regions is determined solely by the thickness of the liquid film.

The entire problem of radial mass transfer in bubble-train flow can be expressed in terms of seven dimensionless groups. Where applicable, the log-mean values will be used. In the case of the Sherwood-number, a careful distinction must be drawn between a plug- a the process-oriented formulation.

The objective of this study is to develop a correlation between the governing groups of the form

$$Sh_{plug} = f\left(\mathrm{Re}, \mathrm{Sc}, \gamma, \beta, \delta, \zeta\right) \tag{1.46}$$

# 2

# Experimental and computer-numerical study

## 2.1 Outline of the strategy employed in the present study

In this section, I shall briefly discuss the available methods of modelling physical systems such as bubble-train flow. The aim is not to present a comprehensive treatise on modelling, but to outline the train of thought that led to the modelling strategy employed in the present study.

### 2.1.1 Modelling physical systems

The state of a physical system can be described by a set of values of its characteristic variables. The present system of bubble-train flow, for example, can be described by a distribution of local velocity and concentration values and their evolution over time. Modelling such a system implies creating a set of mathematical expressions that deliver values for the characteristic variables of the system that are sufficiently precise for an intended application[1].

If the mathematical model consists of a single equation and is explicit in the dependent variable, it is often referred to as a correlation. Correlations are a class of models particularly useful to the engineer, since they lend themselves to deriving quick estimates

[1]Speaking tongue-in-cheek, "sufficient precision" is the pragmatic answer of an engineer to the philosophical question of "exactness" in science.

of complex systems. The aim of the present study is to develop such a correlation for the rate of radial transport in bubble-train flow.

A good model can fully substitute the experimental examination of a system: Both model and experiment deliver a set of values for the variables describing the system. A good model, however, does so with far less effort and with greater flexibility than the experiment can. The use of models to describe physical systems has therefore become the corner stone of all applied sciences.

There are three routes to modelling a physical system (Fig. 2.1):

The first is the theoretical approach which is deductive in nature and involves applying first principles to the problem. First principles are fundamental, general "laws of nature" such as the principle of conservation. Applying theses principles involves adapting their general mathematical representation to the particular circumstances and boundary conditions of a given problem. Typically, the result is a set of partial differential equations (PDEs) for the governing variables. The model of the physical system is the analytical solution of the set of PDEs, which I shall refer to as the first principles-model.

In principle, this approach leads to very precise models with a well-defined scope of applicability. In practise, however, there are two major drawbacks to this method.

First of all, many of the complexities of real systems cannot yet be described in terms of first principles. This problem typically arises when the macroscopic behaviour of a continuum results from interactions at the molecular level. Examples for this problem are legion, ranging from such basic phenomena as viscosity or diffusion to complex issues such as adsorption, reaction or the behaviour of mixtures. Lacking a set of usable first principles, a host of empirical closures have been developed to describe these phenomena - often based on simple linearisations. Using them in modelling introduces much uncertainty as to the precision and applicability of the model and thus partially defeats the point of the first principles approach.

Secondly, general analytical solutions to PDEs are known only for the simplest systems and even moderate geometric or physical complexity typically renders the PDEs analytically unsolvable. This constraint is often overcome by assuming a simplified geometry or neglecting inconvenient features of the system in order to obtain solvable PDEs. The resulting model obviously falls short of reality and may prove insufficient, if the neglected features were essential. Furthermore, the solution to many PDEs take the form of implicit infinite series. While these solutions are analytical in the strict mathematical sense, they are anything but handy engineering tools.

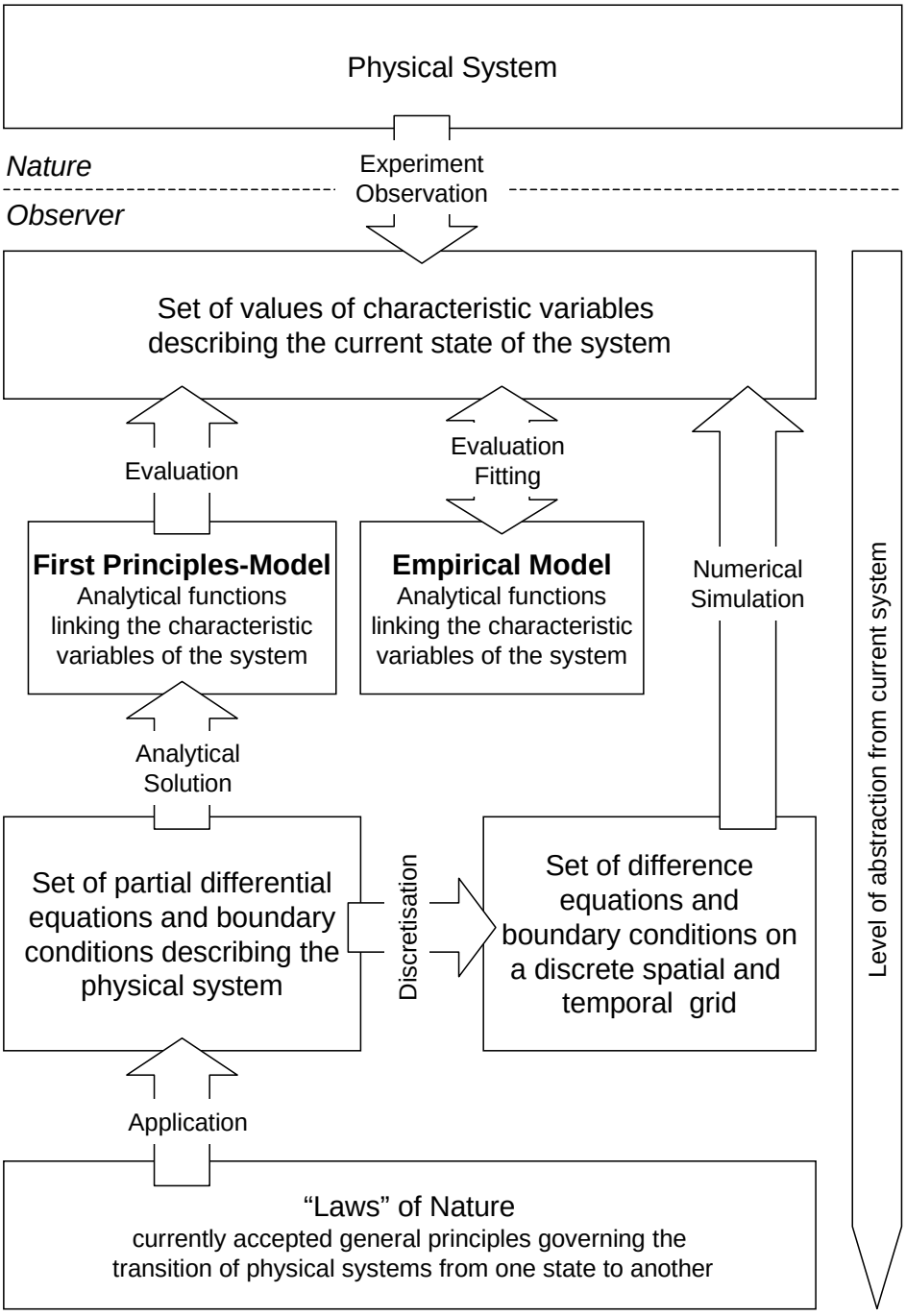


Figure 2.1: Schematic representation of the two available routes to modelling physical systems.

The second route to models takes an empirical or semi-empirical approach and is inductive in nature. A suitable mathematical expression containing one or more free parameters is fit to a set of data obtained by experiment. The structure of the mathematical model can be found either by hypothesising the mechanisms underlying the observed physical phenomena and casting them into an equation (semi-empirical or mechanistic approach) or by selecting an arbitrary function that qualitatively renders the same behaviour as the physical system does (empirical approach). The advantage of this route is that the complexity of the model can be tailored to the requirements and thus even complex physical systems can be rendered by moderately complex and therefore easy to use models. The drawback of this approach is that the quality of the model depends on the size of the available data set, and obtaining large data sets by experiment can be a very extensive task. Furthermore, the model can only be trusted within the scope of the underlying data. Outside this parameter space, semi-empirical models will sometimes render reliable results while empirical models will not.

The third route to modelling is the numerical simulation. Initially, this follows the same route as the analytical approach up to the point where the problem is expressed in terms of a set of PDEs. Instead of attempting to solve the PDEs analytically, however, they are discretised, i. e. replaced by the corresponding difference equations which are formulated at discrete points in the physical domain. Thus each PDE is replaced by a system of algebraic equations, one for each discrete point, resulting in a very large set of simultaneous equations. This system of algebraic equations is in essence the actual model of the physical system. For sheer size, however, the model cannot be solved analytically for the governing variables. Instead, one resorts to numerical solution or simulation, which lends this method its name. While the recent advances in the design of digital computers have made this approach feasible for many problems, computational power remains a serious constraint. Thus, compared with the models derived by the previous two methods, numerical models are exceedingly cumbersome to evaluate. This drawback is offset, however, with a key advantage: transforming the problem from calculus to algebra overcomes the limitation of the analytical approach to solvable PDEs without incurring the limitations of the (semi)empirical approach. In fact, the level of detail included in the model is limited only by the available computational power.

### 2.1.2 Development of a modelling strategy

The first principles-route to modelling the present system was not attempted for several reasons. The results of Duda and Vrentas [9, 10] show that far-reaching simplifications of

the geometry are required in order to obtain a solvable system of PDEs (see discussion in introduction). Furthermore, they studied heat transfer and included transport through the bubbles into the liquid. This boundary condition would require changing for the case of mass transfer and it is unclear whether this would affect the solvability of the PDEs. An attempt could be made to overcome these limitations, but the results would hardly warrant the effort. As Duda's and Vrentas' work illustrates, the analytical solution to PDEs on a cylindrical geometry is given by implicit infinite series. The evaluation of such equations is a formidable task in its own right and hardly meets the expectation of easy applicability which is thought to be the merit of analytical solutions. There is no reason to assume that solving the PDEs under less simplifying assumptions will deliver an easier-to-use result.

Since a numerical simulation does not lead to an analytical correlation by itself, only the empirical approach to modelling remains. This approach involves two steps: the generation of a data set and the development of a correlation for the data.

In the present case, the required data set consists of the Sherwood-number of the system as a function of the other dimensionless groups. As the dimensional analysis in section 1.4 showed, there are six independent dimensionless variables. In order to create a model that is valid over a large range of these groups, data has to be generated for the same range and with sufficient resolution. Given the number of independent variables, the required number of data points can become very large. For example, choosing only ten different values for each variable would result in a data set with $6^{10}$ points. Even after employing methods such as a sensitivity analysis to reduce the number of required data points, it is obvious that a method of automated data generation has to be found.

While an automated experiment could be a solution, it became clear early on that the available experimental methods posed a sufficient challenge even without automation. The step from manual experiment and analysis to automated operation therefore seemed too costly both in time and funds.

The alternative is to employ a numerical simulation to generate the necessary data. Since the numerical calculation of each data set follows the same method and differs only in the initial and boundary values, the problem lends itself ideally to automation on a computer. I therefore decided to employ the numerical method to generate most of the data.

At present, however, numerical methods alone are not considered sufficiently reliable to be used without experimental verification. There are a number of reasons for this:

Firstly, the discretisation of the PDEs and the subsequent interpolation of values between grid-points is merely an approximation of the real system and thus a source of error. In particular, hydrodynamic effects that are smaller than the size of a cell on the grid

will not be resolved. This affects the numerical study of turbulence worst, but can also affect the study of laminar systems such as the present one. The circulation effects and the partitioning of the stream at the stagnation point on the bubble are computationally expensive to resolve although they probably play a key role in determining mass transfer.

Secondly, digital computers calculate with finite precision. Every calculation thus incurs a truncation error. While the individual error is very small, the sum of errors over the many thousands of computations involved in calculating just one data point can add up to produce a significant error.

Thirdly, the numerical calculation is based on a simplified rendering of the physical system. In order to keep the calculation manageable, assumptions are made as to which natural phenomena have no influence on the results and can thus be neglected. For example, the physical properties of the system such as viscosity, density and diffusion coefficients are typically assumed to be constant, geometrical uniformity of the capillary is assumed and complex effects such as surfactants at interfaces are neglected for want of suitable models. Since these effects are omitted from the underlying equations, they cannot be rendered by the numerical calculation. If the assumption was wrong that the omitted effects are insignificant then the results of the calculation will be physically wrong - even if they are algebraically correct. The only method to detect such errors in the assumptions is by experimental verification.

It was therefore necessary to run a set of experiments in addition to the numerical study in order to generate a limited set of quality data with which to verify the numerical results. If the experimental and numerical data coincide, then the numerical data without direct experimental counterparts will be assumed to be correct as well.

The second step in (semi)empirical modelling is to design the mathematical framework of the correlation. The objective is to find as simple a mathematical expression as possible that can be fit with as few free parameters as possible to the data set and then render the data with as small an error as possible. The two basic approaches to this challenging task - mechanistic and empirical modelling - have already been discussed above. The choice of method will be deferred to Section 3.6.

## 2.2 Experimental examination

### 2.2.1 Measuring mass transfer in capillary tubes: a survey of available methods

The objective of the experimental study is to obtain a sparse set of data for mass transfer in bubble-train flow spanning a wide range of the governing variables as a reference for verifying the numerical simulation. For this purpose, an experimental procedure is required that allows the precise measurement of the radial transport velocity in the capillary.

The principle obstacle to be overcome in designing such a method is the inaccessibility of the radial transport velocity in the liquid to direct measurement[2]. The reason is that sustained mass transfer to the capillary wall requires the driving concentration gradient to be maintained by an additional effect at the wall. This can include chemical reactions, dissolution, solidification or permeation. Thus the observed rate of mass transfer to the wall depends on both the radial transport velocity in the liquid and the velocity of the effects at the wall and both rates are lumped into one experimental observation.

This is a problem frequently encountered in mass transfer studies and a host of experimental and statistical techniques have been developed to solve it. The most common and straightforward approach is to devise an experiment in which the rates of all interfering effects are so high that their influence on the experimental observation becomes negligible compared with the principle mass transfer step being studied. A literature survey of such methods brought several techniques to light that can be applied to the present problem of liquid-solid mass transfer inside capillaries [3]. The methods fall into three groups.

The first group is based on the dissolution of the solid. If the solid is sparingly soluble in water, then the rate of dissolution is governed by the mass transfer step in the liquid. Suitable solids include benzoic acid [32], salicylic acid or 2-naphtol [33], adipic acid [34] or transcinnamic acid [35]. The advantage of the dissolution method is that only one solute is involved, whereas the methods discussed below involve several solutes with all the possible ramifications for mass transfer. Furthermore, the chemically mild aqueous solutions allow tailoring the viscosity by adding glycerine or another viscous polyalcohol [36]. A major disadvantage is that the solute concentration spans the entire range from saturation at the

[2]This situation may change in the near future by the application of non-invasive, high-resolution imaging techniques such as nuclear magnetic resonance imaging (NMRI) to measure local flow patterns and concentration profiles in liquids [30].

[3]For an extended overview with many references, see Poulson and Robinson [31].

wall to infinite dilution in the bulk liquid, so that the assumption of an ideal solution no longer holds.

In this group, the dissolution of benzoic acid in water appears to have been used most often. Besides the advantage of its mild chemical properties, solid benzoic acid can be fashioned into small shapes quite easily. The manufacture of large bodies is difficult, however, owing to the acid's contraction during solidification[4]. As a result, the method has been used most frequently to study mass transfer between small spheres and a liquid, such as that which occurs in ion-exchange beds or fluidised beds of solid catalyst particles [33, 37, 38].

Besides these numerous studies employing benzoic acid spheres, several reports of the use of benzoic acid cylinders were found. Vašak et al. [39] manufactured benzoic acid pipes from 10 - 30 mm long segments made by compressing crystalline benzoic acid. However, they found that the observed mass transfer deviated significantly from theoretical predictions, which they attributed to the segmented nature of the pipe. An alternate approach is to cast molten benzoic acid into a tubular shape. By this method, Straight and Baasel [40] manufactured tubes with an inner diameter of 1 inch and a wall thickness of $\frac{1}{4}$ inch, while Irandoust and Andersson [41] produced 17 cm tubes with an inner diameter of 2 and 4 mm. My attempt to adopt this procedure for the manufacture of capillaries with 1 mm inner diameter failed, however, because the benzoic acid tube unvaryingly fractured during solidification. While the cited authors apparently did not encounter this problem, Straight and Baasel report considerable experimental problems owing to counter diffusion of water into the benzoic acid cylinder, the water flux being of the same order of magnitude as the flux of benzoic acid. Furthermore, Irandoust and Andersson report a significant deviation from theory caused by the concentration-dependent variation of the acid's diffusivity. In view of these difficulties, the method was not further pursued in this study.

The second group of methods employ a fast chemical reaction at the solid-liquid interface. As long as the chemical reaction is much faster than the mass-transfer to the wall, the turnover will depend entirely on the liquid side mass transfer. Such conditions can be achieved by fixing a heterogeneous catalyst to the solid. An example is the enzyme-covered tube developed by Horvath [8] et. al, which was employed to study precisely the same mass transfer problem that this study is addressing. In spite of its apparent suit-

[4]Alternatively to manufacturing solid benzoic acid shapes, a shape made of a third material can be coated with benzoic acid [37]. While this does allow greater geometric flexibility, it is difficult to assure an even coating. Also, the coating can be worn-off rapidly in places of high mass transfer, resulting in erroneous measurements.

ability, this method was not adopted for lack of experience in handling and immobilising enzymes. [5]

The third group combines the first two methods and uses dissolution by chemical reaction at the wall. The wall reacts rapidly with a solute in the liquid phase and the products dissolve in the liquid, thus maintaining the reactivity of the wall. If both the chemical reaction and the dissolution of the products are fast enough, the process becomes governed by mass transfer alone.

Research into metal corrosion has given rise to a number of such methods, including the dissolution of iron, copper and nickel [31] in hydrochloric acid containing ferric ions. The ferric ions reduce to ferrous ions while oxidising the metal wall and the reaction can be shown to be rate-limited by mass transfer of the ferric ions. Other methods reported are the dissolution of carbon steel in concentrated sulphuric acid [43], where the mass transfer of dissolved ferrous sulphate is limiting, or the dissolution of zinc in an acidified iodine solution [44].

All these methods potentially suffer from the complexities of multi-ionic solutions, such as ionic migration, which can result in a serious departure from ideal Fickian diffusion. Another disadvantage is the difficulty of varying the viscosity of the system, since typical additives such as glycerol react with the chemically aggressive solutions. Furthermore, as was found in the present study and mentioned here in hind-sight, the metal ions entering the solution at the solid-liquid interface can increase the local density, leading to natural convection that disrupts the intended transport regime. On the other hand, manufacturing techniques are well established for the mentioned metals and a wide range of semiproducts made from them are available off-the-shelf. Thus the considerable difficulties in fashioning complex shapes from obstinate materials such as benzoic acid are avoided.

A market survey revealed that of the above-mentioned metals, capillary tubing made of copper alone is available off-the-shelf and thus the choice is between two copper dissolution methods: The method according to Gregory and Ridiford [45] uses a solution of potassium dichromate in sulphuric acid to dissolve the copper, while, more recently, Poulson and Robinson [31] suggested the use of dilute hydrochloric acid with ferric ions for the same purpose.

[5] A further method belonging to this group was conceived by the present author: Membranes made of *Nafion* (trademark of *Du Pont Corp.*) are known to behave as very strong solid acids (*super acid*, [42]) and can substitute liquid acid catalysts for reactions such as esterifications. Thus an alcohol solution and a Nafion-coated solid could possibly be used to study mass transfer. This method was not studied any further, however, not least for lack of suitable Nafion capillaries, and it is mentioned here merely for the record.

For two reasons, I chose Gregory's and Ridiford's method for this study. In the four decades since the original publication, considerable experience in using the system has been documented in the literature and the key-parameters of the system, such as the diffusion coefficient of the dichromate ion appeared well established [38, 46, 47, 48]. By contrast, the latter method still suffers from uncertainties in this respect, as Poulson and Robinson report themselves. Secondly, it is an established fact that samples gathered by the aforementioned method can be analysed by spectral photometry [49, 50, 51], which allows rapid sample processing with reasonable accuracy. It is at present unclear, whether the same holds true for the latter method.

As a final remark, the chosen experimental system appears to fall short of the requirements by not allowing the adjustment of its viscosity and thus the variation of the Schmidt-number and the film thickness. An early sensitivity analysis with the aid of the numerical simulation showed, however, that in the present system the Schmidt and Reynolds-numbers are grouped together (see Section 3.3). It is therefore quite sufficient to vary Re while keeping Sc constant.

The shortcoming that the film thickness cannot be varied independently in the experiments is alleviated by the findings of a further sensitivity study: It will be shown that the film thickness has a week influence on mass transfer provided the films are very thin. The influence of thicker films, which can occur in more viscous media or at higher velocities, cannot be experimentally resolved, which is a shortcoming I cannot deny.

### 2.2.2 The copper dissolution method

The method according to Gregory and Riddiford involves bringing a solution of 1 mol/liter sulphuric acid containing 30 mmol/liter potassium dichromate into contact with a copper surface. The dichromate anion acts as an oxidation agent and oxidises the copper according to the following over-all equation:

$$3Cu + K_2Cr_2O_7 + 7H_2SO_4 \rightarrow 3CuSO_4 + K_2SO_4 + Cr_2(SO_4)_3 + 7H_2O \qquad (2.1)$$

where chromium is reduced from $Cr^{(VI)}$ to $Cr^{(III)}$. Gregory and Riddiford showed the reaction rate to be determined by the supply of dichromate to the copper surface, which implies that the dichromate concentration at the wall is zero. Thus the depletion of $Cr^{(VI)}$ depends solely on the rate of mass transfer to the wall and the log-mean mass transfer coefficient can be computed directly from the decline in $Cr^{(VI)}$:

$$k_L = \frac{\dot{V}}{A_w} \ln\left(\frac{C_\alpha}{C_\omega}\right) \tag{2.2}$$

where $k_L$ is the steady state log-average mass transfer coefficient between liquid and wall, $\dot{V}$ is the volume flow rate of the acid solution, $A_w$ is the inner surface area of the copper tube and $C_\alpha$ and $C_\omega$ are the concentrations of $Cr^{(VI)}$ in the solution before and after contacting the wall, respectively.

### 2.2.3 Materials and experimental procedure

Initially, all experiments were performed with the 30 mmol/l solution as described by Gregory and Riddiford [45] and with 2 mm i. d. copper tubes. With this configuration, serious experimental difficulties were encountered, which will be discussed in Section 3.1. A refined experimental procedure was therefore developed, which comprises a solution 100-fold more dilute in potassium dichromate and the use of 1 mm i. d. copper tubes. All experiments used to verify the numerical results were performed with this refined procedure.

In the following, both the initial and the refined experimental procedure will be described.

For the initial experiments, one litre of feed-stock was made by adding 102.17g of sulphuric acid (95-98%, extra pure-grade) to deionised and degassed water. To this solution, 8.826 g potassium dichromate (CAS-No.: 7778-50-9, NIST standard reference material (SRM)-grade) was added. The solution was then filled-up to a volume of 1 litre with deionised water. The result was a 1 M solution of sulphuric acid with 30 mmol/l potassium dichromate, as Gregory and Riddiford suggested. For the refined system, the solution was prepared as above and then diluted 100-fold with 1 M sulphuric acid. All chemicals were supplied by Merck KGaA, Germany.

Copper tubing with an inner diameter of 2 mm was supplied by *Chromatographie Service GmbH* (Langerwehe, Germany), tubing with an inner diameter of 1 mm was supplied by *Metalle Lothmann GmbH* (Würselen, Germany). The material was certified to comply with DIN 1787 SF-Cu, implying 99.90% pure copper. The tubing was cut to lengths of 270 mm. In order to obtain a chemically uniform surface, the tubes were prepared for use by rinsing their lumen with a sequence of acetone, water, potassium dichromate solution (initial composition) and water. Each rinse lasted for 5 min during which a flow rate of approximately 40 ml/min was maintained. After the final rinse, the tubes were blown dry.

Several methods for creating a steady and defined flow of bubbles in the capillary were examined. Surprisingly, the methods described in the literature [7, 8, 18, 52], which

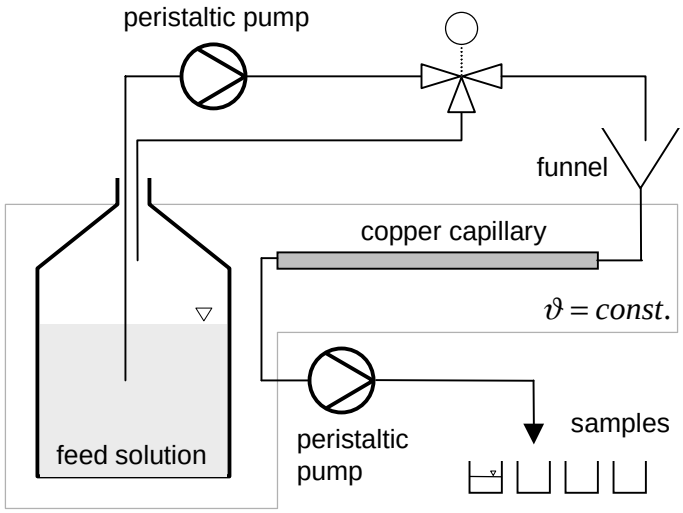


Figure 2.2: Schematic representation of the experimental setup.

essentially involve passing gas and liquid through a T-connection, did not produce a bubble-train with constant and uniform plug and bubble lengths. This was probably caused by the smaller capillary diameter used in this study, which increases the erratic effects of surface tension on bubble formation.

Instead, a new method was developed that proved to be very reliable. A finely adjustable flow of feed solution was dispensed via a magnetic three-way valve from a thin PTFE nozzle (i. d. 0.25 mm) into a funnel. The liquid was drawn from the spout of the funnel and pumped through the copper capillary. The three-way valve periodically interrupted the flow to the funnel, causing air to be sucked into the capillary and leading to the formation of bubble-train flow. By precisely timing the opening and closing of the valve by means of an electronic switch, the lengths of both the bubbles and plugs could be adjusted very finely. The method proved very stable, displaying no measurable drift in bubble and plug sizes over time.

### Equipment used

The following equipment was used (Fig. 2.2): The feed solution was pumped from a 2 l glass flask with the aid of a peristaltic pump (*MCP* peristaltic drive with a *MS/CA 4-12* head with 12 rollers, *Ismatec*, Zürich, Switzerland). The magnetic valve was manufactured by *Neuberger GmbH* (Freiburg, Germany) and was made of EPDM. The funnel was custom-made of transparent PMMA, allowing the bubble formation to be observed. The bubble-train was pumped from the funnel with a second peristaltic pump, equipped with

eight rollers (*Reglo-Analog MS-2/8-160*, *Ismatec*, Zürich, Switzerland). Since the peristaltic pump "chops-up" the bubble-train flow, it was placed at the outlet of the capillary, thus operating in suction mode. The tubing used in the peristaltic pumps was supplied by the pump manufacturer and was made of either Tygon® or Viton®. The funnel was connected to the copper capillary by means of stainless steel tubing, while the exit of the capillary was connected to the pump with semitranslucent PTFE-tubing to allow observation. All connecting tubes had the same inner diameter as the copper capillary and were interconnected with PEEK couplings. The feed flask and the copper tube were placed in a thermostatic basin which was maintained at 25°C.

The liquid flow rate was determined volumetrically. The length of the liquid plugs resulted from the ratio of the gas and liquid flow rates and was determined by photographing the flow in the PTFE tubing.

Blank test runs without a copper tube proved that there was no measurable sink for $Cr^{(VI)}$ in the system other than the copper. Furthermore, samples of dichromate solution were left open to the air for 6 hours without a measurable decline in $Cr^{(VI)}$ concentration, proving that no special precautions were required for sample handling.

Sampling began ten minutes after starting the bubble-train flow through the capillary and three samples of 2.5 ml each were drawn at 2 min intervals for every run. Several runs were performed in one batch. The copper tubes were replaced after 8 hours of operation and no significant change in inner diameter was detected[6].

### Analytical procedure

All samples were analysed spectrophotometrically with a *Varian* model *Cary 219* spectrophotometer. Owing to the strong absorbence of $Cr^{(VI)}$, all samples with an initial concentration of 30 mmol/l had to be diluted 100-fold with 1 M sulphuric acid.

Figure 2.3 shows the absorption spectrum of the diluted potassium dichromate solution. In order to rule-out an interference of other species in the spectrophotometric measurement of $Cr^{(VI)}$, the absorption spectrums of $Cr^{III}$ and $Cu^{II}$ were measured, using solutions of 0.6 mmol/l chromium chloride and 0.9 mmol/l copper sulphate in 1 M sulphuric acid. It can be seen (Fig. 2.3) that the absorption around 350 nm depends solely on $Cr^{(VI)}$. Further-

[6]Assuming complete $Cr^{(VI)}$ depletion and an even erosion of the tube over its length, operation could continue for $\sim$ 24 h before the copper wall is reduced by 0.1 mm in strength. However, far from being evenly spread over the capillary length, copper erosion is particularly pronounced close to the entry. It was therefore necessary to replace the tubes every 8 hours.

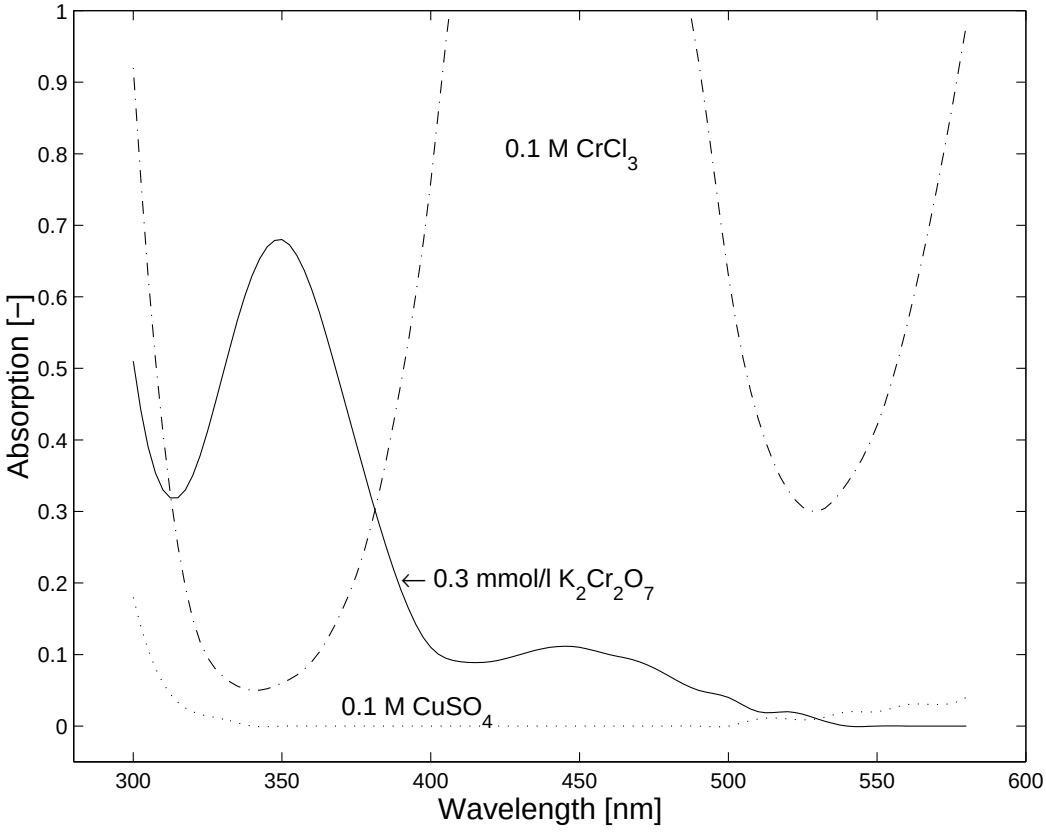


Figure 2.3: Absorption spectra of 0.3 mmol/l $K_2Cr_2O_7$, 0.1 M $CuSO_4$ and 0.1 M $CrCl_3$ in 1 M $H_2SO_4$. The absorption-peak at 350 nm is suitable for measuring the $Cr^{(VI)}$ concentration. Note that the concentrations of $Cr^{III}$ and $Cu^{II}$ are 300 times higher than will occur in the actual samples.

more, the spectrum displays a plateau at this wavelength, which makes the measurements insensitive to wavelength-drift.

This method is well-supported by the literature. In studying a very similar system[7], Goeringer et al. [49] confirm that absorption by $Cr^{(VI)}$ is strongest at ∼350 nm and is not interfered with by other species. The same authors cite further evidence for the choice of absorption wavelength (references 1-3 in [49]). Furthermore, Lee and Stewart [50] studied the oxidation of alcohols by potassium dichromate in mineral acid solutions, including sulphuric acid. They monitored the consumption of $Cr^{(VI)}$ spectrophotometrically at 349 nm.

Vincent [51], however, casts some doubt on the procedure, by observing that $HCrO_4^-$ and $CrO_4^{2-}$ absorb ultraviolet light at slightly different wavelengths, with peaks at ∼350 nm

[7]Goeringer et al studied the dissolution of copper by 1 mmol/l $K_2Cr_2O_7$ in 0.2 mol/l $H_2SO_4$.

and ∼370 nm respectively. This poses a potential source of analytical error: the $Cr^{(VI)}$ concentration in the samples is measured by comparing its absorptivity with that of reference samples with the aid of a calibration curve. If the experimental samples experience a shift in equilibrium composition in favour of $CrO_4^{2-}$ as compared with the reference samples, this would result in an incorrectly low $Cr^{(VI)}$-reading. Such a shift could conceivably be caused by copper ions, which are not present in the reference samples.

In view of these concerns and prompted by the unexpectedly low $Cr^{(VI)}$ concentrations in the initial experimental samples (see Section 3.1), the analytical procedure was subjected to a further test. Reference samples were prepared by dissolving carefully weighed amounts of copper powder (GR grade, Merck KGaA, Germany) in 100 ml flasks of fresh feed solution (30 mmol/l potassium dichromate), thus reducing the $Cr^{(VI)}$ concentration by a defined amount. Comparison of the absorption data of these samples with copper-free reference samples confirmed the predicted $Cr^{(VI)}$ concentration with negligible error (see Table 2.1). Thus the reliability of the analytical method was established beyond reasonable doubt.

| | Amount of Cu added | $Cr^{(VI)}$ concentration | |
|---|---|---|---|
| | | Theoretical | Spectrophotometry |
| Sample 1 | 42.3 mg (0.665 mmol) | 25.6 mmol/l | 25.1 mmol/l |
| Sample 2 | 106.8 mg (1.68 mmol) | 18.8 mmol/l | 18.9 mmol/l |
| Sample 3 | 173.5 mg (2.74 mmol) | 11.8 mmol/l | 12.2 mmol/l |

Table 2.1: Verification of spectrophotometric sample analysis

In summary, the analytical procedure was as follows. Prior to and after each batch of measurements, a calibration curve was prepared with samples of 0.1, 0.2 and 0.3 mmol/l potassium dichromate in 1 M sulphuric acid[8]. From each experimental sample, two sub-samples were drawn and each was individually diluted 1:99 with 1 M sulphuric acid. Both diluted samples were measured individually. If the measured $Cr^{(VI)}$ concentrations differed between the sub-samples by more than 1%, the dilution was considered to be inaccurate and two new sub-samples were analysed. Otherwise the arithmetic mean of both measurements was taken to be the correct $Cr^{(VI)}$ concentration.

[8]In all cases, both calibration curves were identical, proving the stable operation of the spectrophotometer.

### 2.2.4 Parameter domain of experiments

An early sensitivity analysis with the aid of the numerical simulation (see section 3.3) showed that mass transfer is only weakly connected to the dimensionless bubble-length $\zeta$ and the dimensionless length of the capillary $\gamma$. By contrast, the dependence on Re and dimensionless plug length $\beta$ is strong. I therefore decided to focus on these two variables in the experiments.

The experiments cover the range of Reynolds-numbers from $\mathrm{Re} = 10 \ldots 50$ and dimensionless plug lengths from $\beta = 10 \ldots 200$. Although the equipment allowed higher Reynolds-numbers, the bubbles were regularly fractured into several shorter bubbles at the connections between the various types of capillary. The result is still a bubble-train flow, however with a broad spread of plug lengths and thus of no use for verifying the simulations[9].

## 2.3 Computer-numerical study

### 2.3.1 Development of a simulation strategy

At the outset of a computer-numerical study, a set of suitable software tools has to be chosen. A prudent choice can considerably reduce the effort both in labour and in computational expense and is thus worth considering carefully.

A first basic choice is between a commercial software package and custom-written code. Today's commercial CFD-packages combine considerable versatility with ease of use by concealing many of the underlying complexities from the user. The price to pay for these advantages is the loss of flexibility that custom-written code offers by giving direct control over the source code and data sets.

The present study is a case in point for this problem. All commercial packages considered for this project are easily capable of simulating bubble-train flow with mass transfer at the wall, albeit under some uncritical restrictions. The task at hand, however, is the simulation of bubble-train flow over a wide range of the six governing variables resulting in thousands of individual simulation jobs. This is only feasible within a reasonable consumption of computational resources if the simulation is highly optimised for the task. The major scope for optimisation arises from the fact that the pattern of flow reaches steady state very rapidly and the only remaining transient quantity is the concentration

[9] It is important to stress that the observed disruption does not impede the ability of bubble-train flow to enhance mass transfer at higher Reynolds-numbers.

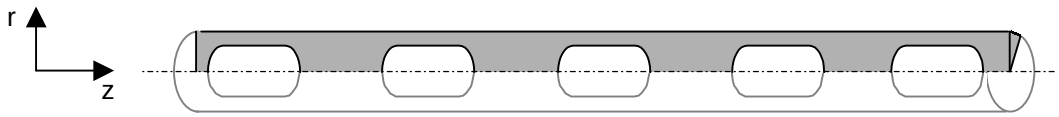


Figure 2.4: The first reduction of the computational domain to a wedge-shaped subsection of the flow (dark gray area).

distribution of the solute. It is thus necessary to solve the Navier-Stokes equations merely for the entry Section until the flow has reached steady state, after which only the solution of the conservation equation for the solute is required. Apparently, none of the commercial packages I examined offer the possibility of making use of this fact and instead doggedly re-evaluate the entire set of transient equations at every time step.

Custom written code, on the other hand, can make full use of the mentioned optimisation strategy, thus vastly accelerating the simulation. The serious draw-back is the effort involved in developing the code, in particular the solver for the Navier-Stokes equations, which amounts to reinventing the wheel.

A hybrid approach was therefore developed with the aim of combining the advantages of both tool sets. The commercial CFD-package *Flow 3D* (*Flow Science, Los Alamos, USA)* was used to solve the Navier-Stokes equations and determine the velocity field of the flow [10]. Then a custom-written tool was developed to solve the conservation equation for the solute, based on the pre-computed velocity data. The reduction in computation time compared with the use of a commercial tool only was found to be roughly fifty-fold.

### 2.3.2 Definition of the computational domain and its boundary conditions

Before the implementation of the hybrid simulation method is discussed, it is necessary to define the geometric domain of the computation. The aim is to choose a subsection of the physical domain - i. e. the capillary tube - as the computational domain so as to minimise the computational effort while still capturing all necessary detail.

The first reduction of the computational domain arises from a symmetry analysis. Assuming the capillary has a straight cylindrical geometry, all tangential velocity components are zero and the problem is two-dimensional. As a necessary consequence of tangential symmetry, the centre line of the capillary is a symmetry axis. In conclusion, the computational domain can be limited to a rectangular wedge as shown in Fig. 2.4.

[10]The reasons for choosing this package are discussed in Section 2.3.5

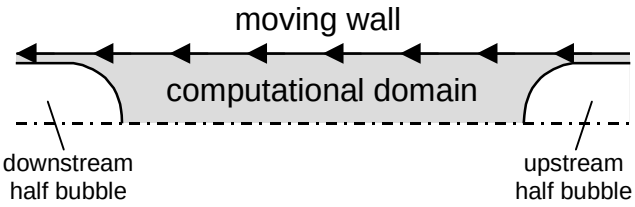


Figure 2.5: By reducing the domain to a single liquid plug, the computational effort can be reduced vastly. The boundary condition at the upwind film is, however, difficult to define.

To further reduce the size of the computational domain, it is worth examining its necessary axial extension. At first it may seem obvious to choose the entire capillary tube as the computational domain. However, closer inspection reveals this choice to be too costly. In order to obtain data over a wide range of capillary aspect ratios, the choice of a long capillary is required, leading to a vast number of computational cells in axial direction. This effect can be reduced by coarsening the grid resolution, but coarseness is limited if the local hydrodynamic effects are still to be resolved. While the resulting computational effort is still acceptable for a single simulation, it must be borne in mind that the simulation is to be repeated with varying parameters many hundreds of times. At the present stage of development of digital computers, the resulting computational expense is too high.

To solve this problem, I decided to limit the geometric domain to a single liquid plug between two bubbles, including half of each bubble at either end (Fig. 2.5). Simulation now involves following a single liquid plug on its journey through the capillary rather than simulating dozens of plugs simultaneously. While vastly reducing the computational load, this method suffers from an uncertainty. Neighbouring liquid plugs correspond with each other via the liquid film separating the bubble from the wall. Through this film, liquid flows[11] into a plug from its upstream neighbour with a concentration of solute characteristic for that neighbour. By limiting the simulation to a single plug, no upstream information is available and the concentration boundary condition at the entering liquid film is unknown.

Several solutions to this problem were examined. The simplest is to assume a complete depletion of solute in the entering film. This is plausible for long bubbles, since the film is thin and is in contact with a large wall surface resulting in a high specific surface area. For the purpose of process enhancement, however, it is obviously desirable to choose short

[11]This notion is based on a coordinate system moving with the plug. The conclusion is, however, independent of the choice of coordinates.

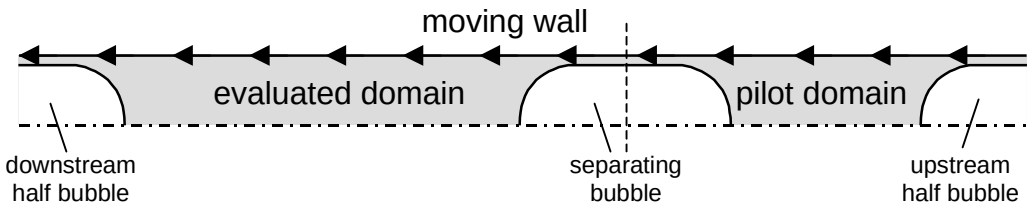


Figure 2.6: The improved computational domain: A pilot plug is used upstream to generate a defined concentration in the film entering the evaluated domain.

bubbles and thus complete depletion is not guaranteed. This was confirmed in a preliminary simulation study.

An alternate approach is to choose periodic concentration boundary conditions. In other words, the concentration in the entering film is set to that of the film leaving the plug at the downstream end. For short liquid plugs this could be a good estimate, but the error increases with plug length. As early experiments showed, the effect of mass transfer enhancement sets in already at considerable bubble distances, thus making it necessary to simulate very long liquid plugs.

A more refined approach is to extend the geometric domain to two neighbouring liquid plugs. The simulation of the upstream plug serves only to determine the concentration of the film entering the downstream plug. Mass transfer is then evaluated for the downstream plug only. Owing to the mixing effects in the plug, choosing an imprecise upstream boundary condition for the upstream plug is expected to have virtually no impact on the results. The drawback of this method is the doubling of the computational expense, especially in the case of long plugs.

Finally, a simplified version of the twin plug approach was chosen: An upstream pilot plug of fixed, short length was included in the geometric domain (Fig. 2.6). Thus the missing concentration boundary condition could be estimated at a low computational expense.

In a preliminary simulation, the latter method was compared with the full twin plug and the zero film concentration method. Both twin-plug methods yielded almost identical results which differed from the simulations with a zero film concentration. Apparently complete film depletion is an overestimate of the true situation. I have therefore chosen the pilot plug method as the less expensive of the two more reliable methods.

In summary, the following assumptions were made with regard to concentration boundary conditions (BC):

1. At the capillary wall, a solute concentration of zero is assumed (Dirichelet-type BC). This is equivalent to placing the entire mass transfer resistance in the liquid, which is the obvious choice for this study.

2. The centre line of the capillary is a symmetry-axis, which is equivalent to a zero flux or zero concentration gradient at the centre line (von Neuman-type BC).

3. The bubbles are opaque to mass transfer and thus the fluxes and concentration gradients at the bubble walls are also zero.

4. The concentration of the liquid film entering the pilot bubble can be set to an arbitrary value, as it has been shown to have little influence on the result. In order to approximate a realistic value, a circular boundary condition was chosen: the concentration in the film entering the pilot bubble was set to the value of the film leaving the downstream plug.

### 2.3.3 The choice of methods for discretisation and approximation

The hybrid method of simulation presented in section 2.3.1 requires the development of custom-written code to solve the conservation equation for the solute. While this approach requires far less effort than coding a solver for the complete set of Navier-Stokes equations, it still involves many of the steps of the latter. In this section, the choice of coordinate system, discretisation and approximation methods and numerical grid type will be discussed. The subsequent section will demonstrate their implementation to yield the algebraic system of equations. In both sections I shall draw upon the ideas and arguments presented by Ferziger and Peric [53], Versteeg and Malalasekera [54] and Patankar [55].

The conservation equations can be written in many different forms depending on the coordinate system used. Choices include orthogonal systems such as Cartesian, cylindrical or spherical coordinates and curvilinear coordinates which can be both orthogonal and non-orthogonal. Furthermore, there is a choice of fixed or moving reference systems.

The treatment of a problem can be significantly simplified if a coordinate system is chosen, in which the boundaries and symmetry axes coincide with the coordinate axes. Apart from the spherical bubble-caps, all essential features of the present system fall naturally into cylindrical coordinates. By using this coordinate system, the tangential symmetry identified in section 2.3.2 reduces the problem to two dimensions.

The problem is further simplified by choosing a coordinate system moving with the computational domain. This choice was already implicitly made by limiting the domain to a pair of neighbouring plugs.

After choosing the coordinate system, the next step is to formulate the governing equations of the problem - in the present case the equation of conservation for the solute. The choice is between a differential and an integral formulation, depending on the method of discretisation.

Discretisation serves to transform the problem from calculus to algebra. There are several methods to choose from.

The most straightforward is the Finite Difference (FD) method, by which the infinitesimal differential operators are replaced by finite difference equations, typically derived by a truncated Taylor Series expansion. The variables involved are expressed as local values at discrete points in space, which form the nodes of the numeric grid.

The advantages of the FD method are the straightforward implementation on simple geometries and the ability to enhance accuracy even on moderately fine grids by using higher order approximations. For this reason, the FD method is the basis for most commercial codes. The limitation to simple geometric grids can be overcome by elaborate multigrid (a. k. a. block-structured grid) schemes. In the present study, the transition from the cylindrical geometry of the plug to the holospherical boundaries at the bubble ends would require such treatment. A suitable multigrid construction is illustrated in Fig. 2.7.

While commercial codes automate the implementation of the FD method on multigrids, the effort of doing so in custom-written code is prohibitive. A further disadvantage of the FD method is that conservation is not necessarily enforced unless special care is taken. Since the whole purpose is to solve the conservation equation for the solute, this drawback is particularly worrying. For these reasons, I did not adopt the FD method for the present study.

The alternatives to the FD method are the Finite Volume (FV) and its close relative, the Finite Element (FE) methods. The starting point of both methods are the integral form of the governing equations, which can be derived by applying Gauß' transformation to the differential equations. The computational domain is then subdivided into finite control volumes (CVs) and the integral equations are applied to them using suitable approximations.

The advantages of the FV method are its suitability and comparatively easy implementation for complex geometries using unstructured grids (see below) and its inherent conservativity, which make it the suitable choice for the present study. The disadvantage of the FV method that higher order discretisation schemes are difficult to implement, is irrelevant for the present study, since such schemes are typically called for in turbulent flows.

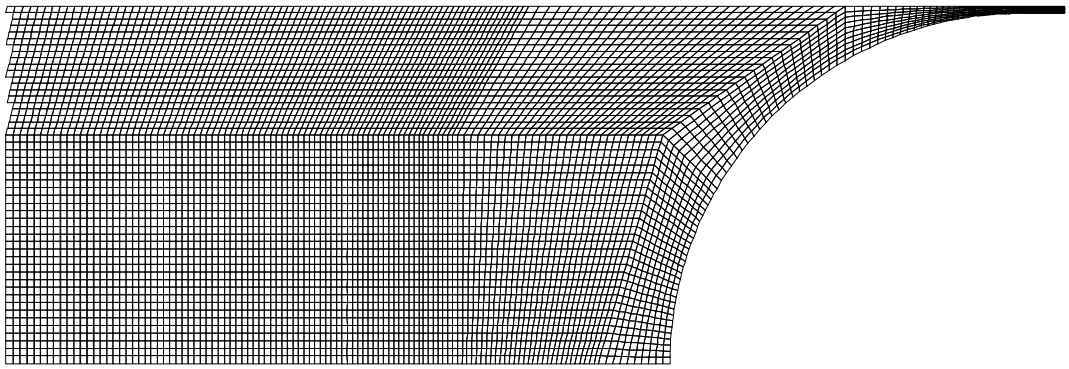

Figure 2.7: Example of a multigrid for the present study. The aim of the construction is to achieve a smooth transition between the cylindrical shape of the capillary and the spherical caps of the bubbles. The grid was developed and tested in *CFX* (*AEA Technology*, Waterloo, Canada). I am endebted to T. Jatzkowski for developing this grid.

The FE method additionally introduces weighting functions into the integral equations and determines the coefficients of the weighting functions by a minimum squares approach. For the present study, no additional advantage of this method over the FV method could be identified and it was thus not further considered.

I have thus decided to employ the FV method in the present study.

Before applying the discretisation method, suitable approximations must be chosen. For the FD method, approximations for the differential operators must be derived, while the FV/FE methods require approximation of the surface and volume integrals of the control volume. Many approximation methods are reported in the literature and many more could be conceived. The following discussion will be limited to the most frequently used approximations for the FV method.

Precisely evaluating the surface and volume integrals of the CV would require differentially resolved values of the relevant variables. In the system of finite volumes, precise values for the variables are, however, known only at the centre of each CV. Information about any other point in the CV has to be approximated.

The simplest method of approximating a volume integral is to assume the value at the centre of the CV to be the volume average value. This is equivalent to integrating over a constant and the integral is reduced to the product of the variable and the volume, making implementation very easy. Higher order methods involve assuming a shape function of the variable over the volume. This elaborate method was not explored in the present study and instead the former method was chosen.

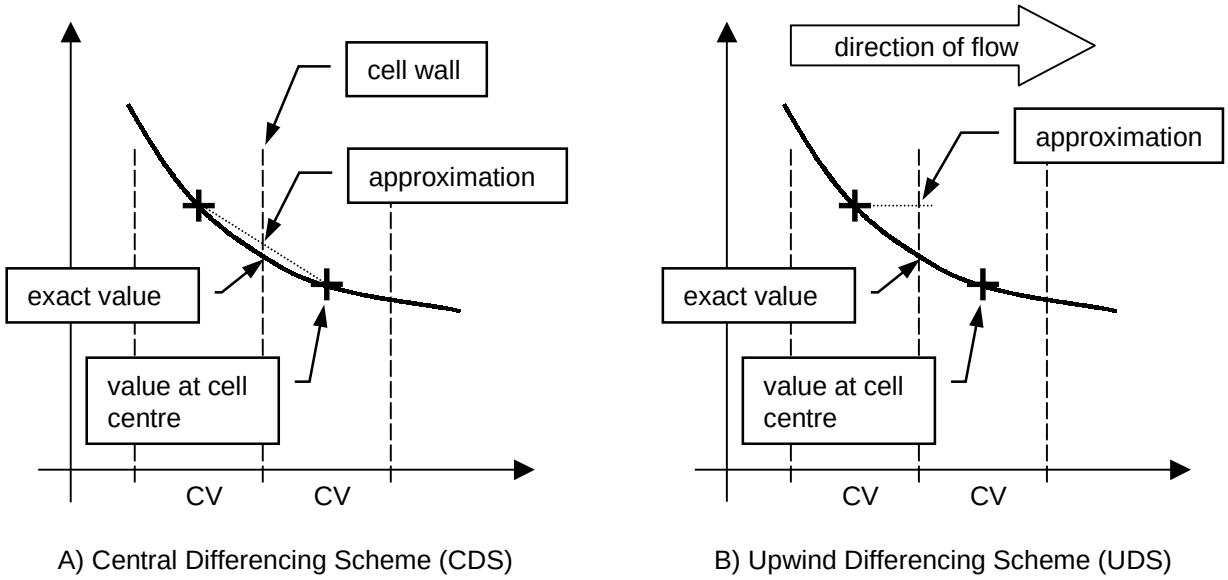


Figure 2.8: Schemes to approximate the variable values at the surface of the CVs. A) Linear interpolation (known as *Central Differencing*, CDS) B) Upwind approximaxion (UDS)

Evaluation of the surface integrals requires approximating the variable values on the surfaces of the CVs. A straightforward method is the linear interpolation of the variable values of the two neighbouring cells (Fig. 2.8, A). This method is analogous to the central differencing scheme in FD methods and is thus called CDS. The major drawback of this method is its tendency to produce oscillating results (Fig. 2.9). They are caused by applying CDS to the convective terms in the equations and are dampened by the diffusive terms. It can be shown that oscillations occur when the local or grid Peclet-number, $\mathrm{Pe}_g = \rho v d L D^{-1}$, exceeds 2, which limits CDS to slow flows with high diffusion.

A commonly used remedy for this problem is a scheme known from FD methods as the upwind differencing scheme (UDS). Under this scheme, the value at the cell wall is taken to be identical with the value at the centre of the cell from which fluid is flowing through the cell wall (Fig. 2.8, B). In other words, the upstream value is taken which gives the scheme its name.

While applying UDS to the convective terms solves the oscillation problem, it incurs the new problem of false diffusion. This effect occurs when the streamlines of the flow are not parallel to the grid lines and is equivalent to an increased diffusion coefficient (Fig. 2.10).

There are two approaches to remedy this problem: The first is to adopt a set of heuristics to weight the diffusion and flux terms depending on the local Peclet-number. Leonard's *hybrid differencing scheme* [56] and the *power law scheme* [55, p. 90] developed by Patankar

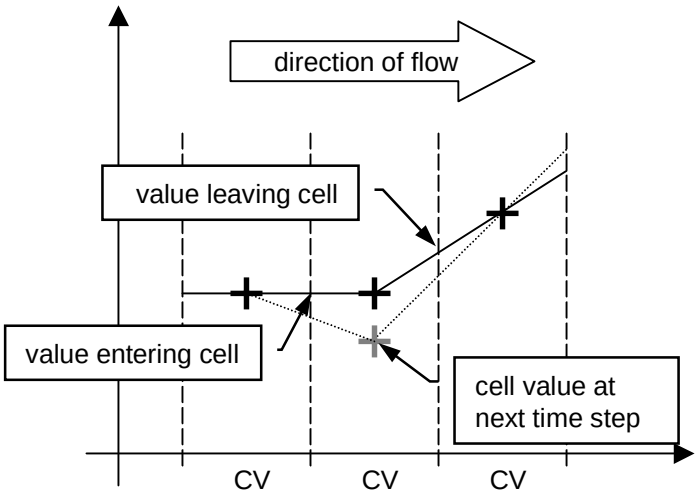


Figure 2.9: Non-physical oscillation arising in a one-dimensional flow problem as a result of Central Differencing. In the literature, such oscillations are often called *wiggles* [54, p. 109].

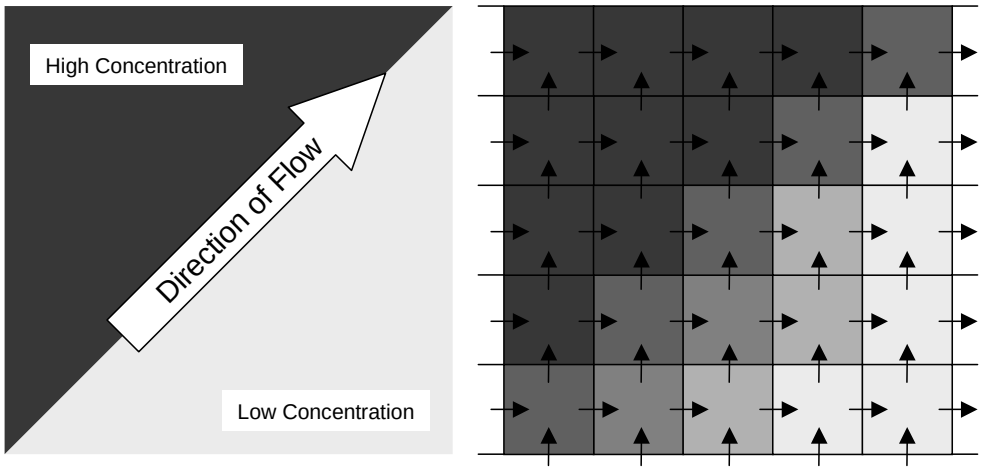


Figure 2.10: False diffusion can be illustrated with a hypothetical worst case. A real system with a step-like concentration gradient and flow parallel to the gradient (A) is being studied. In the case of zero diffusion, the concentration step would remain unaltered by the flow. Simulation of the same case using UDS with flow diagonal to the grid (B) will erroniously produce a strong mixing of the two areas, caused by splitting the diagonal flow into two orthogonal components.

belong to this group. The second approach is to use a higher-order differencing scheme, thus including more cells in the approximation of the integrals. The *quadratic upstream interpolation for convective kinetics* (*QUICK*) developed by Leonard [57] is the most widely used method belonging to this group.

The heuristic approach involves little effort to implement but only partially reduces false diffusion, whereas the QUICK scheme largely - but not completely - eliminates false diffusion at the expense of a more elaborate implementation and additional stability issues. Numerous enhancements of the QUICK scheme have been suggested in the literature [54, p. 133], but their discussion is beyond the scope of this work.

In order to avoid the considerable effort of employing a higher-order scheme, I have used the power law scheme, which is more easily implemented. The crucial question is whether false diffusion is sufficiently suppressed by this method. In the present study, flow conditions susceptible to false diffusion - i. e. flow diagonal to the grid - occur only in a small area of the recirculation zone near the bubble tips. An error introduced by false diffusion would therefore worst affect the simulation of short liquid plugs at high Reynolds- and Schmidt-numbers. However, careful comparison of the results from such simulations with experimental data revealed no systematic deviation, from which I conclude that the precautions taken against false diffusion are adequate[12].

Finally, we turn to the issue of temporal approximation. In transient problems such as the present one, the system is discretised in time as well as space, necessitating the use of temporal approximations as well as spatial ones. The simplest method of temporal approximation is the time-explicit scheme, according to which the variable values are assumed to remain constant during a time step. In other words, the actually changing variables are approximated by their initial values. Since all variable values are known at the beginning of a time step, this scheme leads to an algebraic problem explicit in the unknown variables - hence the name. The major drawback of this approach is the stability limit of the time step: unless $dt < dx^2/(2D)$ the calculation diverges and produces unphysical results [54, p. 172]. This makes the time-explicit scheme unsuitable for problems that do not require high temporal resolution, such as the slowly changing system of this study. In such cases, it may be worth using the time-implicit scheme: here all variables are approximated by their values at the end of the time step. Since these values are not available at the beginning of the time step, this scheme leads to an algebraic problem that

[12] Additional confirmation may be found in the fact that - according to Versteeg and Malalasekera [54, p. 125] - the commercial CFD package *Fluent* (*Fluent Inc.*, Lebanon, NH, USA) uses the power law scheme by default.

is implicit in the unknown variables, which makes the implementation more elaborate. The gain is a free choice of the time step limited only by the increasing loss of accuracy that longer time steps incur.

The result of the discretisation step is a set of generic algebraic equations. The step from here to a system of simultaneous algebraic equations describing the specific problem requires the description of the geometric domain in terms of a numeric grid.

The choice of numeric grid depends largely on the geometric complexity of the problem and the requirements of the discretisation method as discussed above. Numerical grids are typically described in terms of grid lines. In the case of a FD discretisation, the grid lines connect the computational nodes, whereas in a FV/FE approach they are the boundary lines of the control volumes.

The fundamental choice is between a structured and an unstructured grid. A structured grid consists of families of grid lines with the property that the lines of one family do not cross each other and cross each member of the other families only once. Structured grids can be either orthogonal or non-orthogonal (Fig. 2.11). This allows straightforward indexing of the nodes or control volumes and equally straightforward determination of the neighbouring nodes or control volumes, which greatly facilitates the formulation of the algebraic equations. This advantage is offset by the impossibility of fitting structured grids to more complex geometries. By using block-structured grids, this drawback can be partially overcome while incurring new problems at the block transitions (Fig. 2.12).

Unstructured grids depart from such constraints. The grid elements can have any shape and any number of neighbours (Fig. 2.13). While this enables the construction of grids on arbitrarily complex geometries, it can make indexing and implementing the discrete algebraic equations on the grid quite a challenge.

As already explained, the geometric domain of the present study cannot be cast into a simple structured grid. Instead the choice is between a block-structured and an unstructured grid. Fortunately, a method was found to construct an unstructured grid on the present geometry without incurring the already mentioned disadvantages of this approach (Fig. 2.14): First a structured grid with grid lines parallel to the z- and r-axes was laid over the entire geometric domain, irrespective of the bubbles. The bubbles were then cut out of the grid, rendering the adjacent control volumes irregular in shape and with between three (1) and five boundary surfaces (2). This is a typical trait of unstructured grids and the treatment of such irregularly shaped control volumes is potentially complex. In the present case, however, only the conservation equation for the solute is to be implemented and the pertaining boundary conditions make the task very simple. The bubbles are considered to

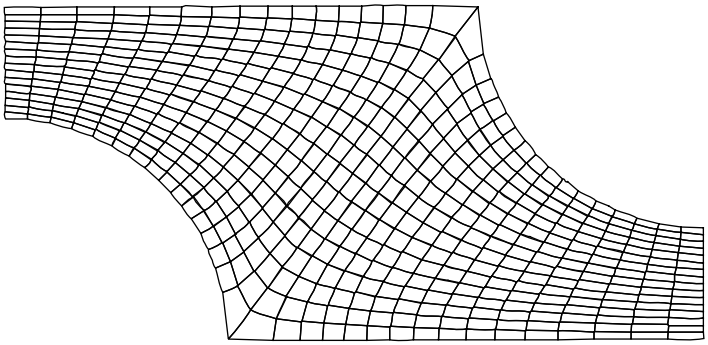

Figure 2.11: Simply shaped domains can often be treated by means of a structured non-orthogonal grid, which greatly facilitates indexing.
Figure after Ferziger and Peric [53].

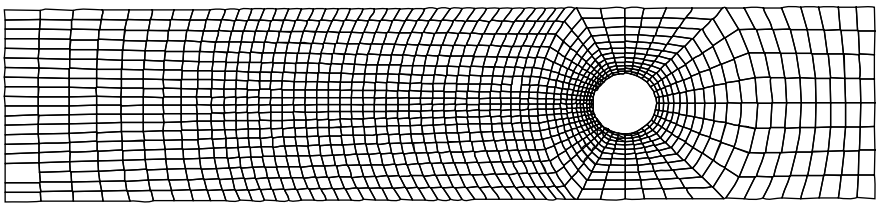

Figure 2.12: More complex domains can be discretised with the aid of several adjoining structured grids blocks. The result is called a block-structured grid. While the indexing of each block is straightforward, the interface between the blocks requires special treatment.
Figure after Ferziger and Peric [53].

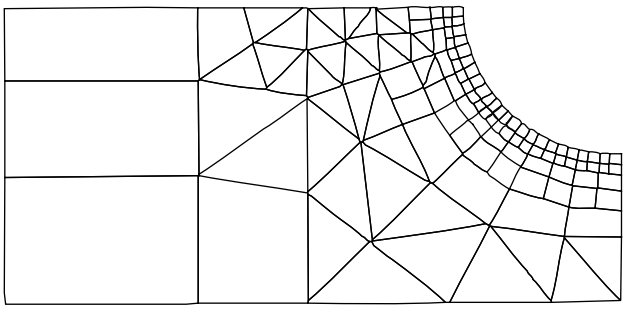

Figure 2.13: The most versatile grid is the unstructured grid, which can be fitted to an arbitrarily shaped domain. The price to pay is that indexing and recording cell neighbours can require considerably more effort.
Figure after Ferziger and Peric [53].

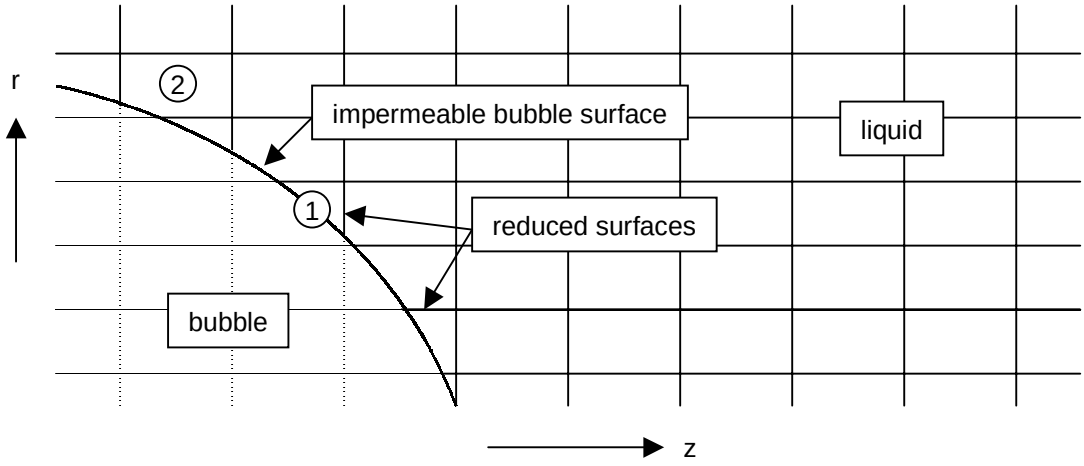


Figure 2.14: The unstructured grid developed for the present problem. The bubbles intersect the grid, cutting irregularly cells.

be impermeable for the solute and therefore the gas-liquid interface of the control volume plays no role in the implementation of the conservation equation. It simply remains to take account of the reduced boundary surfaces between neighbouring control volumes in the vicinity of the bubble, which is straightforward.

In summary, a finite volume discretisation method on an unstructured grid was adopted for the present study using an upwind differencing approximation scheme for the convective terms, central differencing for the diffusive terms and a time-implicit formulation.

### 2.3.4 Derivation of the system of algebraic equations

With the choice of methods in place, as discussed in the previous section, implementation includes formulating the integral form of the conservation equation, discretising it to obtain the generic algebraic equation and applying it to the grid by invoking the boundary conditions.

In the following discussion, the widely-used compass metaphor will be employed to index the variables (Fig. 2.15). Capital indices (N,W,S,E,P) denote the value at the centre of the corresponding cell while small indices (n,w,s,e) mark the values at the corresponding surface of the central cell.

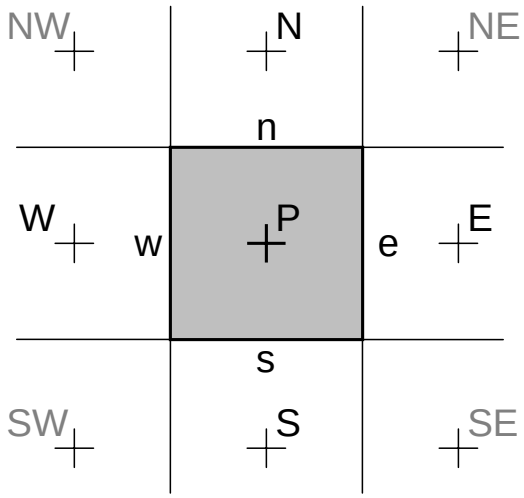


Figure 2.15: The compass metaphor is widely used to name the surroundings of a cell: values at the centre of neighbouring cells are indexed with capital letters ($N,S,E,W$), while values at the cell wall are indexed with lower case letters ($n,s,e,w$). The value at the centre of the current cell is indexed with $P$.

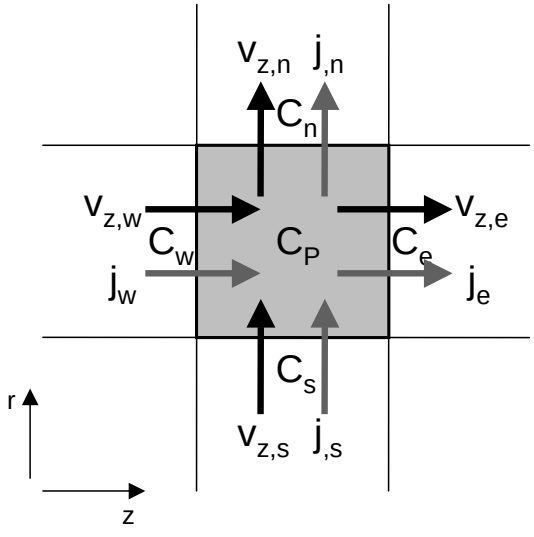


Figure 2.16: The convective (dark arrows) and diffusive (light arrows) fluxes across the boundaries of a bulk cell. By convention, fluxes in direction of the coordinate axes are defined as positive.

The integral equation of conservation for the solute can be obtained by a shell balance[13] on a control volume (Fig. 2.16). Using the time-implicit approximation, the shell balance delivers:

$$\begin{aligned} V_P \frac{C_P|_{t+\Delta t} - C_P|_t}{\Delta t} &= (v_{z,w} A_w C_w - v_{z,e} A_e C_e + v_{r,s} A_s C_s - v_{r,n} A_n C_n + \\ &\quad j_w A_w - j_e A_e + j_s A_s - j_n A_n)\,|_{t+\Delta t} \end{aligned} \tag{2.3}$$

Where the diffusive fluxes are given by Fickian diffusion as

$$j_w = -D\frac{\partial C_w}{\partial z} \quad j_e = -D\frac{\partial C_e}{\partial z} \quad j_s = -D\frac{\partial C_s}{\partial r} \quad j_n = -D\frac{\partial C_n}{\partial r} \tag{2.4}$$

Using central differencing, these expressions are discretised to

$$j_w = -D\frac{C_P - C_W}{dz} \quad j_e = -D\frac{C_E - C_P}{dz} \quad j_s = -D\frac{C_P - C_S}{dr} \quad j_n = -D\frac{C_N - C_P}{dr} \tag{2.5}$$

Next, the convective terms are approximated using the upwind scheme. This scheme requires the distinction between the two possible flow directions over the cell wall, which can be implemented with the aid of Boolean flags. The flag is set to *true* if the flow through a given face is leaving the cell and to *false* if it is entering the cell. A Boolean NOT-operator can then be used to select the appropriate concentration variable:

$$\begin{aligned} C_w &= fw\, C_P + \mathbf{not}(fw) \qquad \text{with} \quad fw = (v_{z,w} < 0) \\ C_e &= fe\, C_P + \mathbf{not}(fe) \qquad \text{with} \quad fe = (v_{z,e} < 0) \\ C_s &= fs\, C_P + \mathbf{not}(fs) \qquad \text{with} \quad fs = (v_{z,s} < 0) \\ C_n &= fn\, C_P + \mathbf{not}(fn) \qquad \text{with} \quad fn = (v_{z,n} < 0) \end{aligned}$$

Inserting the approximated diffusive and convective fluxes into 2.3 and sorting by cell concentrations delivers the generic algebraic equation:

$$C_P|_t = (a_W C_W + a_E C_E + a_S C_S + a_N C_N + a_P C_P)_{t+\Delta t} \tag{2.6}$$

with the coefficients

[13] In non-cartesian coordinates, this is possible only for the equation of continuity and not for the equations of motion and energy, as Bird, Stewart and Lightfoot helpfully point out [12, p. 83].

$$a_W = \left(-D\frac{A_w}{\Delta z} - v_{z,w}A_w\mathbf{not}(fw)\right)\frac{\Delta t}{V_P} \tag{2.7}$$

$$a_E = \left(-D\frac{A_e}{\Delta z} + v_{z,e}A_e\mathbf{not}(fe)\right)\frac{\Delta t}{V_P} \tag{2.8}$$

$$a_S = \left(-D\frac{A_s}{\Delta r} - v_{r,s}A_s\mathbf{not}(fs)\right)\frac{\Delta t}{V_P} \tag{2.9}$$

$$a_N = \left(-D\frac{A_n}{\Delta r} + v_{r,n}A_n\mathbf{not}(fn)\right)\frac{\Delta t}{V_P} \tag{2.10}$$

$$a_P = \left(1 + D\frac{A_w}{\Delta z} + D\frac{A_e}{\Delta z} + D\frac{A_s}{\Delta r} + D\frac{A_n}{\Delta r} - v_{z,w}A_w fw + v_{z,e}A_e fe - v_{r,s}A_s fs + v_{r,n}A_n fn\right)\frac{\Delta t}{V_P} \tag{2.11}$$

The implementation of the boundary conditions proved to be straightforward:

- The zero flux condition across the bubble surface is implemented automatically by setting the surface area fractions of the cell walls facing the bubbles to zero, which is done by Flow 3D.

- The zero flux condition across the centre line is similarly taken care of by the fact that the southern interfacial area $A_s$ of the southern most cell is necessarily zero.

- The circular boundary condition between the flow leaving the film at the north western corner and the flow entering the pilot bubble at the northeastern corner is implemented by wrapping the indices of the coefficient matrix (see section 2.3.5).

- The northern boundary condition requires more attention (Fig. 2.17): Simulation begins with the computational domain completely outside the capillary. Mass transfer is limited to the actual capillary tube and thus prior to entering the capillary, the wall is considered impermeable to the solute. Thus the boundary condition at the wall is a zero solute gradient. This can be achieved by setting $C_N = C_P$ which translates into the following coefficients:

$$a_N = 0 \tag{2.12}$$

$$a_P = \left(1 + D\frac{A_w}{\Delta z} + D\frac{A_e}{\Delta z} + D\frac{A_s}{\Delta r} - v_{z,w}A_w fw + v_{z,e}A_e fe - v_{r,s}A_s fs + v_{r,n}A_n fn\right)\frac{\Delta t}{V_P} \tag{2.13}$$

  As the simulation progesses, the computational domain gradually moves into the capillary tube and is subject to solute removal at the wall. The boundary condition

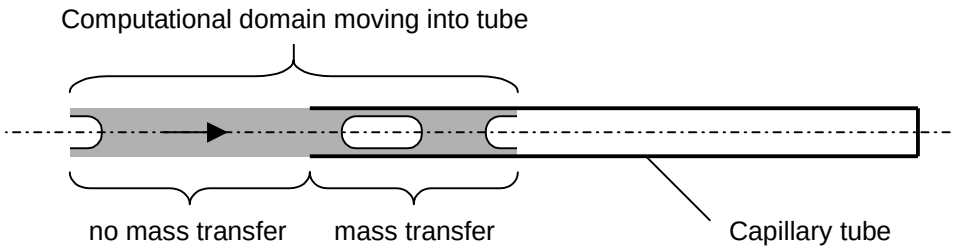


Figure 2.17: The concentration boundary condition at the wall changes as the computational domain enters and later exits the capillary tube.

now changes to $C_n = 0$ which can best be achieved by setting $C_N = -C_P$ (Fig. 2.18) and which translates into:

$$a_N = 0 \tag{2.14}$$

$$a_P = \left(1 + D\frac{A_w}{\Delta z} + D\frac{A_e}{\Delta z} + D\frac{A_s}{\Delta r} + 2D\frac{A_n}{\Delta r} - v_{z,w}A_w fw + v_{z,e}A_e fe - v_{r,s}A_s fs + v_{r,n}A_n fn\right)\frac{\Delta t}{V_P} \tag{2.15}$$

At the capillary exit, the change of boundary condition is reversed again[14]. This dynamic boundary condition is implemented by dynamically changing the coefficient matrix of the algebraic system, which will be detailed in Section 2.3.5.

Finally, the generic algebraic equation must be applied to the numeric grid. The result is a system of algebraic equations with one equation for every cell. To distinguish between cells, each is given a unique number, counting in the present case from the south western to the north-eastern corner (Fig. 2.19). Using this notation, the system of equations can be written in a compact vector form as

$$\begin{pmatrix} C_1 \\ \vdots \\ C_{n\cdot m} \end{pmatrix}_t = \mathbf{S} \cdot \begin{pmatrix} C_1 \\ \vdots \\ C_{n\cdot m} \end{pmatrix}_{t+\Delta t} \tag{2.16}$$

or simply

$$C|_t = \mathbf{S} \cdot C|_{t+\Delta t} \tag{2.17}$$

[14]Strictly speaking, it is not necessary to return to an impermeable wall boundary condition at the exit of the capillary, since the measurement of the exit concentration is not influenced by the concentration downstream. The procedure used to measure the exit concentration is explained in Section 2.3.5.

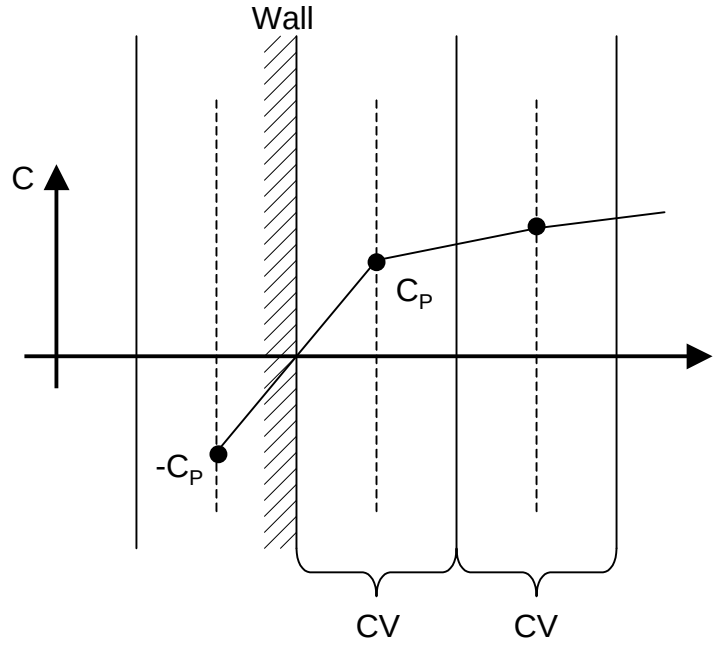


Figure 2.18: A zero concentration at the wall can be implemented by setting $C_N = -C_P$.

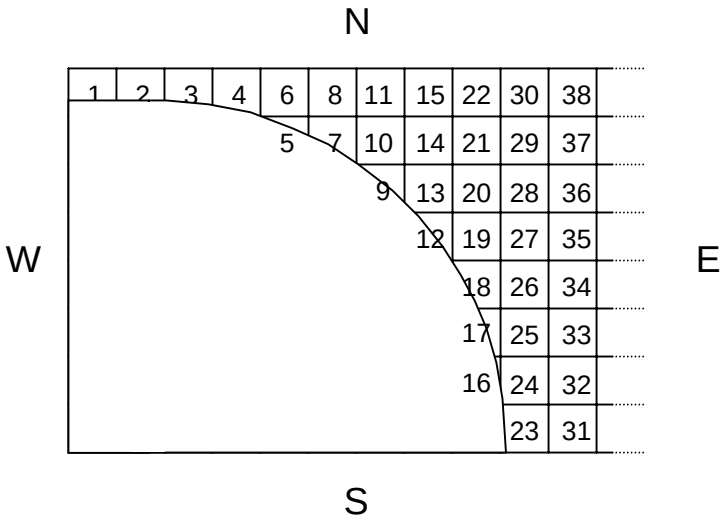


Figure 2.19: Each cell is given an index number as a unique identifier by counting from the south western to the north-eastern corner.

where each line of the coefficient matrix **S** contains the coefficients of one equation. The final step is to solve the equation for $C|_{t+\Delta t}$ by a suitable method, which will be discussed in the following section.

### 2.3.5 Implementation of the simulation

Summing up the previous sections, it can be seen that the implementation of the hybrid simulation scheme involves two steps. First, a set of fluid dynamic data describing the hydrodynamic conditions in the liquid plugs under a range of conditions is generated using a commercial CFD-package; Thereafter, a custom-written software tool is used to solve the conservation equation for the solute on the basis of the previously generated hydrodynamic data.

This section will describe some of the features of the implementation without going into a detailed discussion of algorithms.

#### Simulating the hydrodynamics

The commercial CFD-package *Flow 3D* (*Flow Science Inc., Los Alamos, NM, USA*) was chosen for the first step. It is particularly well suited to the task at hand in several respects. It allows the use of exactly the same unstructured grid as was developed for the custom-written solver (see Section 2.3.3). Therefore no translation of flow data from a block-structured grid is required, which would be an additional source of both effort and error. Furthermore, *Flow 3D* uses a staggered grid and therefore calculates the velocities at the cell faces rather than at their centres, which is precisely what will be required for the second step. Finally, *Flow 3D* also generates and exports the volume- and area fraction data that is required to describe the CVs that are partially intersected by the bubbles. These features were not found in the other available CFD-packages and thus the choice was obvious.

The following standard set-up was used for all *Flow 3D*-jobs (Fig. 2.20): the computational domain was chosen according to Fig. 2.5 - a pilot domain was not required, as the simulations did not include mass transfer[15]. The two half-bubbles were implemented as rigid hemispheres attached to short cylinders with a slip-boundary condition at the bubble

[15]It would seem obvious to include mass transfer in *Flow 3D* model in order to obtain reference data for the custom simulation. In release 7.6 , however, *Flow 3D* has a sloppy implementation of wall concentration boundary conditions: the imposed wall concentration is placed half a cell width beyond the wall and not at the wall itself. Thus the results cannot be compared with those from the custom simulation. *Flow Science* has confirmed this bug.

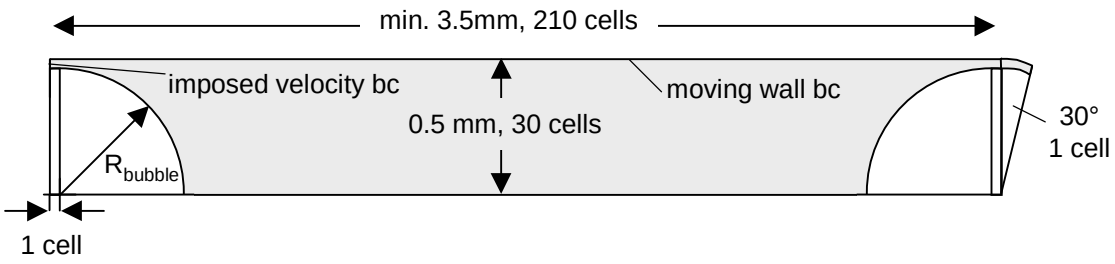


Figure 2.20:

surface. The distance from tip to tip between the bubbles was set just long enough to allow the flow to become fully laminar half way between the bubbles. The corresponding length was estimated from equ. 1.4, but was set no shorter than $3R$. The domain had a diameter of 1 mm. Since *Flow 3D* lacks the ability to detect steady state, all simulations were run for a real-time duration of two seconds, which was found to produce steady state results even for the slowest liquid velocities.

Initially, two sets of hydrodynamic data were generated. The first set used a grid with an aspect ratio of one while the second used cells stretched in axial direction to a ratio of three. The second set of data was used to simulate very long liquid plugs with a dimensionless length $\beta > 200$, where the longer cells helped to contain memory consumption. The loss of resolution in the recirculating flow near the bubble tips that is incurred by using a higher cell aspect ratio is acceptable for large values of $\beta$.

At the end of each job, the last axial and radial velocities at the CV surfaces were exported to an ASCII-file along with the surface and volume fraction data of the grid.

To make the hydrodynamic data independent of the bubble and plug lengths and at the same time more accessible to the custom solver, it was cut into five axial sections (Fig. 2.21), each comprising characteristic flow regions. Two sections with flow in the liquid film between bubble and wall (1, 5), the section of recirculation near the western (2) and eastern (4) bubble, which was defined as ending where the radial velocities had dropped below 5% of the maximum radial velocity in the domain and a middle laminar section (3). The recirculation sections were laminarised at their ends, meaning that the radial velocities in the column of cells next to section (3) was set to zero and the axial velocities were corrected to comply with continuity. The laminar sections (1, 3, 5) were each reduced to a single column of cells. Finally, the velocity data of each section were stored along with the volume and area fraction data as a double precision Matlab file.

Thus the hydrodynamic data were reduced to building-blocks, from which subsequent simulations with arbitrary bubble and plug lengths can be constructed instantly. In essence,

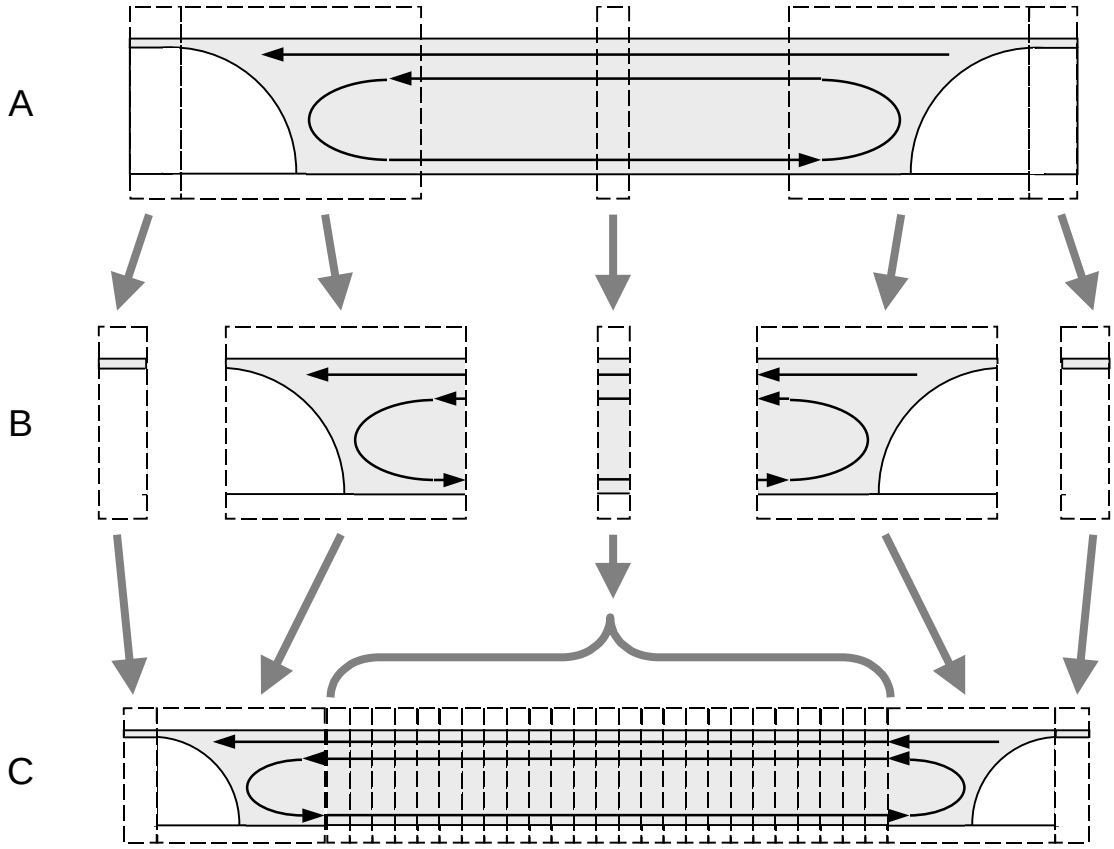


Figure 2.21: The hydrodynamic data computed by *Flow3D* is processed for use in *Matlab* by splitting it into five characteristic regions (A). The velocity and geometry data within each region is stored separately by *Matlab* (B). It can then be reassembled to a domain with any required bubble distance by repeating the central laminar region appropriately (C).

this simply involves assembling the velocity data sections in the correct order while repeating the laminar sections (1, 3, 5) as often as is required to produce the desired bubble and plug lengths. The key advantage of this method is to drastically reduce the number of required *Flow 3D* simulations by making it independent of the length ranges to be examined by the custom simulation.

As a result of the sensitivity study (Section 3.3), it became clear that special attention had to be given to very short plugs. The building-block method described above relies on the flow reaching a laminar profile somewhere between the bubbles. In the case of very short plugs this assumption no longer holds. I have therefore added a third set of hydrodynamic data based on the simulation of plugs with a dimensionless length of $\beta = 0.5....6$. These data-sets were not sliced into building-blocks but instead used directly in a batch of special mass transfer simulations.

**Simulating mass transfer**

The software package *Matlab* (acronym for *Mat*rix *Lab*oratory, *The Mathworks, Natick, MA, USA*) was chosen as the programming tool for the custom solver. Matlab is a programming language specialised in linear algebra and offers a wide variety of ready-to-use algorithms for the manipulation of large sets of linear equations. More importantly, though, Matlab offers techniques for efficiently storing very large, sparse matrices. In the present study, a grid size of $m \times n$ produces a coefficient matrix with $(m \times n)^2$ elements of which only $5 \times m \times n$ elements are non-zero. Efficient storage techniques are a prerequisite for running the custom solver on affordable hardware. It is therefore the natural choice of tool for the second part of the implementation process.

The solver for the algebraic system of equations consists of three components: an initialisation tool, which constructs the coefficient matrix $\mathbf{S}$, the solver, which performs the actual simulation by repeatedly evaluating the system of equations and returning the predicted exit concentrations from the capillary and a job-management tool, which automatically feeds the jobs defined in a job-list one by one to the solver. Both the joblist and the results file can be placed on a network storage unit allowing several instances of the simulation running on networked PCs to share the work (distributed computing), with the job-manager taking the necessary precautions for file-sharing.

Some of the features of the implementation deserve discussion in more detail:

- Simulation begins with the computational domain completely outside the capillary and ends when it has completely left the capillary again. During the entry to and exit

from the capillary, the computational domain experiences a change in wall boundary condition from impermeability to zero wall concentration and back again. This change in boundary condition is implemented by manipulating the coefficient matrix. a list is kept with the wall coefficients for both boundary conditions and these are inserted into the coefficient matrix during the entry and exit of the computational domain.

- The time step $\Delta t$ is set to such a value that the computational domain moves forward by the length of 100 cells every time step. This is possible because the time-implicit formulation of the problem removes the stability constraints from the size of the time step. The advantage is two-fold: the simulation involves fewer evaluations of the system of equations which translates into a significant acceleration compared with the time explicit formulation. Secondly, moving the domain by the length of a whole number of cells avoids the situation in which individual cells come to straddle the entry or exit of the capillary. This situation would result in two different boundary conditions in a single cell, which is difficult to implement. The step of 100 cells was chosen on the basis of a study comparing a range of possible steps and which showed a value of 100 to buy a significant acceleration without incurring detectable error.

- The cup-mixing exit concentration is measured at 50 probing sites along the length of the capillary tube. Thus, a single simulation delivers data for 50 different capillary lengths, which massively reduces the required number of simulations. The exit concentration is determined by a "gate keeper" method in which the concentrations in the cells passing a probing site are multiplied with the axial flow rates through the cells and added to a cumulative flux. Dividing the cumulative flux by the average flow rate at the end of the simulation delivers the cup-mixing exit concentration at the probing site.

- There are three possible approaches to solving the implicit system of linear equations. Firstly, the matrix can be inverted and the system solved by simple multiplication: $C|_{t+\Delta t} = \mathbf{S^{-1}} \cdot C|_t$. Secondly, the system can be solved directly, e. g. by Gauß-elimination. Thirdly, an approximate solution can be found iteratively.

  At first sight, the first method appears to be the best choice, since the inversion would only have to be performed once for the entire simulation, after which only simple, fast matrix multiplications are required for the rest of the simulation. Matrix inversion is, however, computationally so expensive that the other methods outperform the

first by far[16]. In addition, repeated inversions would be necessary as the coefficient matrix changes with every time step while the computational domain enters into the capillary.

Of the two remaining methods, the direct solution by Gauß-elimination proved faster but more memory-intensive. On the available hardware, jobs with a dimensionless plug-length $\beta < 100$ could be executed in memory. For these jobs, the system of equations was solved in three steps. First the coefficient matrix $\mathbf{S}$ was LU-factorised by Gauß-elimination with the purpose of accelerating the following steps. The factorisation has to be repeated at every time step only while the computational domain enters the capillary. Following the factorisation, the system of equations was solved by a permuted back-substitution algorithm in two steps. Matlab hides the underlying algorithms in a black-box manner and thus the implementation in Matlab code is simple:

```
[L,U]=lu(S);
y=L \ Cold;
Cnew=U \ y;
```

For jobs with $\beta > 100$, an iterative solution method had to be chosen to relieve memory constraints. The method involves two steps: an incomplete LU-factorisation is performed as a pre-conditioner to accelerate the second step, which is the iterative solution of the preconditioned problem using a biconjugate gradients algorithm. Again, Matlab hides the required algorithms and the code is similarly laconic as above.

### 2.3.6 Parameter field covered by the simulations

As far as possible, the simulations are intended to cover the entire parameter domain of bubble-train flow. We will have to introduce some restrictions, though, since the domain is open-ended with respect to several parameters. As discussed in Section 1.3, bubble-train flow is limited to a range of $\mathrm{Re} = 0\ldots \sim 1000$ and to a dimensionless film thickness of $\delta = 0\ldots \sim 3\%$. The dimensionless capillary length $\gamma$ can assume any positive value. Similarly, the dimensionless bubble and plug lengths, $\zeta$ and $\beta$, have a lower limit of 1 but no principle upper limit, although $\beta$ is limited to $\beta < 600$ by the size of the available

[16]While more efficient methods of inverting strongly banded sparse matrices may possibly resolve this problem, this path was not further explored since the Gauß-elimination method displayed satisfactory performance.

computer memory. Finally, the Schmidt-number can vary over an approximate range of $Sc = 500...2500$ for most solute-solvent systems, although outliers exist.

It is obviously not feasible to sample the entire parameter domain by numerical simulation. Nor is it necessarily desirable, since not all the parameters will influence mass transfer significantly over their entire range. The alternative is to analyse the sensitivity of Sh to each parameter. We may then run simulations of sensitive regions with a higher resolution of sampling points while sampling insensitive regions with only a sparse spread of points.

The hitch is, of course, that a sensitivity study requires precisely the kind of data that I intend gathering by simulation after studying sensitivity. I have attempted to resolve this problem by performing a set of initial, widely spaced simulations as a basis for the sensitivity analysis, followed by a more highly resolved set of simulations guided by the sensitivity study. The results will be presented in Section 3.3.

# 3

# Results

## 3.1 Initial experimental results, discussion and refinement of method

Before embarking on the experimental study of bubble train flow, a series of single phase experiments were performed with the aim of verifying the experimental and analytical procedure. Transport to the wall of a tube with laminar flow, known as the Graetz-Nußelt problem, is theoretically well-understood and very precise correlations for the Sherwood-number exist (see Section 1.1). Thus, by comparing experimental results with theory, the experimental and analytical methods can be verified.

The results are shown in Fig. 3.1 as relative exit concentrations over Gz. The solid line is the theoretical result using Stephan's equation (equ. 1.15). The data are plotted twice: once with the diffusion coefficient for dichromate reported by Gregory and Riddiford ($D = 0.907 \cdot 10^{-9} m^2/s$) and a second time with $D$ fitted to the Stephan solution ($D = 2.493 \cdot 10^{-9} m^2/s$)[1].

The correlation between theory and experiment is disappointing. The experiments display a significantly lower exit concentration and thus more vigorous mass transfer than theory predicts. The data were obtained in three independent experimental runs and each data point was measured repeatedly. Nonetheless, the spread of the data is far smaller than the deviation from the theoretical result, and the error is therefore obviously systematic.

Having ruled out an error in the analytical procedure (see Section 2.2.3), the following possible causes for the observed discrepancy remain:

[1] It is a peculiarity of the presentation in terms of the Graetz-number that the Gz-scale and not the concentration scale changes with $D$.

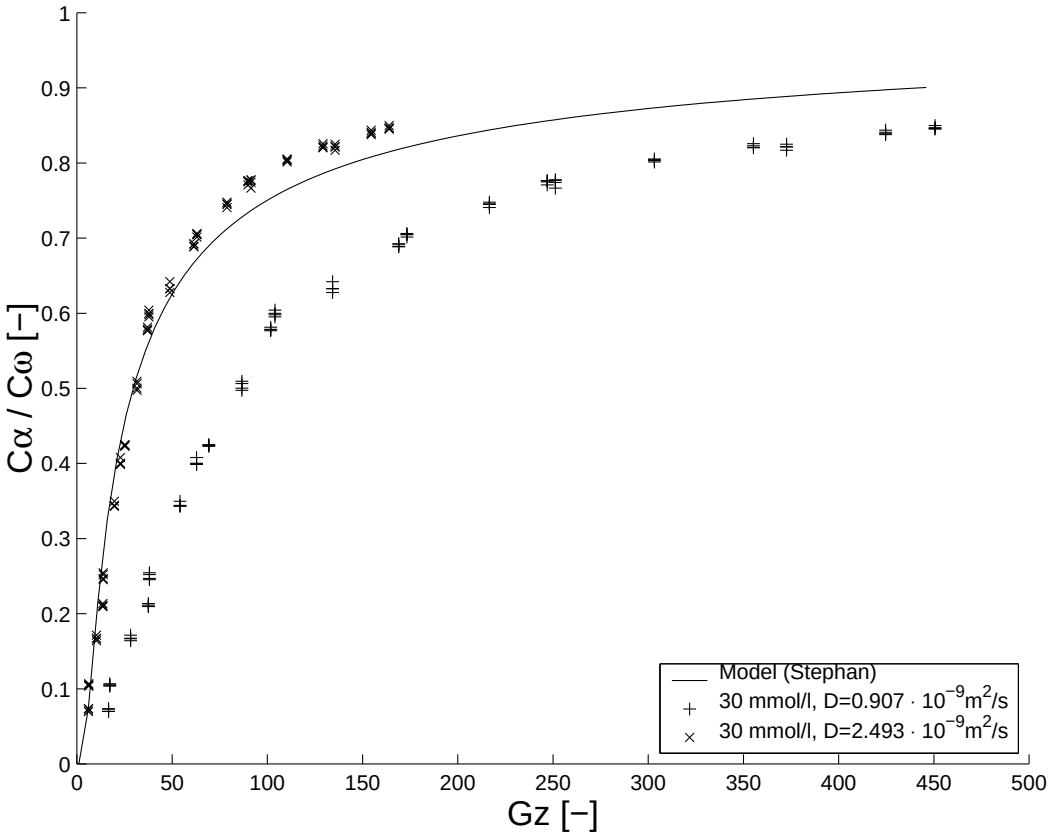


Figure 3.1: Comparison of initial single-phase results with the theoretical solution according to Stephan [11, p. 363]. Experiments were performed with 30 mmol/l potassium dichromate. Data are plotted for the literature value of $D = 0.907 \cdot 10^{-9} m^2/s$ and for the least-squares fitted value of $D = 2.2 \cdot 10^{-9} m^2/s$.

- an error in the diffusion coefficient reported in the literature;
- a shift in chemical composition near the wall resulting in more mobile $Cr^{(VI)}$ species;
- a distortion of the flow owing to a change in viscosity at wall;
- natural convection near the wall caused by a density increase owing to copper dissolution;
- the enhancement of Fickian diffusion by ionic drag effects;

I shall discuss each hypothesis in turn.

### The diffusion coefficient

The diffusion coefficient enters the theoretical solution via the Graetz-number, which is defined by

$$Gz = \frac{u \cdot d^2}{D \cdot L} \tag{3.1}$$

Gregory and Riddiford [45] measured the diffusivity by the sintered-pad technique and found $D = 0.907 \cdot 10^{-9} m^2/s$. Fitting the experimental data to the theoretical curve resulted in a diffusion coefficient of $D = 2.493 \cdot 10^{-9} m^2/s$. Not only is such an error in the original measurement of $D$ unlikely, but the resulting alignment of theory and experiment also remains unsatisfactory (Fig. 3.1). With the fitted diffusion coefficient, theory underpredicts mass transfer for low and over-predicts it for higher Graetz-numbers. Thus, only a dependence of effective diffusivity on the Graetz-number could improve the fit.

### Chemical composition

Such a dependence could possibly be caused by a shift in chemical composition of the system during the consumption of $Cr^{(VI)}$. If this resulted in an increase in more mobile species, the observed effect could be explained. Discussion of this hypothesis requires a more detailed understanding of the underlying chemistry.

The dichromate system - to give the solution proposed by Gregory and Riddiford a name - initially has three components: potassium dichromate, sulphuric acid and water. Potassium dichromate is the potassium salt of dichromic acid and so, given the amphotic nature of water, we are essentially dealing with a mixture of three acids. In aqueous solution, the acids are subject to dissociation reactions which very rapidly reach an equilibrium

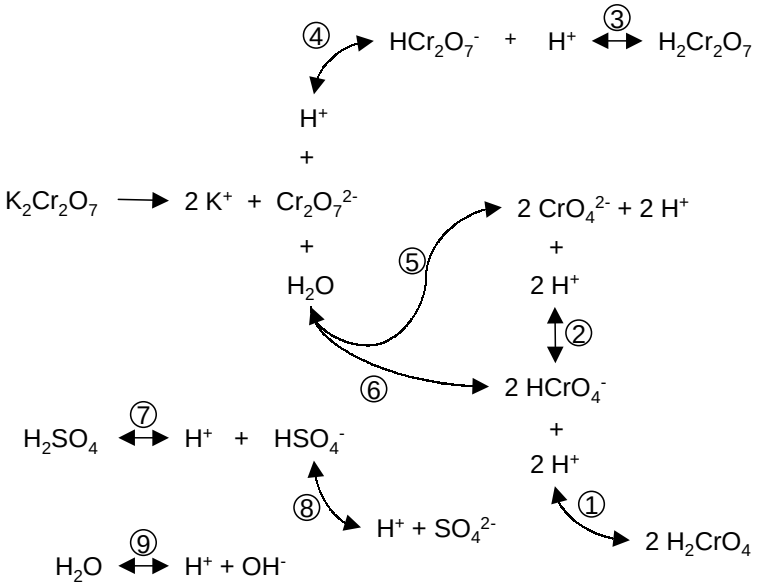


Figure 3.2: Reaction pathways of potassium dichromate in aqueous sulphuric acid.

and are linked to each other by the proton concentration in the system. Dichromic acid and sulphuric acid are bivalent acids and thus dissociate in two steps. Furthermore, the dichromate ion itself dissociates into monochromate, which in turn can re-associate in two steps to form the bivalent monochromic acid. Thus, in summary, the dichromate system comprises no less than 13 chemical species of which 9 are ionic, balanced with each other in 9 interlocking equilibrium reactions (Fig. 3.2).

Quite clearly, the proton concentration has a major influence on the equilibrium composition of the dichromate system. Since seven protons are consumed in the reduction of every $Cr^{(VI)}$-ion, a marked shift in proton concentration and therefore a shift of the overall chemical equilibrium can be expected to occur near the copper surface.

In order to study such changes in composition, the system of equilibrium reactions has to be evaluated. This requires the knowledge of the governing equilibrium coefficients, which can be found in the literature. Table 3.1 gives a synopsis of the data found there. Some uncertainty arises from the fact that not all the equilibrium constants were determined for the combination of dichromate and sulphuric acid. Lee and Stewart [50] report a dependence of $K_1$ on the proton source, which is likely to be the cause of the range of values found for this constant in the literature. No such issues are reported for the other equilibrium constants. With due caution, the following analysis should be viewed as at least qualitatively correct.

| | Chemical Reaction | | | | Source | | |
|---|---|---|---|---|---|---|---|
| | Left side | | Right side | | [58] | [59] | [60] |
| 1 | $H_2CrO_4$ | $\overset{K_1}{\rightleftharpoons}$ | $H^+ + HCrO_4^-$ | $K_1 =$ | 1.21 | **0.182** | 0.178 |
| 2 | $HCrO_4^-$ | $\overset{K_2}{\rightleftharpoons}$ | $H^+ + CrO_4^-$ | $K_2 =$ | $3.7 \cdot 10^{-7}$ | $3.24 \cdot 10^{-7}$ | $\mathbf{3.55 \cdot 10^{-7}}$ |
| 3 | $H_2Cr_2O_7$ | $\overset{K_3}{\rightleftharpoons}$ | $H^+ + HCr_2O_7^-$ | $K_3 =$ | **1** | – | – |
| 4 | $HCr_2O_7^-$ | $\overset{K_4}{\rightleftharpoons}$ | $H^+ + Cr_2O_7^{2-}$ | $K_4 =$ | **0.85** | – | – |
| 5 | $Cr_2O_7^{2-}(+H_2O)$ | $\overset{K_5}{\rightleftharpoons}$ | $2H^+ + 2Cr_2O_4^{2-}$ | $K_5 =$ | $\mathbf{3 \cdot 10^{-15}}$ | – | $2.57 \cdot 10^{-15}$ |
| 6 | $Cr_2O_7^{2-}(+H_2O)$ | $\overset{K_6}{\rightleftharpoons}$ | $2HCrO_4^-$ | $K_6 =$ | $\mathbf{2.3 \cdot 10^{-2}}$ | – | $2.09 \cdot 10^{-2}$ |

Table 3.1: Equilibrium coefficients of chromic acid. The indices refer to Fig. 3.2. The constants are defined in the customary way, e. g.: $K_1 = \frac{[H^+][HCrO_4^-]}{[H_2CrO_4]}$ Water is omitted from the equation.

Using the equilibrium constants highlighted in Table 3.1 and a specially developed pseudo-time marching algorithm[2] to solve the underlying system of non-linear equations, the composition of the dichromate system during the consumption of $Cr^{(VI)}$ was calculated (Figs. 3.3. A and 3.4. A).

The results show that in the fresh dichromate solution, 2/3 of the $Cr^{(VI)}$ inventory are stored in dichromates and 1/3 in monochromates. This equilibrium shifts in the course of $Cr^{(VI)}$ consumption in favour of the monochromates, which are the only $Cr^{(VI)}$ species left at the limit of complete turnover.

Making this shift in composition responsible for the increased mass transfer at higher $Cr^{(VI)}$ depletion implies that the monochromates have a significantly higher diffusion coefficient than the dichromates.

A review of diffusion coefficients found in the literature, which is summarised in Table 3.2, does not support this view. Vacek and Rod [39] and Iadicicco et al. [61] studied the diffusion coefficients of potassium chromate and dichromate in water. Although their results cannot be applied to the present case for lack of a background electrolyte, they support the notion that dichromates are more mobile than monochromates. Vacek and Rod suggest that this is due to the substantially lower degree of hydration of the dichromate ion which can be deduced from its lower heat of solution. Therefore the effective molecular radius of the dichromate ion is smaller than that of the monochromate, which results in

[2]To be published by the present author.

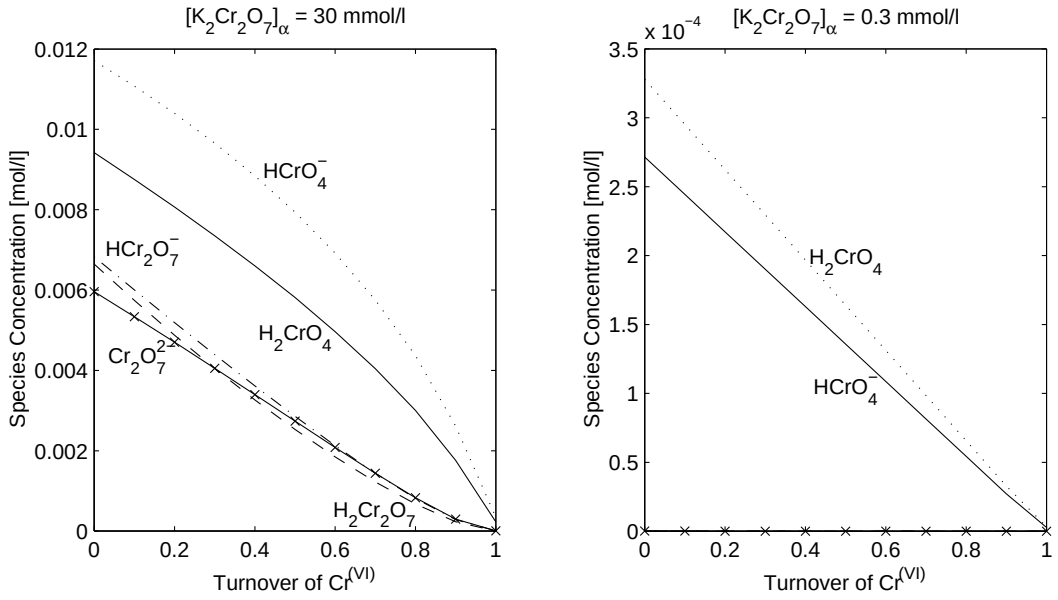


Figure 3.3: Evolution of chemical composition over chromate turnover. A) For an initial concentration of 30 mmol/l potassium dichromate (left) and B) for an initial concentration of 0.3 mmol/l (right).

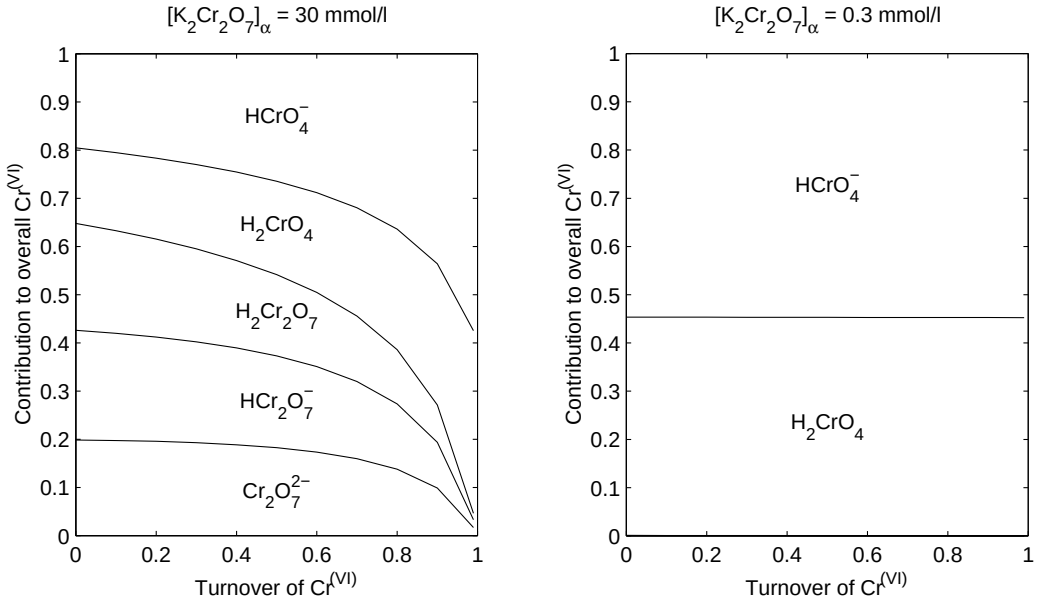


Figure 3.4: Composition of the $Cr^{(VI)}$ inventory of the solution over $Cr^{(VI)}$ consumption. The amount of $Cr^{(VI)}$ locked-up in each species is proportional to the vertical distance between neighbouring curves. A) For an initial concentration of 30 mmol/l potassium dichromate (left) and B) for an initial concentration of 0.3 mmol/l (right).

| Composition | Method | Value | Source |
|---|---|---|---|
| 30 mM $K_2Cr_2O_7$ in 1 M $H_2SO_4$ | Sintered pad cell | $9.07 \cdot 10^{-9} m^2/s$ | Gregory and Riddiford [45] |
| 30 mM $K_2Cr_2O_7$ in 0.25 M $H_2SO_4$ | Sintered pad cell | $1.16 \cdot 10^{-9} m^2/s$ | Gregory and Riddiford [45] |
| Inf. dilute $K_2Cr_2O_7$ in water | Taylor dispersion | $1.8 \cdot 10^{-9} m^2/s$ | Vacek and Rod [39] |
| Inf. dilute $K_2CrO_4$ in water | Taylor dispersion | $1.5 \cdot 10^{-9} m^2/s$ | Vacek and Rod [39] |
| Inf. dilute $K_2CrO_4$ in water | Gouy diffusiometer | $1.45 \cdot 10^{-9} m^2/s$ | Iadicicco et al. [61] |

Table 3.2: Synopsis of effective diffusion coefficients for the dichromate system found in the literature. All measurements at 25°C.

a higher diffusion coefficient. The bottom line is that the dichromates appear to be more mobile than the monochromates, which contradicts the above hypothesis.

Apart from the change in the composition of $Cr^{(VI)}$ species, the concentration of $Cr^{(III)}$ and $Cu^{(II)}$ increases in the course of the reaction. The possible effect of this change will be discussed in the following subsection.

### Viscosity

The next hypothesis postulates a distortion of the velocity profile caused by a change in viscosity at the wall, resulting in increased mass transfer. The dissolution of copper at the wall does in fact increase the viscosity. A measurement of the dynamic viscosity of samples of the dichromate system to which increasing amounts of copper were added shows an increase by 10% from fresh dichromate solution to complete $Cr^{(VI)}$ turnover (Fig. 3.5).

An increase in viscosity at the wall would, however, impede rather than enhance mass transfer, owing to reduced diffusion coefficients and reduced convection. This fact is well established and is correlated by the Sieder and Tate-correction of the Sherwood-number:

$$Sh = \left( \frac{\eta_0}{\eta_{\text{wall}}} \right)^{0.14} Sh_{\text{iso}} \tag{3.2}$$

where $Sh_{\text{iso}}$ is the Sherwood-number of an isoviscous flow[3].

[3]The correction factor was developed for heat transfer problems. Note that the correction factor is larger than unity for heated walls and smaller than unity for cooled walls. The present case of mass transfer thus corresponds to cooled walls.

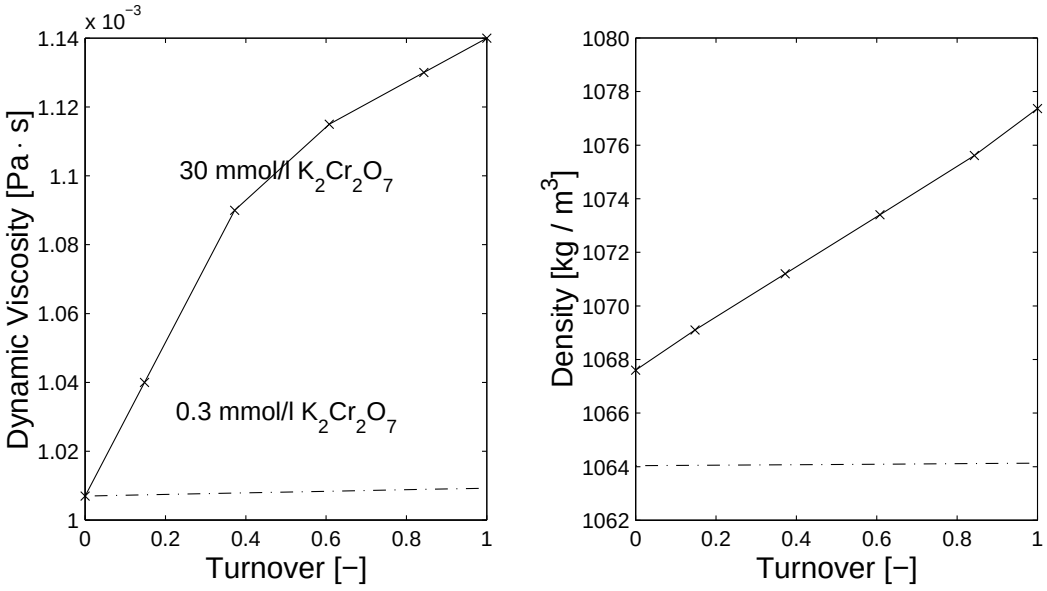


Figure 3.5: Dynamic viscosity and density over $Cr^{(VI)}$ turnover at 25°C for 30 mM and 0.3 mM initial $K_2Cr_2O_7$ in 1 M $H_2SO_4$.

### Density

The dissolution of copper at the wall causes a change not only in viscosity but also in density. The change is not substantial: density measurements of the same samples that were used to measure the viscosity show a difference of merely 0.91% between fresh dichromate solution and exhausted solution containing the corresponding amount of copper[4]. It will be shown, however, that this density gradient is quite sufficient to induce natural convection in the capillary. In a horizontal capillary, the dense outer liquid layer flows down in circumferential direction, thus inducing tangential and radial motion in the hitherto purely translational flow. This natural convection results in increased mass transfer to the wall.

This new regime of mixed forced and natural convection is known as the extended Graetz-Nußelt problem and its implications on heat-transfer have been studied extensively. Solutions for horizontal tubes have been reviewed by Shome and Jensen [62] and those for vertical tubes are reviewed by Zeldin and Schmidt [63].

[4]This would be the density at the wall only if the copper ions diffuse at the same speed as the $Cr^{(VI)}$ species. Slower copper diffusion would lead to an higher density change while faster diffusion would results in a lower increase in density. In all cases the bottom line is the same, so it is sufficient for the present purposes to assume a density increase of approximately 1% at the wall.

The degree of natural convection is generally described in terms of the Grashof- and Prandtl-numbers or their combination, the Rayleigh-number:

$$\mathrm{Gr} = \frac{g d_i^3}{\nu^2}\left(1 - \frac{\rho_{bulk}}{\rho_{wall}}\right) \tag{3.3}$$

$$\mathrm{Pr} = \frac{\nu}{\lambda} \tag{3.4}$$

$$\mathrm{Ra} = \mathrm{GrPr} \tag{3.5}$$

The usual analogy between heat and mass transfer is invoked by substituting the Schmidt-number for Pr.

The literature reports a significant departure of Nu from the standard Graetz-Nußelt solution for Ra above $10^4$. The density gradient that occurs in the present system translates to a Rayleigh-number of $Ra \approx 10^5$ for 2 mm capillaries and 30 mmol/l of $K_2Cr_2O_7$, which is strongly indicative of mixed convection. To further substantiate this hypothesis, the empirical solution to the extended Graetz-Nußelt problem developed by Shome and Jensen [62] was applied to the present system (Fig. 3.6). The comparison shows an excellent rendering of the experimental results by the extended solution, which is a first confirmation of the present hypothesis. At the same time, this finding points the way to an improved experimental procedure: by reducing the dichromate concentration to 0.3 mmol/l and the capillary diameter to 1 mm, the Rayleigh-number can be lowered to $\sim 4 \cdot 10^3$ which implies only insignificant natural convection.

To further confirm the presence of natural convection and to test the improved experimental procedure, three sets of experiments were performed:

First, the capillary was placed in a vertical position with flow from top down. Under these circumstances, natural convection works in the same direction as the forced convection, which should reduce the enhancement to mass transfer.

Secondly, the dichromate concentration was reduced 100-fold to 0.3 mmol/l. This will reduce the copper concentration at the wall and thus the density gradient and natural convection accordingly.

Finally, the capillary diameter was halved to 1 mm, which reduces Ra eight-fold and with it the strength of natural convection.

The results, summarised in Fig. 3.7, allow two conclusions. Firstly, the hypothesis that the observed deviation is caused mainly by natural convection is proven. This is best shown by the case of vertical flow, which differs from horizontal mode only in the direction of gravitational pull. This alone was sufficient to reduce the discrepancy significantly, which proves that mixed convection is a major cause of the observed deviation.

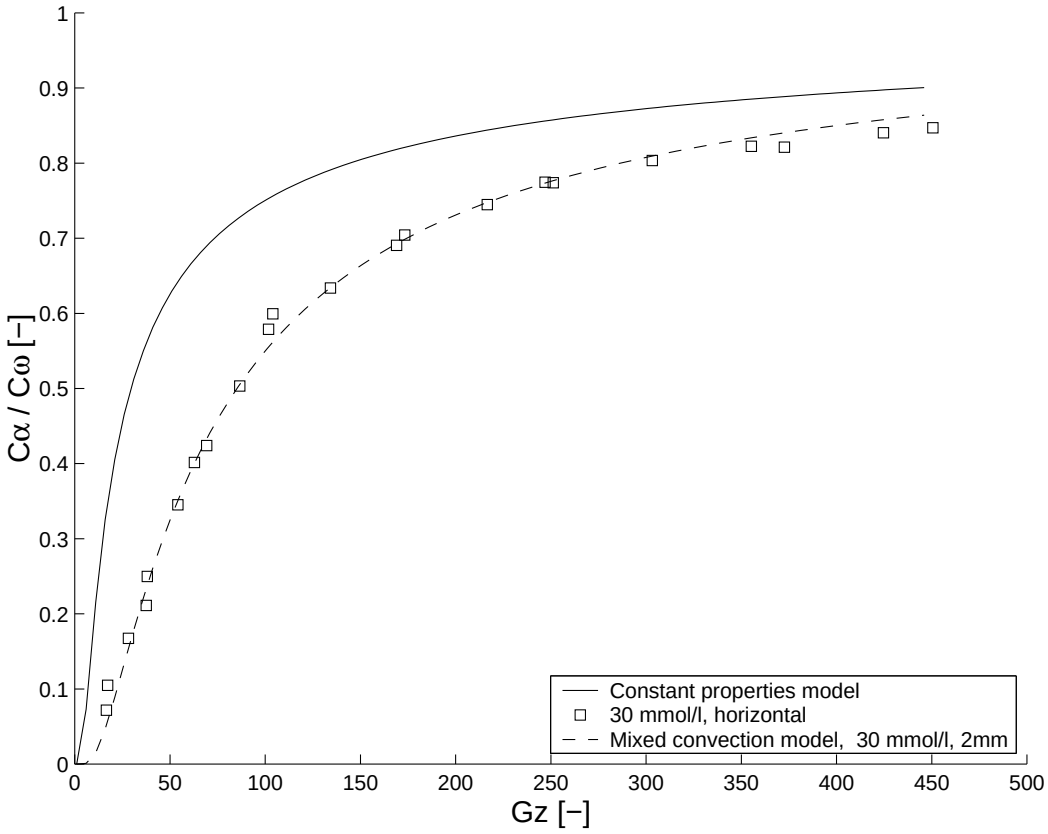


Figure 3.6: Comparison of experimental data with theoretical solutions for forced and mixed convection. Correlation used are due to Stephan (forced) and Shome and Jensen (mixed convection). Experimental data based on 2 mm i. d. tube and 30 mM $K_2Cr_2O_7$, Graetz-number computed with $D = 0.907 \cdot 10^{-9} m^2/s$.

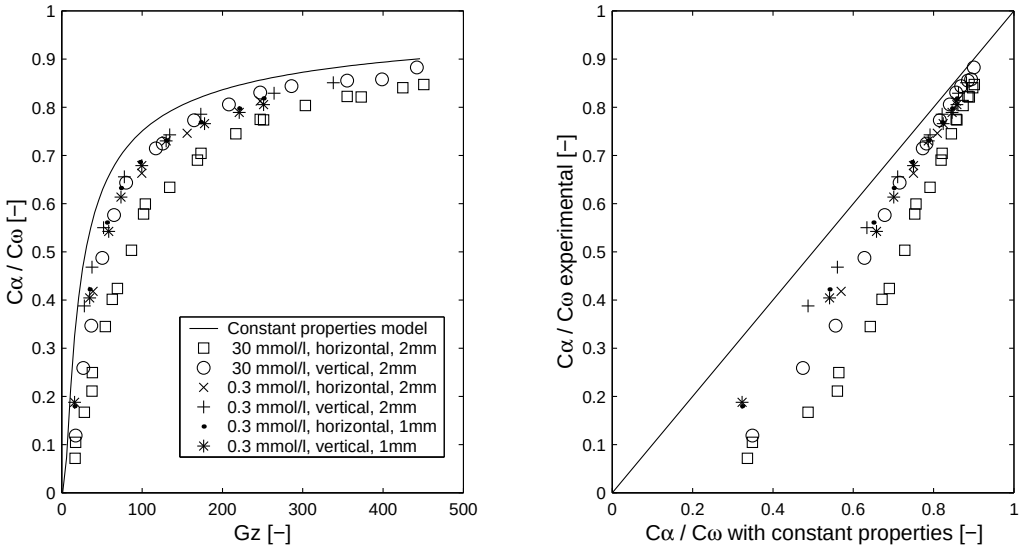


Figure 3.7: Results from modified experiment, based on $D = 0.907 \cdot 10^{-9} m^2/s$.

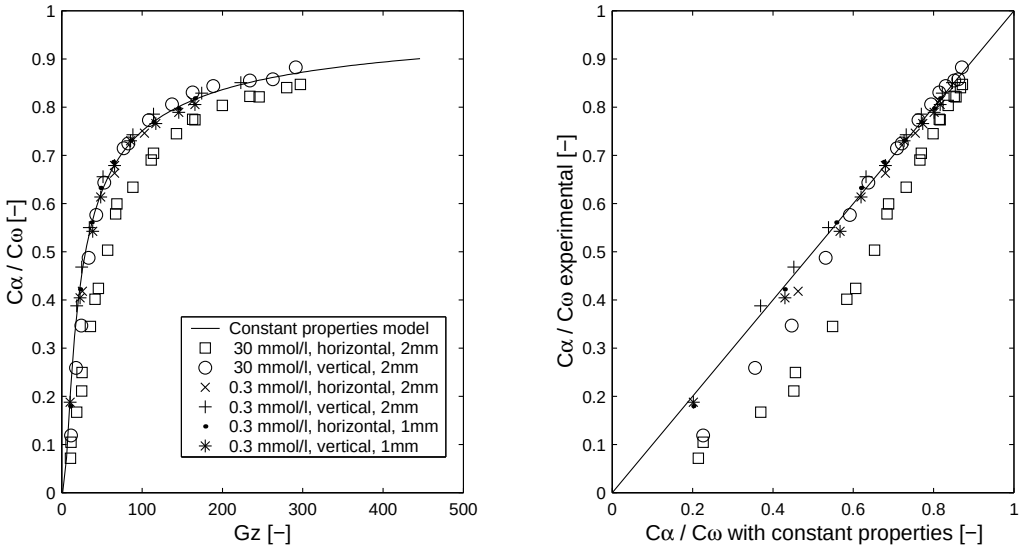


Figure 3.8: Results from modified experiment as before, but based on $D = 1.3756 \cdot 10^{-9} m^2/s$.

| | |
|---|---|
| 0.3 mmol/l $K_2Cr_2O_7$ in 1 M $H_2SO_4$ | $D = 1.01 \cdot 10^{-9} m^2/s$ |
| as above with 0.9 mmol/l $CuSO_4$ | $D = 0.99 \cdot 10^{-9} m^2/s$ |

Table 3.3: Diffusion coefficients fit to three experimental runs without natural convection.

Secondly, it is shown that even after eliminating natural convection, the experiments do not coincide with theory. Application of the other techniques further reduces the discrepancy until the results for the dilute solution in 1 mm capillaries and in 2 mm vertical capillaries approach each other. However, a significant deviation from the standard solution remains. The close proximity of the results for vertical and horizontal operation using the dilute dichromate system and a comparison with the Shome and Jensen solution for mixed convection shows that under these circumstances natural convection is insignificant. Apparently the remaining deviation has a different cause.

The picture changes significantly after fitting the diffusion coefficient to the three mentioned experimental runs (Fig. 3.8), resulting $D = 1.3756 \cdot 10^{-9} m^2/s$. The experimental data now coincide well with theory, with a standard deviation of 0.013.

This outcome again calls into doubt the diffusion coefficient reported by Gregory and Riddiford ($D = 0.907 \cdot 10^{-9} m^2/s$). This coefficient was measured at 30 mmol/l potassium dichromate, whereas we are now using a solution 100-fold more dilute. I therefore remeasured the coefficient by the Taylor-dispersion technique using both fresh dilute dichromate solution and solution to which copper sulphate was added. The results are summarised in Table 3.3 and show that dilution increases the diffusion coefficient, while the presence of small amounts of $Cu^{(II)}$ is without effect. The measured value of $D$, however, falls short of the value determined by fitting our data to theory.

At this point it is necessary to recall that $D$ is not a true Fickian diffusion coefficient but an effective or apparent coefficient. It lumps the diffusivities and interaction coefficients of all the chromate and dichromate species in the system into one parameter. In addition, it also lumps any local change in the physical properties of the system into the same parameter. Using effective diffusivities cuts through the often intractable problems encountered in more rigourous modelling at the expense of generality. Newman ([64], p. 304) points out that the effective diffusivity found for a chemically complex solution under one set of hydrodynamic and geometric conditions is not readily applicable to exactly the same solution under a different set of conditions. In the present case, the comparison of the copper dissolution and Taylor dispersion experiments shows that different effective diffusivities apply to radial transport with and without the chemical reaction at the wall. This

implicates the change in chemical composition and possibly also ionic interactions, such as migration and drag-effects which may result from the reaction, as the cause for the change in diffusivity.

Using the same analysis of the chemical composition as before, I found that the relative chemical composition of the dilute dichromate system does not change in the course of the reaction (Fig. 3.4. B). This is quite plausible, since the strong background concentration of protons is hardly altered by the reaction of the dilute $Cr^{(VI)}$ species. Therefore a shift to faster diffusing species can be ruled out.

### Ionic interaction

Ionic interactions can occur in two different ways in the present system. On the one hand, the ionic double-layer at the copper wall may create a local electrical potential which causes ionic migration. It is generally believed that such migration effects are suppressed by a high background electrolyte solution ([45], [64] p. 332). Gregory and Riddiford, however, observed an increase in effective diffusivity when they lowered the sulphuric acid concentration to 0.25 M [45] (see Table 3.2). They suggest ionic migration to be the cause, arguing that the strong background electrolyte concentration is depleted by the reaction near the wall, thus enabling migration. Whatever the merit of this argument may be, in the 100-fold dilute dichromate system the background electrolyte should be sufficient to reliably suppress migration.

Ionic-drag appears to be a more plausible cause for the spread of diffusion coefficients. In the present system, the reduction of every $Cr^{(VI)}$ ion at the copper wall consumes seven protons. The resulting considerable proton flux to the wall may therefore cause a drag-effect on anions such as the $Cr^{(VI)}$ species, thus enhancing mass transfer to the wall. On the other hand, the strong concentration of background electrolyte may again absorb the drag-effect, since sulphate and hydrogen sulphate anions are approximately 1600 times more concentrated in the solution than the $Cr^{(VI)}$ anions. Diffusing protons are therefore $\sim 1600$ times more likely to exert their drag on sulphate ions than on $Cr^{(VI)}$.

To settle this argument, we can evaluate the effective ionic transport equation, which is defined by Taylor and Krishna ([65], equ. 2.4.33) for a system containing $n$ electrolytes without convection as

$$N_i = -D_i^{\infty} \nabla C_i + \frac{t_i}{z_i} \sum_{j=1}^{n} z_j D_j^{\infty} \nabla C_j \tag{3.6}$$

using the following nomenclature:

| | |
|---|---|
| $N_i$ | molar flux of ionic species $i$ |
| $D_i^\infty$ | diffusion coefficient at infinite dilution |
| $C_i$ | local concentration of species $i$ |
| $t_i$ | transference number of species $i$ |
| $z_i$ | charge of species $i$ |

Using this definition, a simple numerical study was undertaken, in which a stagnant dichromate solution dissolved a flat copper wall. This one-dimensional problem was evaluated in Matlab using the above-mentioned method to impose the chemical equilibrium at every time-step. The process was run for 500 sec (simulated time) and then evaluated. The results showed a considerable influence of ionic drag in the concentrated dichromate system, whereas there is no noticeable effect in the dilute system. Comparing the overall consumption of $Cr^{(VI)}$, we find an increase of 10% for the concentrated and of 0.4% for the dilute system as compared to the simulation without ionic drag. On the basis of these findings, it appears unlikely that ionic drag causes the observed change in diffusivity and its cause remains unexplained.

Although it would be both interesting and challenging to resolve these questions, it is unnecessary for the aim and beyond the scope of this work to do so. It has been shown that the modified experimental system can be described very accurately with a simple effective diffusivity model and that the process of copper dissolution is transport-controlled. We are therefore now ready to proceed to the actual study of bubble-train flow on the basis of the modified copper dissolution method, which is the subject of the next section.

Before proceeding, however, it is worth discussing why mixed convection was not observed on previous occasions when using the copper dissolution method. In the case of Gregory's and Riddiford's study of the rotating disk, the data correlated closely with the extended Levich-correlation, which is theoretically well-founded. This implies that no mixed convection occurred. On reflection, this seems plausible. The rotating disk system is far less prone to mixed convection than laminar tube flow, because the region of the potentially highest density gradient close to the disk is simultaneously the region of strongest forced convection, which diminishes the density gradient. By contrast, in laminar flow, liquid at the wall stagnates, allowing the density gradient to build-up. Thus mixed convection probably did not occur in Gregory's and Riddiford's experiments.

In the case of other studies, the answer is less clear. For example, Zarraa et al. [47] studied mass transfer to a single sphere under gas sparging and Patil and Sharma [46] examined mass transfer in bubble columns with the aid of copper dissolution. In the absence of a reliable theoretical frame of reference, no deviation from theory could be detected and it thus remains unclear, whether mixed convection influenced their results or not. In such cases, the best approach may be to repeat the experiments at several degrees of dilution and to compare the results critically.

## 3.2 Experimental results and verification of numerical simulation

The experimental programme set out in Section 2.2.4 was executed and a set of simulations covering the identical range of parameters was performed. Besides the capillary length of 0.25 m, a viscosity of $\nu = 1.01 \cdot 10^{-6}\, m^2/s$ and a diffusion coefficient of $D = 1.3756 \cdot 10^{-9}\, m^2/s$ were used, resulting in Sc = 734.2. A film thickness of $\delta = 0.5\%$ was chosen in the simulations, which is a good estimate of the average experimental film thickness. The results are shown in Fig. 3.9 in terms of relative exit concentration over dimensionless plug length $\beta$.

The correlation between experiment and simulation is excellent. The standard deviation is $\sigma = 1.4\%$ and the errors are unsystematic.

By contrast, a comparison of the data reported by Horvath et al. [8] with simulations run with identical parameters[5] is disappointing (Fig. 3.10). It shows a systematic deviation from the numerical results towards lower rates of mass transfer. In view of the excellent agreement between my own experiments and simulations, I am inclined to seek the flaw in Horvath's data.

The potential source of error in the cited data arises from the enzyme-catalytic method used by the authors (see Section 2.2.1, p. 28). They base their analysis on the crucial assumption that the reaction rate in their capillary reactor is entirely transport-limited. The evidence they cite is based on previous work [66] in which single-phase mass transfer was studied. Since, as we shall see, mass transfer in bubble-train flow is faster by up to an order of magnitude than its single-phase counterpart, this evidence of transport limitation may no longer be sufficient. If the enzyme-catalysed reaction at the wall introduces an additional resistance to turnover, this would be most pronounced at the highest rates of mass transfer which occur in the shortest liquid plugs.

[5] However, a uniform film thickness of $\delta = 0.5\%$ was used in these simulations.

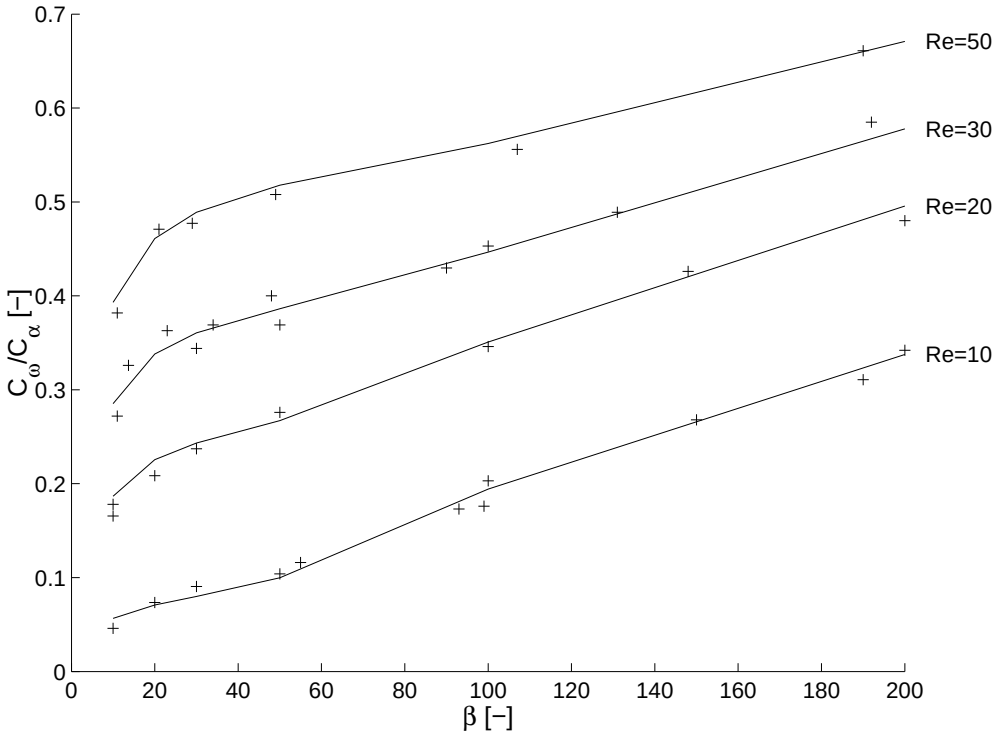


Figure 3.9: Comparison of experimental results from this study (marked with crosses) with data from the numerical simulation (connected lines).

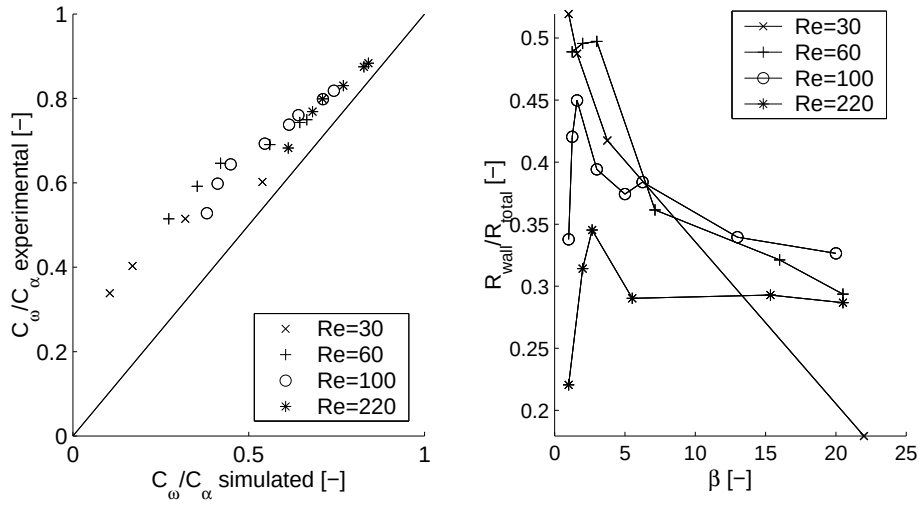


Figure 3.10: Comparison of experimental data reported by Horvath et al. [8] with simulations run with identical parameters. A plot of the experimental exit concentrations over the numerical results shows a systematic deviation between both (left). This deviation is analysed in terms of an additional transport coefficient at the wall over $\beta$ (right).

To test this hypothesis, I computed the wall resistance according to equ. 3.7 and plotted the ratio of the wall resistance to the overall resistance (Fig. 3.10).

$$R_{wall} = R_{Horvath} - R_{simulated} = \frac{1}{k_{L,Horvath}} - \frac{1}{k_{L,simulated}} \tag{3.7}$$

The result is ambiguous. The suspected increase of the wall resistance at lower $\beta$ is clearly visible at Re=30 and 60, whereas, contrary to the hypothesis, the wall resistance drops at Re=100 and 220. Thus the deviation between the cited data and my own remains unexplained.

Since no other reference data are available in the literature, I see no alternative to disregarding this discrepancy. On the evidence of the excellent agreement between the simulations and my own experiments, I consider the simulations verified by the experiments.

## 3.3 Sensitivity analysis and discussion

We will now turn to studying the sensitivity of mass transfer in bubble-train flow to the six governing dimensionless groups. As outlined in Section 2.3.6, the purpose of this analysis is to focus the simulation work on the essential parameters and to identify regions of the

parameter domain that require higher resolution. In addition, this analysis will reveal some interesting features of mass transfer in bubble-train flow.

As far as applicable, the data presented in this section are the result of the final simulation study which was launched after the sensitivity analysis. The original sensitivity study was based on more sparse data sets, which lend themselves less favourably to presentation.

### Reynolds and Schmidt-numbers

To study the sensitivity of mass transfer to the Schmidt-number, I ran a set of 12 simulations varying Re and Sc over four different values each[6], using a 1 mm × 25 cm capillary and assuming a film thickness of $\delta = 1\%$. As anticipated, a plot of the exit concentrations over Re resulted in four individual curves showing a strong sensitivity of mass transfer to Reynolds-number (Fig. 3.11). A plot over Re·Sc, however, resulted in a single curve, showing that mass transfer depends on the product of the Reynolds and Schmidt-numbers rather than on their individual values. This product is known as the Peclet-number which can be interpreted as the ratio of convective and diffusive transport rates. Thus in the present study Re and Sc can be replaced by Pe = Re·Sc without any loss of information.

The grouping of Re and Sc to Pe is frequently observed in heat and mass transfer problems. It is found in the solution of the Graetz-Nußelt problem as well, where Re and Sc are grouped together with $\gamma^{-1}$ to form the single governing variable, the Graetz-number Gz. In the case of bubble-train flow, however, no equivalent grouping of Re·Sc with a length variable could be detected.

The replacement of Re and Sc by Pe is significant for this study, since it reduces the parameter space by one dimension. In principle, this finding would also allow us to run all simulations at a single value of Re, and to vary Pe by changing Sc. In this case, the task of generating the hydrodynamic data would be reduced to computing a single data set. By the time I started the sensitivity analysis, though, the hydrodynamic data sets had already been computed.

The range of Pe required to cover all conceivable cases of mass transfer in bubble-train flow can be derived from the typical ranges of Re and Sc. With stable bubble-train flow limited to Re= $1 \ldots 1000$ and an estimated range of Sc= $400 \ldots 5000$, we find Pe= $400 \ldots 5 \cdot 10^6$. A sensitivity analysis of mass transfer over Pe shows, however, that the plug enhancement factor reaches a constant level above Pe$\approx 5 \cdot 10^5$ for all but the shortest plugs (Fig. 3.14). To stay on the safe side, I have limited the study to a range of Pe= $400 \ldots 8 \cdot 10^5$.

[6]Not all possible permutations of Re and Sc were simulated, thus only 12 rather than 16 runs.

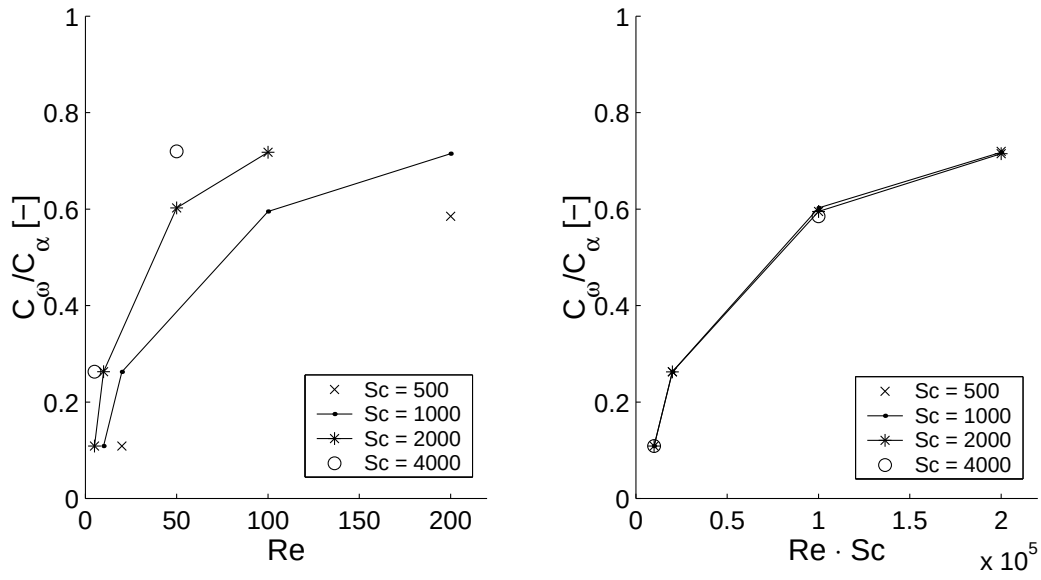


Figure 3.11: Relative exit concentrations from sample calculations for four different values each of Re and Sc. A plot over Re (left) shows four individual curves, whereas the curves coincide in a plot over Re·Sc. This shows that Re and Sc can be grouped together in describing mass transfer in bubble-train flow.

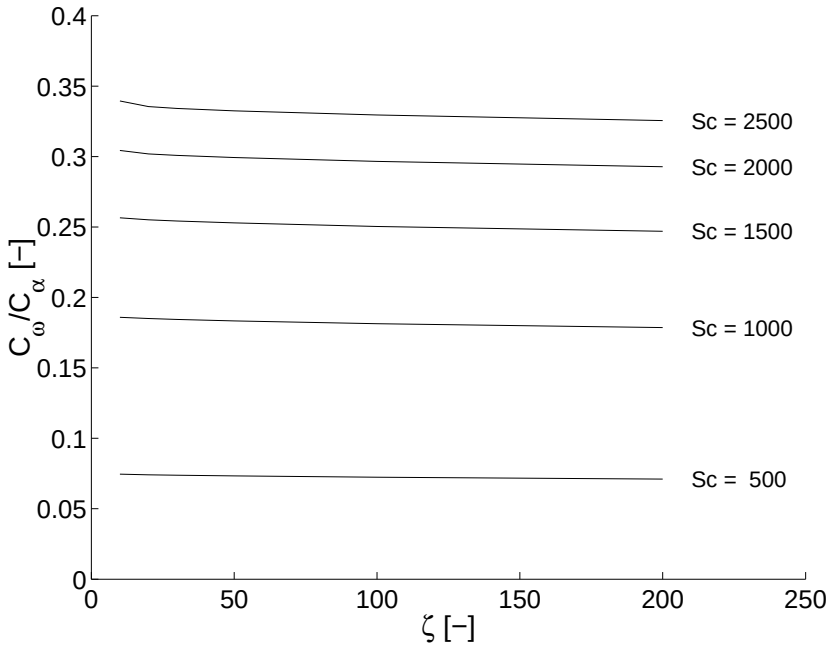


Figure 3.12: Numerically computed sensitivity plot of the exit concentration from a 1 mm × 25 cm capillary at Re = 20, Sc = 1000 and $\delta = 1\%$ over a range of dimensionless bubble lengths $\beta$. As anticipated by estimation, the exit concentration is insensitive to the bubble length.

### Bubble length $\zeta$

For two reasons the influence of the dimensionless bubble length $\zeta$ on the relative exit concentration from the capillary is weak. First of all, the bubble length clearly does not affect the hydrodynamics in the liquid plug, since the plugs are merely in contact with the bubble caps. Secondly, only a fraction of the overall liquid is located in the film between bubble and wall, as can be shown by estimating the fraction of liquid located in the film[7]:

$$\frac{V_{film}}{V_{plug}} = \frac{\zeta\delta}{\beta} \tag{3.8}$$

With $\delta \approx 0.01$ and $\beta > \zeta$ as a prudent technical requirement, less than one percent of the liquid is located in the film and its influence on overall mass transfer is correspondingly low.

To further support this view, a series of simulations spanning $\zeta = 10 \ldots 200$ and $\mathrm{Pe} = 10^4 \ldots 5 \cdot 10^4$ was run using a 1 mm × 25 cm capillary with $\delta = 1\%$, as before. The results are shown in Fig. 3.12 in terms of relative output concentration and confirm that $\zeta$ has a negligible influence on mass transfer. I have therefore chosen a single bubble length of $\zeta = 4$ for all further simulations and will exclude $\zeta$ from the correlation of Sh[8].

### Plug length $\beta$

Mass transfer is obviously sensitive to the plug lengths (Fig. 3.14). On the one hand, the effect of radial mixing near the bubble tips is all the stronger, the shorter the plugs. Thus the highest rates of mass transfer from the individual plug are achieved at the lower end of the $\beta$-scale. A plug enhancement factor as defined by equ. 1.45 of up to $\mathrm{E}_{plug} \approx 25$ was observed in this study at $\beta = 0.5$. This corresponds to a maximum $\mathrm{Sh}_{plug} \approx 200$.

On the other hand, the enhancement of mass transfer will diminish as the plugs lengthen and eventually mass transfer will approach the rates found in single phase flow. Surprisingly, this limit was not reached in the present study. With an exception at the lowest Peclet-numbers, the plug enhancement factor remained above 1 even for the longest plugs examined ($\beta = 600$). A linear extrapolation of $\mathrm{E}_{plug}$ at $\mathrm{Pe} > 2 \cdot 10^5$ suggests that E=1 is reached only at $\beta \approx 1100$.

[7]This method of estimation is justified by the absence of convective exchange between the film and the recirculation region.

[8]Despite its weak influence on the exit concentration from the capillary, the bubble length does influence $\mathrm{Sh}_{process}$, as was discussed in Section 1.4. In order to maximise process performance, it is therefore advisable to keep the bubbles short.

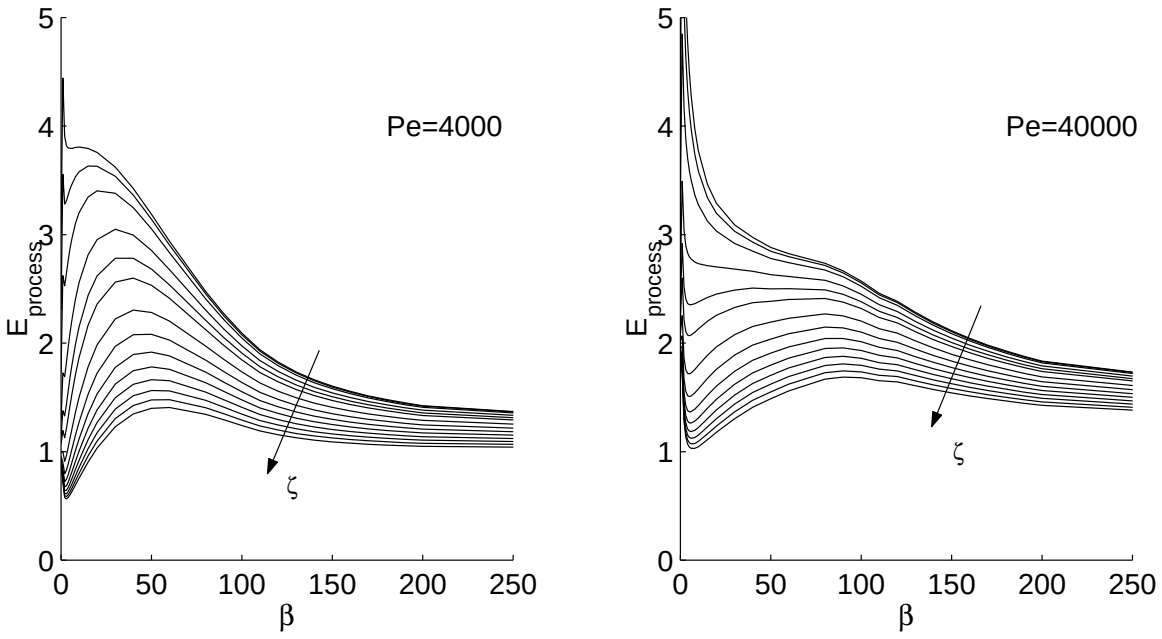


Figure 3.13: The process enhancement factor $E_{process}$ plotted over plug lengths $\beta$ for bubble lengths $\zeta \in \{2, 3, 5, 10, 15, 20, 30, \ldots, 100\}$. Data is plotted for Pe=4000 (left) and Pe=40000 (right).

As discussed in Section 1.4, a trade off between transport enhancement and loss of liquid-wall interface can lead to $E_{process}$ increasing only to a certain plug length and then falling again as the plug is further shortened. To examine this effect, the simulations were evaluated over a range of dimensionless bubble lengths from $\zeta = 2 \ldots 100$ (Fig. 3.13)[9].

The results are remarkable in several respects. First of all, the anticipated effect of the loss of wall area at shorter plug lengths is clearly visible. It does not, however, lead to a loss of process enhancement if the bubbles are kept short ($\zeta = 2$). Secondly, longer bubbles do lead to a loss of process enhancement, but $E_{process}$ only drops below unity at low Peclet-numbers, whereas it remains larger than unity under all circumstances at higher values of Pe. The risk of loosing process efficiency by using bubble-train flow is therefore very low. Thirdly, although $E_{process}$ may drop as the plugs are shortened, it passes through a minimum and then rises sharply again as the plugs are further shortened. Apparently, the intense mixing in very short plugs can overcompensate the loss of wall area.

[9]This examination does not contradict the earlier finding that $\zeta$ may be omitted from parameter domain of the simulations. Instead, the influence of $\zeta$ on $Sh_{process}$ and $E_{process}$ is introduced after the simulation by multiplication with $(1 - \epsilon)$. See Section 1.4 for further discussion.

In conclusion, the final simulations will have to span the largest possible range of plug lengths. On the available hardware, this translates into a range of $\beta \leq 600$. At the lower end of the scale, the range of $\beta$ requires a fine resolution, whereas it is sufficient to sample mass transfer sparsely for very long plugs. Since the computational effort and memory requirement increase linearly with $\beta$, this analysis is very instrumental in keeping down the computational expense.

### Capillary length $\gamma$

A study of the influence of the capillary length on mass transfer reveals that the log-averaged $\mathrm{Sh}_{plug}$ reaches a constant value after a certain entry length. In order to quantify this length, it was defined as the axial position $\gamma_e$ at which $\mathrm{Sh}_{plug}$ has approached its value at $\gamma = 1000$ to within 1%. Based on this definition, the entry lengths were extracted from the data set for $\mathrm{Sh}_{plug}$ (Fig. 3.15). The plot reveals a dependence of $\gamma_e$ on $\beta$, rising from $\sim 20$ for short plugs to $\sim 400$ for long ones, while remaining virtually unchanged over Pe. The only departure from this rule can be observed at low Pe and long plugs. Here the entry length rises sharply to $\sim 800$. This could be a result of the particularly sluggish evolution of a steady concentration profile in the slowly moving long plugs, but I have investigated this question no further. In order to capture the entry-length behaviour, it appears advisable to run the simulations over a range of $\gamma = 0 \ldots 1000$ for all combinations of Pe and $\beta$.

### Film thickness $\delta$

The thickness of the liquid film between bubble and wall appears to have very little influence on mass transfer as long as it is thinner than $\sim 1\%$ of the capillary diameter. This was shown by running simulations $\mathrm{Sh}_{plug}$ at various values of Pe and at a fixed plug length of $\beta = 5$ (Fig. 3.16). For $\delta > 1\%$, $\mathrm{Sh}_{plug}$ decreases with increasing film thickness.

There are two possible causes of this effect - one natural and one artificial. $\delta$ is a measure for the thickness of the diffusional layer that separates the recirculation region from the wall. A thinner layer means a steeper concentration gradient and therefore a higher flux. The sensitivity study suggests that the additional resistance to mass transfer introduced by the thickening film is negligible up to $\delta = 1\%$. It is unclear, however, whether the deviation of $\mathrm{Sh}_{plug}$ at $\delta > 1\%$ is solely attributable to the additional film thickness, or whether the heuristic upstream boundary condition where the film enters the domain begins to affect the results.

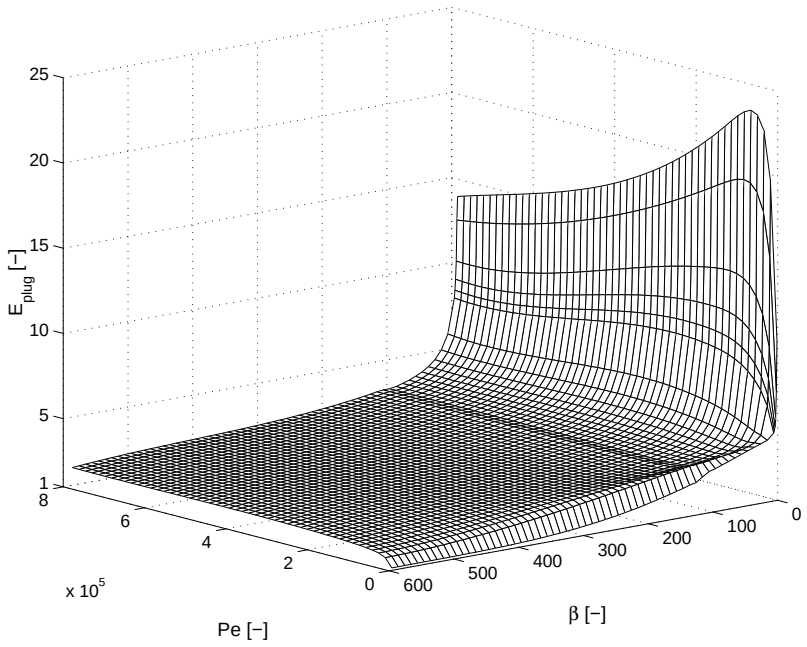


Figure 3.14: The sensitivity of mass transfer to the length of the liquid plugs in terms of the plug enhancement factor over Pe and $\beta$. The numerical data are based on a dimensionless tube length of $10^3$ and has been interpolated by cubic splines to achieve a finer grid.

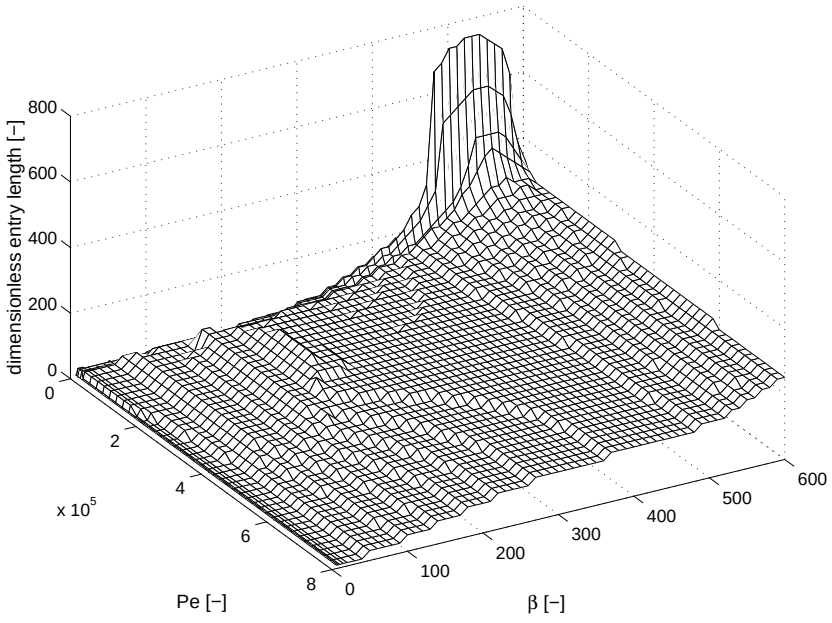


Figure 3.15: A plot of the entry length of mass transfer over Pe and $\beta$. The entry length is defined here as the axial position $\gamma_e$ in the capillary at which $\mathrm{Sh}_{plug}$ has approached the value at $\beta = 1000$ to within 1%. As above, the data have been interpolated by cubic splines.

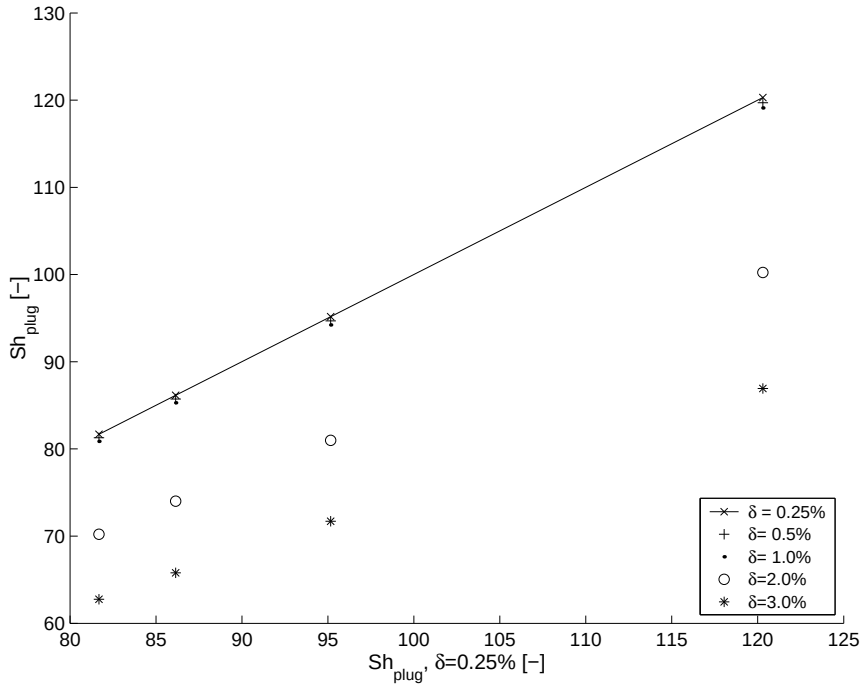


Figure 3.16: A plot of $\mathrm{Sh}_{plug}$ for a range of film thicknesses $\delta$ over the corresponding values at $\delta = 0.25$. The data were obtained numerically over a range of Peclet-numbers and for $\beta = 5$.

A series of tests using other upstream boundary conditions showed some sensitivity of $\mathrm{Sh}_{plug}$ at $\delta > 1\%$, but only partially affected the deviation from the thin-film results. More importantly, it remains unclear which method of simulation produces accurate results, since no experimental reference data for varying film thicknesses are available. On the other hand, it was shown in Section 2.3.2 that under most technically relevant circumstances the film thickness remains below 1%. The considerable effort involved in resolving these issues with thicker films therefore does not seem warranted, and I have chosen to limit the scope of this work to $\delta < 1\%$. Under this limitation, we can neglect $\delta$ as a parameter for mass transfer in bubble-train flow.

In summary, the parameter domain of the problem can be simplified by omitting $\zeta$ and $\delta$ and by grouping Re and Sc to Pe. The problem is thus reduced to examining $\mathrm{Sh} = f(Pe, \beta, \gamma)$. The final numerical simulation will cover the following parameter domain:

$\mathrm{Pe} = 1600 \ldots 800000$

$\beta = 0.5 \ldots 600$ with higher resolution at the lower end of the scale

$\gamma = 0 \ldots 1000$

## 3.4 Results of the numerical simulation

The presentation of the four-dimensional data set obtained in the final numerical simulation requires some preponderance. The objective is to convey all the essential features of the data in a compact presentation and in a manner facilitating its use in engineering.

The attempt to present the entire data set in a nomography failed, since no valid factorisation of Sh of the form

$$\mathrm{Sh} = f_1(A,\, B) \cdot f_2(A,\, C)$$

could be found, where A, B and C stand for any combination of the three governing dimensionless groups. The only alternative is to present several two-dimensional cuts through the data set. The sensitivity analysis showed a strong dependence of Sh on Pe and $\beta$, while the dependence on $\gamma$ is comparatively weak and limited to an entry length of the capillary. This suggests plotting Sh over $\beta$ with Pe as the additional parameter or vice versa, while keeping $\zeta$ constant. I have chosen the former, which follows the example of Horvath et al. [8] and facilitates the comparison with their results.

The results are presented in Fig. 3.17 and 3.18 for dimensionless capillary lengths of $\zeta$ = 50, 100, 200 and 1000 and for Peclet-numbers ranging from 1600 to 800000. The single-phase Sherwood-number computed with equ. 1.15 is included for reference. It was computed with the absolute velocity of the two-phase flow (i. e. plug velocity) and is therefore the upper limit of the actually comparable single-phase Sherwood-number.

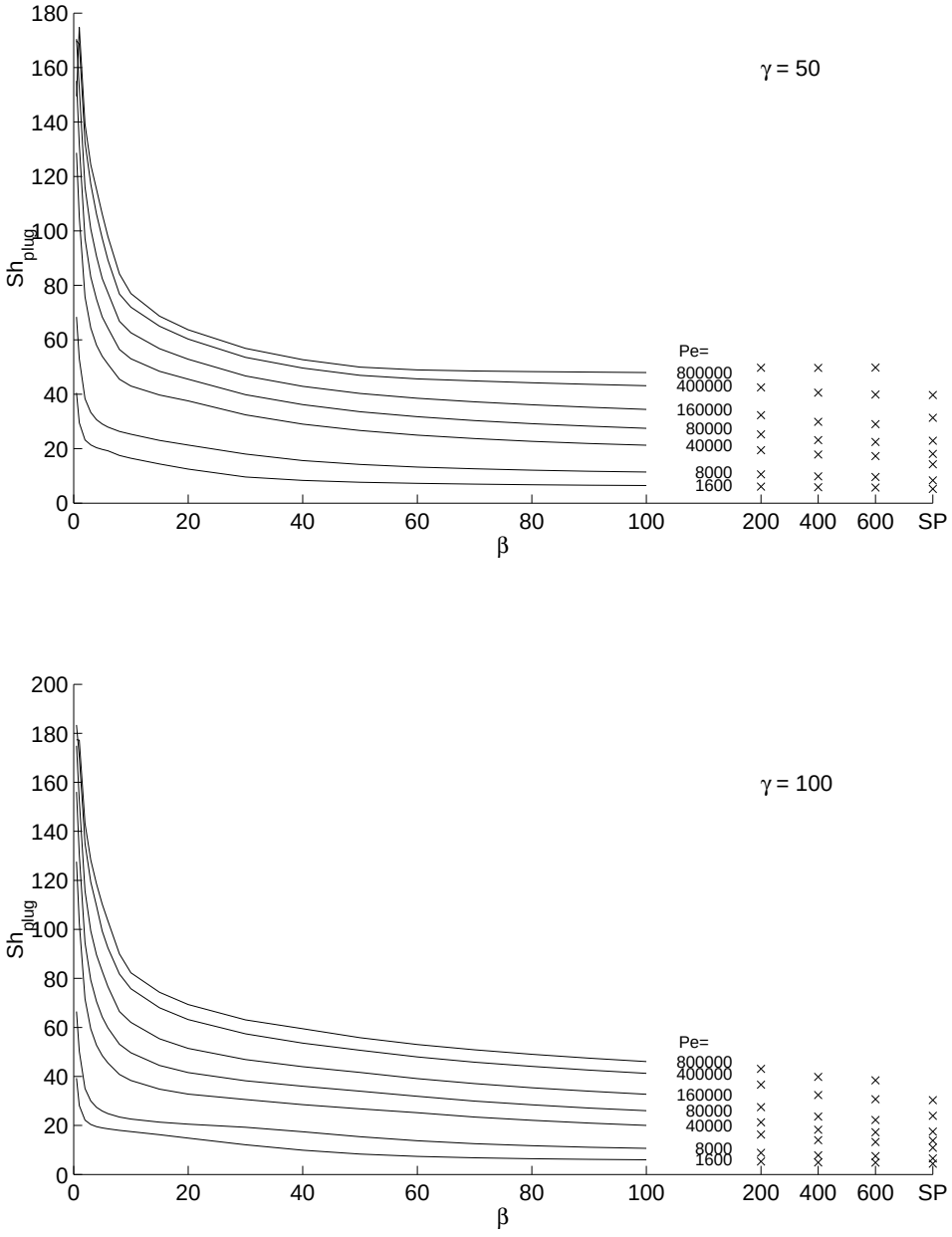


Figure 3.17: Summary of the numerical data for capillaries with a dimensionless length of $\zeta = 50$ (top) and $\zeta = 100$ (bottom) over a range of Pe. The single phase Sherwood-numbers are included for reference and are marked with *SP*.

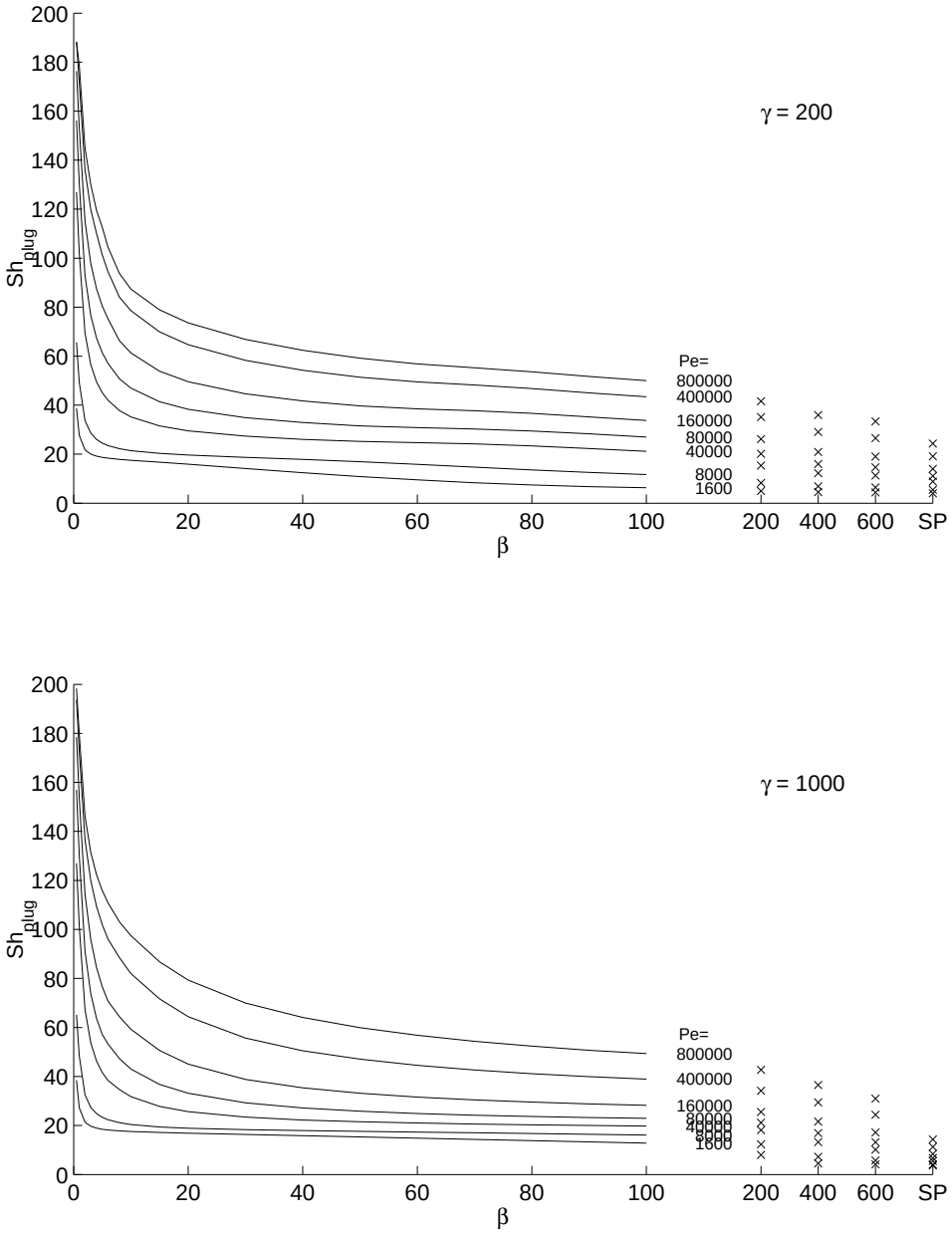


Figure 3.18: Summary of the numerical data as in Fig. 3.18, but for capillaries with a dimensionless length of $\zeta = 200$ (top) and $\zeta = 1000$ (bottom).

## 3.5 The mechanism of flux enhancement

Besides the integral data for mass transfer presented in the previous section, the numerical simulation also offers a unique opportunity to study the evolving local concentration profiles during mass transfer in bubble-train flow. Apart from satisfying scientific curiosity, this analysis will elucidate the mechanism of flux enhancement and provide the basis for a mechanistic model, which will be explored in the following section.

In Fig. 3.19, the evolution of the local concentration distribution in a liquid plug is plotted[10]. As the plug enters the capillary (A), the first depletion appears at the wall. When the rear bubble enters the capillary as well (B), the concentration boundary layer is sheered off by the bubble and deflected towards the centre. A cone of depleted liquid then flows down the centre of the capillary (C-E). As it reaches the forward bubble (F-G), it is deflected towards the wall. The fully established concentration distribution (H) is characterised by depletion at the wall and along the centre of the capillary, while a torus-shaped region along the line of zero relative velocity is left comparatively untouched.

These findings not only confirm the existence of the characteristic regions of flow identified in Section 1.3, but also show by which mechanism bubble-train flow enhances mass transfer. As Fig. 3.19 shows, the region of maximum concentration is located not at the centre of the capillary as in the Graetz-Nußelt problem but in a torus-shaped region and therefore much closer to the wall. The result is a steeper concentration gradient near the wall which leads to increased radial diffusion.

To illustrate this effect in more detail, the normalised radial concentration profiles in bubble-train flow and in the single-phase problem are compared in Fig. 3.20. The single-phase profiles were calculated with the approximate solution to the Graetz-Nußelt problem presented by Skelland [13, p. 160 ff.], while the bubble-train concentration profile was taken from the numerical simulation at a position half-way between two bubbles. Both sets of data were sampled at $\gamma = 50$, 100, 150 and 200[11].

The single-phase profiles show the expected gradual decay of the concentration gradient. By contrast, the normalised concentration gradient in bubble-train flow remains constant once it has been established and is steeper than its single-phase counterpart at the same

[10]The following discussion of Fig. 3.19 assumes mass transfer from the liquid to the wall, although the plots are naturally valid for the reverse case as well. Furthermore, I shall assume a frame of reference moving with the bubbles.

[11]The data were computed using the exemplary values of Re=10 and Sc=1000; the findings hold for other levels of $\beta$, Re and Sc as well.

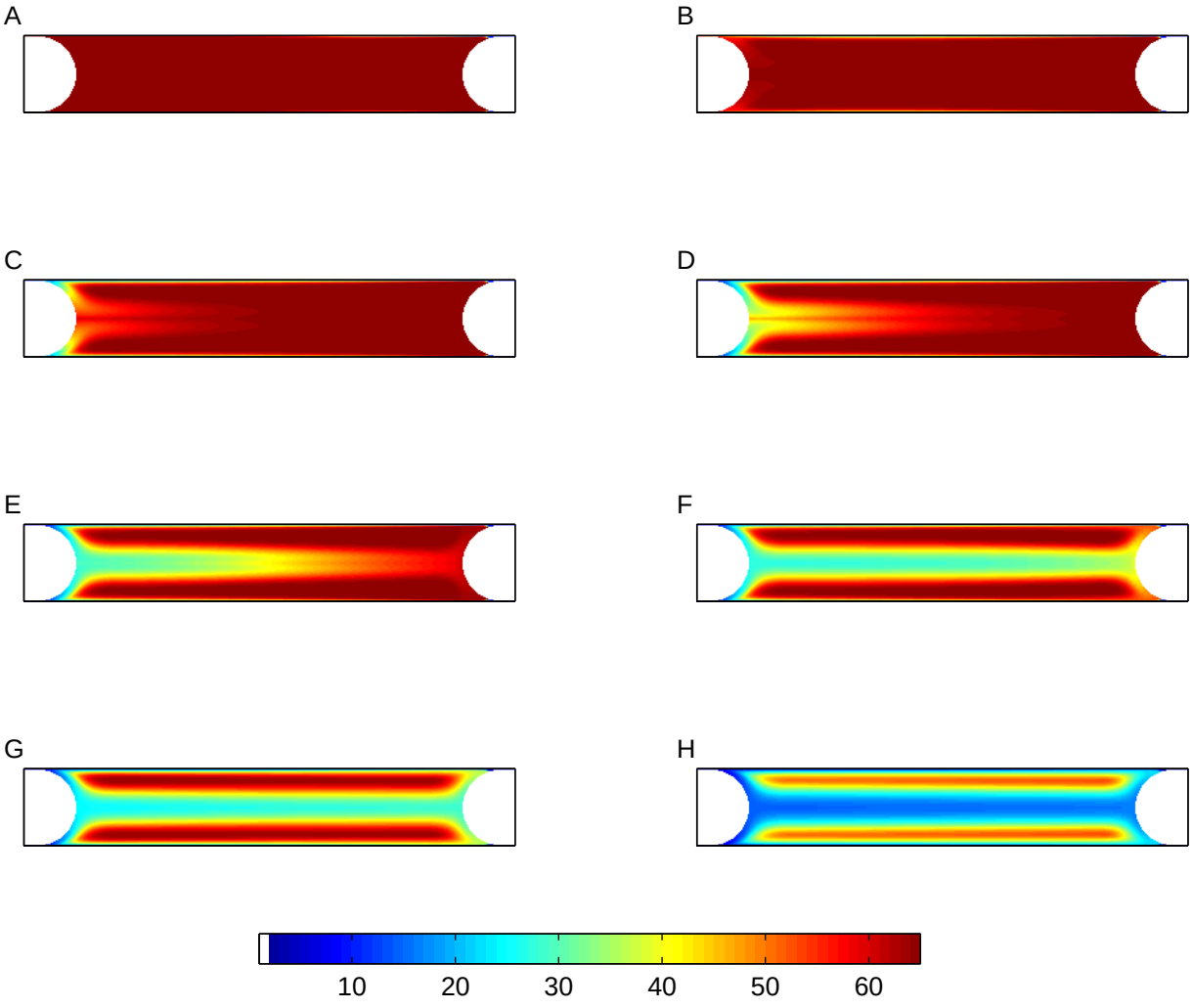


Figure 3.19: The evolution of the concentration distribution in a liquid plug as the plug enters the capillary.

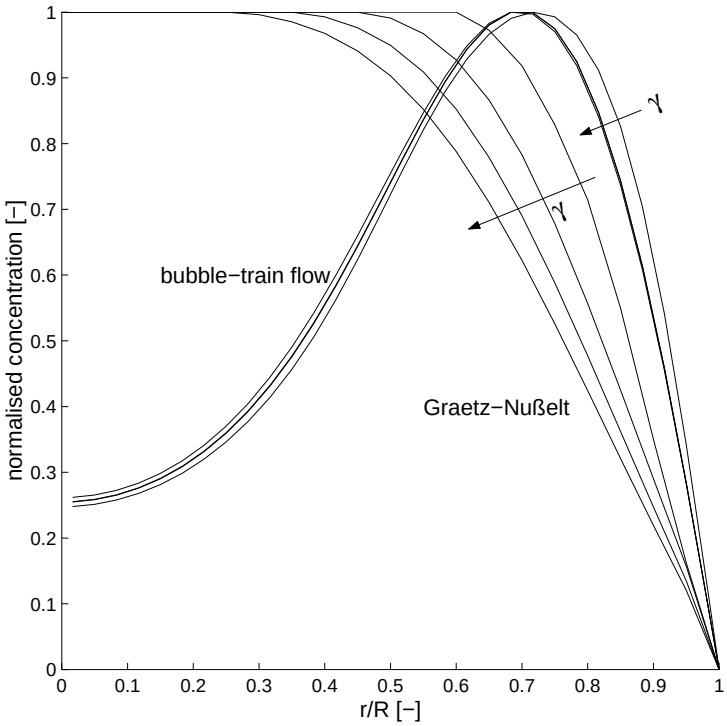


Figure 3.20: Comparison of the radial concentration profiles in laminar single-phase and bubble-train flow. The profiles are plotted for $\gamma = 50$, 100, 150 and 200. The concentration profile in bubble-train flow was computed with $\beta = 20$ and was extracted from a position half-way between the bubbles. All concentrations were normalised.

axial position. It is this steeper concentration gradient near the wall that causes the enhancement to mass transfer observed in bubble-train flow.

## 3.6 Correlating the data

We now turn to the final task of developing a mathematical correlation for the obtained data set. As discussed in Section 2.1.1, there is merit in seeking to develop a mechanistic model, since it promises greater reliability outside the data set to which its parameters were fitted. I therefore attempted this approach first. However, the attempt was abortive and I will therefore merely sketch the method used.

The typical approach to creating a mechanistic model for mass transfer problems is to subdivide the physical system into characteristic regions and represent each of them by a simple model for flow and mass transfer. This results in a system of partial differential equations (PDEs) with at least one PDE for every characteristic region. The next step is to

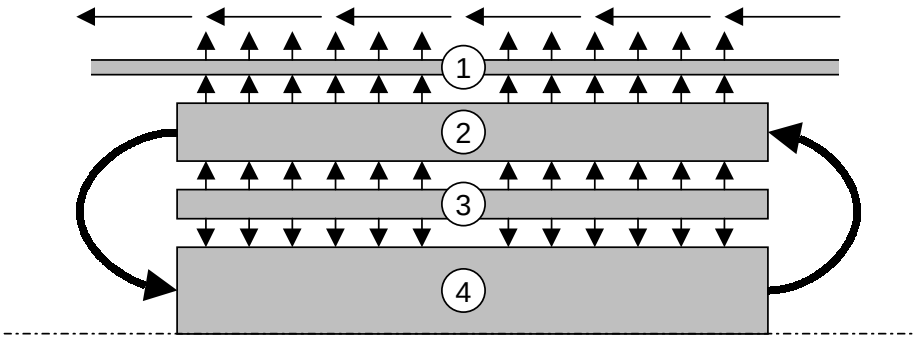


Figure 3.21: To create a mechanistic model of mass transfer in bubble-train flow, the flow pattern in a liquid plug can be segmented into four distinctive regions.

solve the system of PDEs and invoke the initial and boundary conditions to obtain the raw model. Finally, the remaining free parameters of the model are fitted by suitable means to a set of experimentally or numerically obtained data describing the actual physical system.

As already discussed in Section 2.1.1, the critical step is solving the PDEs. Only comparatively simple PDEs are readily analytically solvable and even then the solution is often algebraically too unwieldy to be of practical use. The crux in mechanistic modelling is therefore to find a representation of the physical system that leads to a solvable system of PDEs while still capturing the essential behaviour of the physical system. Clearly, this will not always succeed, as in the present case.

Based on the analysis of Fig. 3.19 in the previous section, four distinctive regions of flow (Fig. 3.21) can be distinguished: a film at the wall (1), a bulk region flowing towards the rear bubble (2) and one flowing towards the forward bubble (4), while regions (2) and (4) are separated by a comparatively stagnant area (3). The boundary lines between the regions can be formulated in terms of the characteristic radii $r_0$ and $r_1$ defined in Section 1.3.

The next step is to create a model for each region that is sufficiently simple to allow the integration of the resulting system of PDEs, yet still captures the true behaviour of the system. A frequently used approach is to assume each region to be ideally mixed and then to model the exchange between the regions with mass transfer coefficients, which are determined by fitting them to a data set. Taking this approach, a simplified version of the model shown in Fig. 3.21 was integrated successfully. However, the resulting correlation could not be fitted to the data set from the numerical simulation without a very large and systematic residual error. Clearly, the mechanistic approach failed to capture the physical system correctly.

This failure can be traced to the assumption of ideal mixing within each region. In turbulent flows, the assumption of an ideally mixed bulk is reasonable. For laminar flows with their distinctive concentration and velocity profiles, however, this assumption is a crude oversimplification. To capture the behaviour of the laminar system successfully, more intricate models are required for the concentration and velocity profiles within each region.

At this point, it may seem called for to explore this route to modelling further. However, I have decided not to do so for several reasons. First of all, even the simple model employed above resulted in a correlation that is mathematically cumbersome to use. A more elaborate model is likely to lead to an even less facile result. Secondly and more critically, this study has shown that bubble-train flow enhances mass transfer appreciably even in very long plugs with dimensionless lengths in the order of $\beta > 1000$. In such cases, the axial change in concentration within the plug can no longer be neglected and must be included in the mechanistic model. This introduces an additional coordinate to the PDEs and renders them far more difficult to solve. Even if this problem could be overcome, the model would suffer a further shortcoming, in that it offers no means to model the gradual entry into and exit from the capillary. For short plugs, this may not be critical, since the entry and exit take a short space of time. For long plugs, however, the entry and exit of the plug would make-up a sizable proportion of the overall process and must be considered. In view of these unresolved issues, it seems justified to abandon the mechanistic approach and take an empirical route to modelling.

Constructing an empirical model basically involves finding an equation with as few free parameters as possible that can be fitted to the data set and then renders it with as small an error as possible. Although the literature on heat and mass transfer abounds with such models, there is to date no systematic method to derive their basic structure. In the absence of a basic equation obtained by mechanistic analysis, finding a suitable equation is a task of trial and error.

A qualitative analysis of the numerical data revealed some similarity between $\mathrm{Sh}_{plug}$ over Pe and $\beta$ and a hyperbolic tangent curve. I have therefore chosen this function as a basic building block to construct the equation[12].

The next step was to construct a model that renders the steady values of $\mathrm{Sh}_{plug}$ after the entry effects have subsided. I found that $\mathrm{Sh}_{plug}$ can be approximated by the product of two subfunctions, representing the effects of Pe and $\beta$ respectively. The seven free parameters

[12]Here I find myself in the company of Stephan [11, p. 363], who used the hyperbolic tangent to construct his solution of the Graetz-Nußelt problem (see equ. 1.15).

of this first model were fitted globally to the subset of numerical results for $\gamma = 600$ with the aid of the Gauss-Newton algorithm implemented in *Matlab*.

The model was then extended by means of a third subfunction to capture the entry effects, which depend in sign and magnitude on both Pe and $\beta$ and subside as a decay-function of $\gamma$. This third subfunction introduces a further five free parameters to the model. The entire set of twelve parameters were fitted globally to the numerical data set by the same method as before.

The resulting correlation renders the numerical data very satisfactorily, with a marked exception at the bottom end of the $\beta$ and $\gamma$ ranges. I therefore decided to limit the scope of the correlation to $\beta \geq 1$ and $\gamma \geq 30$, which in practise is an insignificant limitation. After finally refitting the coefficients to the thus reduced data set, the result is as follows:

$$\mathrm{Sh}_{plug} = a_1 \cdot \tanh(a_2 \mathrm{Pe}^{a_3} + a_4) \cdot \tanh(a_5 \beta^{-a_6} + a_7) \cdot \left(1 - (a_8 \mathrm{Pe} - a_9 \beta^{a_{10}} - a_{11}) \cdot e^{-a_{12}\gamma}\right) \quad (3.9)$$

with the following coefficients:

$$\begin{aligned}
a_1 &= 9.6699 \cdot 10^{3} & a_7 &= 2.3378 \cdot 10^{-3} \\
a_2 &= 6.1743 \cdot 10^{-4} & a_8 &= 9.0380 \cdot 10^{-7} \\
a_3 &= 5.9852 \cdot 10^{-1} & a_9 &= 6.5869 \cdot 10^{-2} \\
a_4 &= 1.1468 \cdot 10^{-1} & a_{10} &= 4.6481 \cdot 10^{-1} \\
a_5 &= 1.8897 \cdot 10^{-2} & a_{11} &= 1.3620 \cdot 10^{-2} \\
a_6 &= 4.6692 \cdot 10^{-1} & a_{12} &= 2.8882 \cdot 10^{-2}
\end{aligned}$$

The correlation has been fitted to data in the range of $\mathrm{Pe} = 1.6 \cdot 10^3 \ldots 4 \cdot 10^5$, $\beta = 1 \ldots 600$ and $\gamma = 30 \ldots 1000$, but should be valid for larger values of $\beta$ and $\gamma$ as well. Within this range, it reproduces the results of the numerical simulation with an arithmetic mean error of $\pm 10\%$ and a maximum error of generally no more than $\pm 20\%$ (Fig. 3.22).

Equ. 3.9 is applicable to a single liquid plug or a complete flow with uniform plug lengths. As I remarked in Section 1.4, however, bubble-train flow under technical conditions will typically encompass a spread of plug and bubble sizes. It is therefore useful to extend equ. 3.9 accordingly. Since it was shown in Sections 1.4 and 3.3 that the rate of mass transfer from the liquid plug is independent of the bubble length, the extension of equ. 3.9 merely involves taking account of a spread of plug lengths.

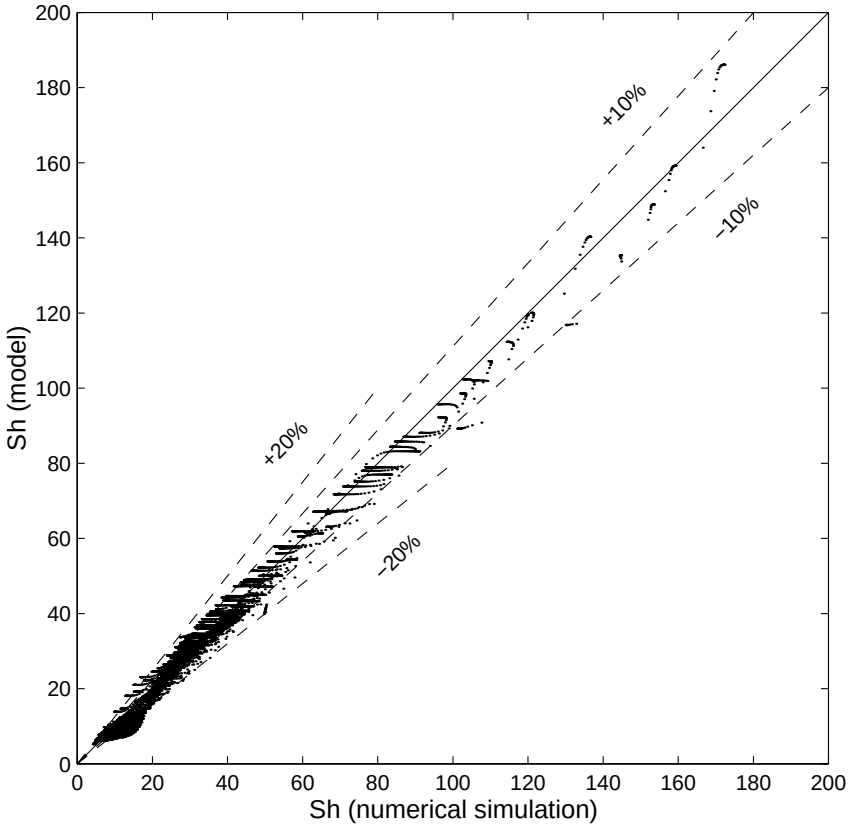


Figure 3.22: Plot of Sherwood as predicted by the correlation (eq. 3.9) over Sh computed in the numerical simulation. The model generally predicts the numeric results to within ±10%, but displays an increased error of up to ±20% at the lower end of the scale.

Typically, a distribution of plug lengths is described by means of a distribution density function $E_{(\beta)}$, where $E_{(\beta)}d\beta$ is the volume-fraction of all plugs flowing through the system that have dimensionless length between $\beta$ and $\beta + d\beta$ [13]. Then the cup-mixing exit concentration is

$$\overline{C} = \int_0^\infty C_{(\beta)} E_{(\beta)}\, d\beta \tag{3.10}$$

By introducing equ. 3.10 into equ. 1.41 we find the Sherwood-number for stochastic bubble-train flow:

$$\overline{\mathrm{Sh}} = \frac{\mathrm{Gz}_{tot}}{4} \ln\left(\frac{C_\alpha}{\overline{C_\omega}}\right) = \frac{\mathrm{Gz}_{tot}}{4} \ln\left(\frac{C_\alpha}{\int_0^\infty C_{(\beta)} E_{(\beta)}\, d\beta}\right) \tag{3.11}$$

We may express $C_{(\beta)}$ in terms of $\mathrm{Sh}_{plug}$ as defined by equ. 3.9 by solving equ. 1.41:

$$C_{(\beta)} = C_\alpha \exp\left(-\frac{4\mathrm{Sh}_{(\beta)}}{\mathrm{Gz}_{tot}}\right) \tag{3.12}$$

By inserting equ. 3.12 into equ. 3.11, we finally obtain the Sherwood number for stochastic bubble-train flow, which can be evaluated numerically:

$$\overline{Sh} = -\frac{\mathrm{Gz}_{tot}}{4} \ln\left(\int_0^\infty \exp\left(-\frac{4\mathrm{Sh}_{plug}}{\mathrm{Gz}_{tot}}\right) E_{(\beta)}\, d\beta\right) \tag{3.13}$$

[13] The exact shape of the distribution density function depends the method of creating the two-phase flow. For example, it may adopt a Gauss-distribution, in which case $E_{(\beta)} = \frac{1}{\sigma\sqrt{2\pi}} \exp\left(\frac{-(\beta-\overline{\beta})^2}{2\sigma^2}\right)$, where $\sigma^2$ is the variance and $\overline{\beta}$ is the average dimensionless plug length.

# 4

# Conclusions

In this work, radial mass transfer in bubble-train flow through capillary tubes has been studied experimentally and numerically over a wide range of the governing variables, with three essential results.

First of all, the understanding of the bubble-train flow regime has been extended. The enhanced rate of mass transfer as compared to single phase laminar flow has been traced to the steeper concentration gradient at the capillary wall that is caused by the distinctive liquid flow pattern in bubble-train flow. The degree of enhancement has been found to depend strongly on the liquid Peclet-number and on the length of the liquid plugs, displaying the sharpest increase for very short plugs while remaining distinctly noticeable even for the longest plugs examined. In contrast to single-phase laminar flow, entry effects in bubble-train flow are brief and a steady Sherwood-number is rapidly reached.

Secondly, a mathematical correlation has been developed that predicts the rate of radial mass transfer in terms of a plug-Sherwood-number with reasonable accuracy.

Thirdly, a hitherto unnoticed source of error in the copper dissolution method of measuring solid-liquid mass transfer has been identified. The error has been traced to the distortion of the flow pattern by natural convection and an improved experimental method has been suggested to avoid this source of error.

From an engineering point of view, bubble-train flow is an attractive means to enhance radial mass transfer in small ducts. It has been shown that process performance is enhanced over a wide range of operating conditions. As Horvath et al. [8] point out, "the introduction of gas bubbles into the liquid stream does not create technical difficulties which would not be well compensated by the significant increase in radial transport". From my own experience, I can confirm this view. I therefore hope that this work will contribute to making bubble-train flow a standard tool for mass transfer enhancement.

# References


[1] L. T. Skeggs Jr. An automatic method for colorimetric analysis. *Journal of Clinical Pathology*, 28:311–322, 1957.

[2] J. Prothero and A. C. Burton. The physics of blood-flow in capillaries - i. the nature of the motion. *Biophysical Journal*, 1:565–575, 1961.

[3] H. A. Johnson and A. H. Abou-Sabe. Heat transfer and pressure drop for turbulent flow of air-water mixtures in a horizontal pipe. *Transactions of the American Society of Mechanical Engineers*, 74:977–987, 1952.

[4] H. A. Johnson. Heat transfer and pressure drop for viscous-turbulent flow of oil-air mixtures in a horizontal pipe. *Transactions of the American Society of Mechanical Engineers*, 77:1257–1264, 1955.

[5] D. R. Oliver and S. J. Wright. Pressure drop and heat transfer in gas-liquid slug flow in horizontal tubes. *British Chemical Engineering*, 9:590–596, 1964.

[6] D. R. Oliver and A. Young-Hoon. Two-phase non-newtonian flow - ii. heat transfer. *Transactions of the Institution of Chemical Engineers*, 46:116–122, 1968.

[7] K. A. Triplett, S. M. Ghiaasiaan, S. I. Abdel-Khalik, and D. L. Sadowski. Gas-liquid two-phase flow in microchannels, part i: two-phase flow patterns. *International Journal of Multiphase Flow*, 25:377–394, 1999.

[8] C. Horvath, B. A. Solomon, and J-M. Engasser. Measurement of radial transport in slug flow using enzyme tubes. *Industrial and Engineering Chemistry Fundamentals*, 12(4):431–439, 1973.

[9] J. L. Duda and J. S. Vrentas. Steady flow in the region of closed streamlines in a cylindrical cavity. *Journal of Fluid Mechanics*, 45:247–260, 1971.

[10] J. L. Duda and J. S. Vrentas. Heat transfer in a cylindrical cavity. *Journal of Fluid Mechanics*, 45:261–279, 1971.

[11] H. D. Baehr and K. Stephan. *Wärme und Stoffübergang*. Springer, 1998.

[12] R. B. Bird, W. E. Stewart, and E. N. Lightfoot. *Transport Phenomena*. Wiley, 1960.

[13] A. H. P. Skelland. *Diffusional Mass Transfer*. Wiley, 1974.

[14] L. Graetz. Über die Wärmeleitfähigkeit von Flüssigkeiten. *Annalen der Physik*, 18:79–94, 1883.

[15] W. Nußelt. Die Abhängigkeit der Wärmeübergangszahl von der Rohrlänge. *Zeitschrift des Vereins Deutscher Ingenieure*, 54:1154–1158, 1910.

[16] M. A. Lévêque. Les lois de transmission de la chaleur par convection. *Annales des Mines*, 12:201–299, 1928.

[17] V. Gnielinksi. New equations for heat and mass transfer in turbulent pipe and channel flow. *International Journal of Chemical Engineering*, 16:359–368, 1976.

[18] T. C. Thulasidas, M. A. Abraham, and R. L. Cerro. Bubble-train flow in capillaries of circular and square cross section. *Chemical Engineering Science, 50, 1995, pp. 183-199*, 50:183–199, 1995.

[19] T. C. Thulasidas, M. A. Abraham, and R. L. Cerro. Flow patterns in liquid slugs during bubble-train flow inside capillaries. *Chemical Engineering Science*, 52:2947–2962, 1997.

[20] M. Suo and P. Griffith. Two-phase flow in capillary tubes. *Journal of Basic Engineering, 86, 1964, pp. 576-582*, 86:576–582, 1964.

[21] C. A. Damianides and J. W. Westwater. Two-phase flow patterns in a compact heat exchanger and in small tubes. In *Proc. Second UK National Conf. on Heat Transfer*, pages 1257–1268. Mechanical Engineering Publications, London, 1988.

[22] T. Fukano and A. Kariyasaki. Characteristics of gas-liquid two-phase flow in a capillary tube. *Nuclear Engineering and Design*, 141:59–68, 1993.

[23] N. Brauner and D. M. Maron. Identification of the range of 'small diameters' conduits, regarding two-phase flow pattern transitions. *International Communications on Heat and Mass Transfer*, 19:29–39, 1992.

[24] Y. Taitel, D. Bornea, and D. Dukler. Two-phase flow in capillary tubes. *Journal of Basic Engineering*, 86:576–582, 1964.

[25] F. P. Bretherton. The motion of long bubbles in tubes. *Journal of Fluid Mechanics*, 10:166–188, 1961.

[26] M. D. Giavedoni and F. A. Saita. The rear meniscus of a long bubble steadily displacing a newtonian liquid in a capillary tube. *Physics of Fluids*, 11:786–794, 1999.

[27] F. Fairbrother and A. E. Stubbs. Studies in electro-endosmosis - iv. the bubble tube method for measurement. *Journal of the Chemical Society*, 1:527–529, 1935.

[28] G. I. Taylor. Deposition of a viscous fluid on the wall of a tube. *Journal of Fluid Mechanics*, 10:161–165, 1961.

[29] R. N. Marchessault and S. G. Mason. Flow of entrapped bubbles through a capillary. *Industrial and Engineering Chemistry*, 52:79–84, 1960.

[30] B. Blümich and W. Kuhn. *Magnetic Resonance Microscopy.* Wiley VCH, 1992.

[31] B. Poulson and R. Robinson. The use of a corrosion process to obtain mass transfer data. *Corrosion Science*, 26(4):265–280, 1986.

[32] P. N. Rowe, K. T. Claxton, and J. B. Lewis. Heat and mass transfer from a single sphere in an extensive flowing liquid. *Transactions of the Institution of Chemical Engineers*, 43(1):T14–T31, 1965.

[33] G. Tripathi, S. K. Singh, and S. N. Upadhyay. Dissolution of solids into turbulent liquid streams. *Indian Journal of Technology*, 9:285–291, 1971.

[34] R. P. Verma, G. N. Pandey, and G. Tripathi. Mass transfer from axi-symmetrical bodies to fluids. *Indian Journal of Technology*, 13:145–151, 1975.

[35] V. V. Rao and O. Trass. Mass transfer from a flat surface to an impinging turbulent jet. *Canadian Journal of Chemical Engineering*, 42:95–99, 1964.

[36] F. Vašak, V. Kolař, and Z. Brož. Mass transfer into the liquid in turbulent flow at high schmidt numbers. dissolution of benzoic acid into aqueous solutions of glycerol from internal surface of the pipe. *Collection of Czechoslovak Chemical Communications*, 46:1566–1576, 1981.

[37] H. Huihua Mao, Y. Christi, and M. Moo-Young. Multiphase hydrodynamics and solid-liquid mass transport in an external-loop airlift reactor - a comprehensive study. *Chemical Engineering Communications*, 113:1–13, 1992.

[38] T. Hirose, Y. Mori, and Y. Sato. Solid-liquid mass transfer in falling liquid films on single spheres. *Journal Chemical Engineering of Japan*, 7(1):19–24, 1974.

[39] V. Vacek and V. Rod. Diffusion coefficients of potassium chromate and dichromate in water at 25°c. *Collection of Czechoslovak Chemical Communications*, 51:1403–1406, 1986.

[40] F. Straight and W. D. Baasel. A comparison of theoretical and experimental results for the internal dissolution of soluble cylinders by water in laminar flow. *American Institute of Chemical Engineers Journal*, 14(5):722–726, 1968.

[41] S. Irandoust and B. Andersson. Concentration-dependent diffusivity of benzoic acid in water and its influence on the liquid-solid mass transfer. *The Canadian Journal of Chemical Engineering*, 64:954–959, 1986.

[42] K. Arata. Solid superacids. *Advances in Catalysis, 37, 1990, pp. 165-177*, 37:165–177, 1990.

[43] B. T. Ellison and W. R. Schmeal. Corrosion of steel in concentrated sulphuric acid. *Journal of the Electrochemical Society*, 125:521, 1978.

[44] D. P. Gregory and A. C. Riddiford. Transport to the surface of a rotating disc. *Journal of the Chemical Society,*, pages 3756–3764, 1956.

[45] D. P. Gregory and A. C. Riddiford. Dissolution of copper in sulphuric acid solutions. *Journal of the Electrochemical Society*, 107:950, 1960.

[46] V. K. Patil and M. M. Sharma. Solid-liquid mass transfer coefficients in bubble columns up to one meter diameter. *Chemical Engineering Research and Design*, 61:21–28, 1983.

[47] M. A. Zarraa, Y. A. El-Tawil, H. A. Farag, M. Z. El-Abd, and G. H. Sedahmed. Effect of gas sparging on the rate of mass transfer at a single sphere. *The Chemical Engineering Journal*, 47:187–191, 1991.

[48] M. Nishikawa, K. Inui, Y. Yonezawa, and S. Nagata. Mass transfer from solid particles in a spouted vessel. *International Chemical Engineering*, 16(4):714–719, 1976.

[49] S. Goeringer, N. R. de Taconi, C. R. Chenthamarakshan, and K. Rajeshwar. Reduction of hexavalent chromium by copper. *Journal of Applied Electrochemistry*, 30:891–897, 2000.

[50] D. G. Lee and R. Stewart. The nature of chromium (vi) in acid solution and its relation to alcohol oxidation. *Journal of the American Chemical Society*, 86:3051–3056, 1964.

[51] Alan Vincent. Determination of an equilibrium constant. *Education in Chemistry*, 27(4):107–108, 1990.

[52] A. M. Barajas and R. L. Panton. The effect of contact angle on two-phase flow in capillary tubes. *International Journal of Multiphase Flow*, 19:337–346, 1993.

[53] J. H. Ferziger and M. Peric. *Computational Methods for Fluid Dynamics*. Springer, 1997.

[54] H. K. Versteeg and W. Malalasekera. *An Introduction to Computational Fluid Dynamics - The Finite Volume Method*. Longman, 1995.

[55] S. V. Patankar. *Numerical Heat Transfer and Fluid Flow*. Hemisphere Publishing Corporation, Taylor and Francis Group, New York, 1980.

[56] D. B. Spalding. A novel finite-difference formulation for differetial expressions involving both first and second derivatives. *International Journal on Numerical Methods in Engineering*, 4:551–, 1972.

[57] B. P. Leonard. A stable and accurate modelling procedure based on quadratic upstream interpolation. *Computational Methods in Apllied Mechanical Engineering*, 19:59–98, 1979.

[58] G. Anger et al. Chromic acids. In *Ullmann's Encyclopedia of Chemical Engineering*. Wiley-VCH, 6th ed., electronic release edition, 1998.

[59] D. R. Lide and Ed. *CRC Handbook of Chemistry and Physics*. CRC Press, 80th ed. edition, 1999.

[60] M. Pourbaix. *Atlas d'equilibres electrochimiques*. Gauthier-Villars, Paris, 1963.

[61] N. Iadicicco, L. Paduano, and V. Vitagliano. Diffusion coefficients for the system potassium chromate - water at 25°c. *Journal of Chemical Engineering Data*, 41:529–533, 1996.

[62] B. Shome and M. K. Jensen. Mixed convection laminar flow and heat transfer of liquids in isothermal horizontal circular ducts. *International Journal of Heat and Mass Transfer*, 38:1945–1956, 1995.

[63] B. Zeldin and F. W. Schmidt. Developing flow with combined forced-free convection in an isothermal vertical tube. *Journal of Heat Transfer*, 94:211–223, 1972.

[64] J. S. Newman. *Electrochemical Systems*. Prentice Hall, 2nd ed. edition, 1991.

[65] R. Taylor and R. Krishna. *Multicomponent Mass Transfer*. Wiley, 1993.

[66] C. Horvath, A. Sardi, and B. A. Solomon. Enzyme reactor tubes. effect of diffusion and slug flow. *Physiological Chemistry and Physics*, 4(2):125–130, 1972.

# About the author

Rainer Gruber was born on February 28th, 1968 in London, Great Britain. He studied mechanical engineering at Aachen University of Technology (RWTH Aachen), specialising in biochemical engineering. He wrote his diploma thesis in the group of Prof. George Coony at the department of chemical engineering at the Massachusetts Institute of Technology, Cambridge, USA, and graduated from RWTH in 1996. He then joined the membrane science group of Prof. Thomas Melin at the Institut für Verfahrenstechnik of RWTH, where he wrote this thesis.

After completing his dissertation, Mr. Gruber joined R&D at Fresenius Hemocare GmbH, Friedberg, Germany.